NANYANG
TECHNOLOGICAL
UNIVERSITY

CATALYST DESIGN FOR ELECTROCHEMICAL CO_2 REDUCTION THROUGH DFT CALCULATIONS

SUN YUANMIAO

SCHOOL OF MATERIALS SCIENCE AND ENGINEERING

2017

CATALYST DESIGN FOR ELECTROCHEMICAL CO_2 REDUCTION THROUGH DFT CALCULATIONS

SUN YUANMIAO

SCHOOL OF MATERIALS SCIENCE AND ENGINEERING

A thesis submitted to the Nanyang Technological University
in partial fulfilment of the requirement for the degree of
Doctor of Philosophy

2017

Statement of Originality

I hereby certify that the work embodied in this thesis is the result of original research and has not been submitted for a higher degree to any other University or Institution.

4 August 2017
…………………….
Date

sun yuanmiao
……………………………..
Sun Yuanmiao

Abstract

Electrochemically converting CO_2 into low-coordinated carbides provides a sustainable way to utilize CO_2 but, unfortunately, requires effective catalysis. The catalytic activity of currently employed metallic catalysts is largely hindered by the low energy efficiency (high overpotential) and poor product selectivity (low Faradaic efficiency). In this thesis, by taking advantage of the density functional theory (DFT) calculations, three strategies – creation of low-coordinated atomic sites, surface alloying, and phase transformation – are proposed to design effective catalysts towards CO_2 electrochemical reduction (CO_2ER).

Large numbers of low-coordinated atomic sites are contained in experimentally synthesized nanoparticles (NPs), whose catalytic roles towards CO_2ER have never been theoretically investigated. Hypothesizing these low-coordinated sites are more active in catalyzing CO_2 reduction, we modelled four types of low-coordinated Cu sites – the plain (100) site, the edgy (211) site, the cornered (532) site, and the defective vac-(111) site – and compared their catalytic activity with the full-coordinated (111) site. For all the mono-carbide products, significantly lowered energetics of reaction intermediates (as high as 74.5% decrease) were found on the low-coordinated sites, estimating decreased overpotential for CO_2ER. Moreover, on the low-coordinated sites, formation of methane was found to be more thermally advantageous than the formation of methanol, implying the generation of hydrocarbons is likely proceeded on these sites. Finally, the unwanted hydrogen evolution reaction (HER) was also found to estimate lowered overpotentials (as high as 66%) on the low-coordinated sites, suggesting that high operation potentials are required to suppress this competing reaction.

Design of surface alloys (SAs) is also proposed to be effective in achieving lowered reaction overpotential for catalyzing CO_2ER. In order to screen out a decent Cu SA catalyst, we have systematically studied the stability and reaction performance of all transition-metal doped Cu SAs. By computing the segregation energy and mixing energy, only eight transition metals (Au, Ag, Zn, Cd, Sc, Y, Pd, and Pt) were found to stably alloy Cu at the topmost layer. For the catalytic activity, SA of ZnCu was found to remain almost the same reaction overpotential for CO_2ER as Cu, but considerably enlarged (200%) the one for the competing HER. Dopants of Au, Ag, Pd, and Pt resulted in enlarged overpotential for CH_4 generation; while dopants of Sc and Y showed no activity towards CO_2ER. When doping low concentration Cd into Cu surface, the generated Cu-Cd-Cu bonding cannot change the selectivity for CH_4; however, when doping high concentration Cd, the formed Cd-Cd-Cu site can selectively and effectively catalyze CO_2 into HCOOH, with the prevention of yielding hydrocarbons as well as the unwanted HER.

The effect of phase transformation on the catalytic activity of metals towards CO_2ER is also explored. Using Cu (selectivity of hydrocarbon), Au (selectivity of CO), and Pb (selectivity of HCOOH) as representatives, the catalytic performances of these metals in crystal symmetry of fcc, bcc, 2H, 4H, and sc have been investigated. It is found that only passive metals (Au) were stable in sc phase under CO_2ER conditions. For other orientations, the binding affinity towards CO_2ER intermediates followed the trend of fcc < hcp-type (2H and 4H) < bcc, suggesting a general guidance can be utilized in tuning the catalytic activity of metals. For Au and Pb, since their original symmetry is fcc, converting the fcc phase into bcc type can result in a 25.2% and 21.3%, respectively, decreased onset potential for catalyzing CO_2ER.

Acknowledgements

Four years ago, with the dream of exploring the materials' world, I came to School of Materials Science and Engineering, Nanyang Technological University to pursue my PhD degree. I have been very lucky to get the guidance, help, and support from a lot of people. Herein, I would like to take this opportunity to express my gratitude to the following people who have helped me during the period of my PhD study. I appreciate their countless advices and guidance that have created a valuable and unforgettable learning experience for me.

Firstly, I would like to express my most sincere appreciation to my PhD supervisor, Associate Professor Li Shuzhou, for his continuous guidance and advices in all aspects in processing the project and for the chance offered me to work independently and analyze logically.

I also would like to thank Assistant Professor Jason Xu Zhichuan, for his patience and valuable suggestions and comments about my work. The experimental insight brought by him is of great help to this work.

I appreciate my group members, Dr. Shi Wenxiong, Dr. Wang Xiaotian, Dr. Hao Wei, Dr. Liow Chi Hao, Dr. Zhang Zhonghan, Dr. Ankit Bisht, Dr. Li Anran, Mr. Chen Chao, Mr. Zhong Lixiang, and Mr. Wei Jiaqi, for their consistent support and encouragement along the way.

In addition, I would like to thank all MSE staffs and technicians who have provided valuable office supplies and other facilities used in the project.

Last but definitely not the least, I want to give all my thanks and respects to my family. I would have never got this far without the strong support from my family.

Table of Contents

Table Captions

Figure Captions

Figure 2.1 Schematic illustration of a common CO2 electro-reduction device in laboratory.

Figure 2.2 Two categories of catalysis process (a) homogeneous catalysis and (b) heterogeneous catalysis.

Figure 2.3 (a) Schematic of a typical metal complex. (b) Aresta catalyst for CO_2 absorption. (c) Eisenberg catalyst for CO_2 to CO.

Figure 2.4 (a) The general electro-catalytic cycle for CO_2 reduction on homogeneous catalyst. (b) CO_2 reduction cycle on $[Ni(cyclam)]^{2+}$.

Figure 2.5 Proposed mechanism for pyridinium catalyzed reduction of CO_2 to methanol on Pt electrode.

Figure 2.6 Product selectivity of CO_2ER on transition- and post transition-metals.

Figure 2.7 (a) Measured current density vs. applied potential for CO_2 on Au particles in different size. (b) Calculated free energy pathway of CO formation on different Au surfaces. Reproduced with permission from ref. 42 © 2014 American Chemical Society.

Figure 2.8 (a) SEM image of oxide derived Au particle. (b) PXRD of oxide derived Au particle. (c) Faradaic efficiency on polycrystalline Au and oxide derived Au. Reproduced with permission from ref. 47 © 2012 American Chemical Society.

Figure 2.9 (a) Schematic illustration of concave rhombic dodecahedral Au particle. (b) Surface roughness of the concave rhombic dodecahedral Au. (c) CO Faradaic efficiencies on Au catalysts in different morphology. Reproduced with permission from ref. 51 © 2015 American Chemical Society.

Figure 2.10 (a) Production ratio between CH_4 and C_2H_2 vs. applied potential on different Cu/Pt systems. (b) Schematic illustration for the surface reconstruction of monolayer Cu on Pt substrate. Reproduced with permission from ref. 57 and 58 © 2013 American Chemical Society.

Figure 2.11 (a) Side view of two metal-metal overlayer systems. The left one is a system with one-layer guest metal coated on the substrate one. The right one is a near-surface alloy (NSA) with the second layer to be guest metals. (b) Plotted volcano plot on the designed systems. The figure plots the predicted limiting potential ($U_{L,volcano}$) as a function of the binding energy of CO and OH. In this figure, each line represents one elementary step involved in CO_2ER. The CH_3OH production is preferred at weaker (less negative) OH binding energies. In total, 27 stable NSAs and pure metals are calculated in the study. Those NSAs that are located close to the top of CO-analogous volcano (i.e., between Cu and Au) are marked in blue. Reproduced with permission from ref. 59 © 2015 American Chemical Society.

Figure 2.12 (a) Faradaic efficiency of CO_2ER on 0D copper. The bars in black, red, and blue represent CO, HCOOH, and H_2, respectively. The data is analyzed at –0.6 V vs. RHE in 0.1 M $KHCO_3/CO_2$. (b) Faradaic efficiency of CO_2ER on In doped Cu. The bars in black and blue represent CO and H_2, respectively. (c) Computed Free energy pathway on Cu(100) and In doped Cu(100). The reaction is CO_2ER to CO via a *COOH intermediate. The red line represents free energy pathway of clean Cu (100), while the blue line stands for the path on In doped Cu (100). The configurations of the corresponding states are also illustrated in the upper level. Reproduced with permission from ref. 67 © 2014 Wiley-VCH Verlag GmbH & Co.

Figure 2.13 (a) Current density vs. applied potential on WSe_2 nanoflakes and other catalysts. (b) Computed free energy pathway on metal dichalcogenides and Ag surfaces. Reproduced with permission from ref. 78 © 2016 American Association for the Advancement of Science.

Figure 2.14 (a) Schematic of different kinds of doped N in the carbon lattice. (b) Computed free energy pathway on these doped N sites. Reproduced with permission from ref. 59 © 2016 American Chemical Society.

Figure 3.1 Smart design for new catalyst with combination of both theoretical and experimental approaches.

Figure 3.2 Reaction coordinates of non-catalyst approach and catalyst-boosted approach.

Figure 3.3 A schematic representation of the Sabatier principle.

Figure 3.4 (a) Schematic illustration of the density of states of a transition metal, containing the broad s band the narrow d bands around the Fermi level, ε_F. (b). Bonding states between the adsorbate σ orbital and the metal *d*-band.

Figure 3.5 The projected density of states of atomic hydrogen chemisorbed on the (111) surface of Ni, Cu, Pt, and Au. The dashed lines show the PDOS of the four clean metal surfaces while the solid lines illustrate the PDOS after the chemisorption. Reproduced with permission from ref. 8 © 2009 Nature Publishing Group.

Figure 3.6 (a) Illustration of the scaling relations for adsorption energies of CH_x intermediates (crosses: x = 1; circles: x = 2; triangles: x = 3). The adsorption substrates are the most close-packed surfaces of the corresponding metals. (b). Illustration of the scaling relations for adsorption energies of *OH *vs.* *O (red), *OOH *vs.* *O (orange), and *OCH_3 *vs.* *O (blue). The types of adsorption sites are labeled at the top. The triangles represent hexagonal-symmetry sites, and the squares represent sites with square or mixed hexagonal/square symmetry. Reproduced with permission from ref. 9 © 2007 American Physical Society.

Figure 3.7 A schematic illustration of the Brønsted–Evans–Polanyi (BEP) principle on the positive correlation between activation energy and reaction energy. Is, ts, and fs represent initial state, transition state, and final state, respectively.

Figure 3.8 A schematic illustration of an interacting system described by many-body perspective and density functional theory (DFT) perspective.

Figure 3.9 A schematic illustration of the connection between experimental situation and simulation model.

Figure 3.10 Two possible reaction pathways for electro-chemical hydrogen evolution reaction (HER).

Figure 3.11 The generated volcano plot (the experimentally measured exchange current density, j_0, as a function of the theoretical H chemisorption free energy, ΔG_{H*}) for HER. Original data are taken from ref. 28 © 2005 The Electrochemical Society, Inc.

Figure 3.12 (a) The most economic reaction pathway for mono-carbides formation during CO_2 reduction processes. For each arrow, it represents an elementary step of proton and electron transfer. The steps for the generation of products have been highlighted by red cubes. (b) Side view of each elementary step on stepped Cu(211). The atoms in red, brown, white, and blue represent O, C, H, and Cu, respectively.

Figure 4.1 Hypothesis of the intrinsic reason for the catalytic performance on the currently employed structural modification approaches.

Figure 4.2 Illustration of the possible atomic sites on a metal nanoparticle.

Figure 4.3 Top view of the two planar surfaces: (a) the full-coordinated (111) surface; (b) the low-coordinated (100) surface.

Figure 4.4 Top view of nonplanar surfaces: (a) vac-(111) surface; (b) (211) surface; (c)

Figure 5.5 Illustration of the (211) orientation of Cu: (a) side view; (b) top view. The lines of edge atoms are highlighted in dark blue.

Figure 5.6 The two types of SA models used in this work: (a) low concentration doping, with a Cu-M-Cu edge; (b) high concentration doping, with a M-M-Cu edge.

Figure 5.7 Results of the computed segregation energy (E_{seg}) and mixing energy (E_{mix}) on the Cu SAs. The red cubes highlight those who can stably alloy Cu at the topmost layer, with a negative value for both the mixing energy (E_{mix}) and segregation energy (E_{seg}).

Figure 5.8 (a) The reaction pathway from CO_2 to CH_4 involving the carbon based intermediates. (b) E_B[COOH] (c) E_B[CHO] (d) E_B[CH_2O] as a linear function of E_B[CO].

Figure 5.9 (a) The reaction pathway from CO_2 to CH_4 involving the oxygen based intermediates. (b) E_B[OCH_3] (c) E_B[O] as a linear function of E_B[OH].

Figure 5.10 Side view of the most stable binding configurations of (a) *COOH and *CHO and (b) *OCH_3 and *OH on Cu (211).

Figure 5.11 Limiting potentials (U_L) for elementary proton-transfer steps for CO_2 reduction to CH_4. Each line is the calculated potential at which the indicated elementary reaction step is neutral with respect to free energy, as a function of E_B[CO] or E_B[OH] on the surface of catalysts. The equilibrium potential for the overall electrochemical reduction of CO_2 to CH_4 is +0.17 V (*vs.* RHE), which is also indicated in the figure. Hence, the theoretical overpotential as a function of E_B[CO] or E_B[OH] can be represented by the distance between the equilibrium line and the most-negative limiting potential line (highlighted in gray). The elementary step of *CH_2O → *OCH_3 is excluded in this figure since it is independent to neither E_B[CO] nor E_B[OH].

Abbreviations

CO_2ER	CO_2 electrochemical reduction
DFT	Density functional theory
FE	Faradaic efficiency
NPs	Nanoparticles
HER	Hydrogen evolution reaction
SAs	Surface alloys
BEP	Brønsted–Evans–Polanyi
LDA	Local-spin density approximation
GGA	Generalized gradient approximation
RDS	Rate-determining step
CHE	Computational hydrogen electrode
VASP	Vienna Ab-initio Simulation Package
PAW	Projected augmented wave
RPBE	Revised Perdew-Burke-Ernzerhof
PBE	Perdew-Burke-Ernzerhof
DOS	Density of states
fcc	Face centered cubic
bcc	Body centered cubic
sc	Simple cubic
hcp	Hexagonal close packed
ORR	Oxygen reduction reaction
OER	Oxygen evolution reaction
RHE	Reversible hydrogen electrode
NHE	Normal hydrogen electrode
SCE	Saturated calomel electrode
PPy	Polypyrrole
PAn	Polyaniline
PXRD	Power X-Ray Diffraction
TEM	Transmission electron microscope

SEM	Scanning electron microscope
2D	2-dimensional
3D	3-dimensional
EC-TEM	Electrochemical scanning tunneling microscope
CNFs	Carbon nanofibers
NG	Nitrogen doped graphene

Chapter 1

Introduction

Nowadays, the atmospheric concentration of CO_2 *has been continuously increasing due to its growing emission caused by human activities. As a consequence, severe climatic changes may be induced because of the greenhouse nature of* CO_2*. Hence, strategies of reducing and utilizing* CO_2 *are keenly desired to be explored. Electro-chemically converting* CO_2 *into low-coordinated carbides offers an economic and environmentally friendly approach to make use of* CO_2*. However, since* CO_2 *is a badly stable molecule, effective catalysis is required in order to convert it into useful carbon compounds (CO, HCOOH,* CH_4*, etc.). Computational predictions can offer great help in designing excellent catalysts towards* CO_2 *electro-chemical reduction (*CO_2*ER). This chapter presents the background information of* CO_2*ER, the proposed hypothesis, and the detailed objectives and scopes. Also, it gives a brief introduction to each chapter in this thesis and points out the major findings obtained in the results chapters.*

1.1 Background

With the development of human society, the global anthropogenic contribution of CO_2 to the atmosphere has significantly increased ever since the industrial revolution.[1] In the last decade, global CO_2 emissions have had continuous strong growth of 2.5% per year.[2,3] As CO_2 is an effective green-house gas, severe climatic consequences will result if atmospheric CO_2 level continues to rise.[4-6] Therefore, strategies need to be explored in order to reduce and utilize CO_2.

Electrochemically reducing CO_2 into low-coordinated carbides provides a sustainable means to utilize CO_2 in order to address the global climate challenges.[7] The approach of electrochemical conversion of CO_2 into various low-coordinated carbides (CO, HCOOH, CH_4, etc.) has particular advantages.[8] Firstly, the reaction can be operated under ambient pressure and temperature, which requires low-cost investment for future industrial applications. Secondly, the driving force of the reaction is electrical energy, which can be generated from renewable resources, that is the whole process is environmentally friendly. Last but not least, the numerous conversion products are important industrial feedstocks such as carbon monoxide, carboxylic, methane, methanol, ethylene, and even long hydrocarbon chains. Therefore, if CO_2 can be effectively reduced by electrochemical process, it will not only help address the climate challenge, but also be possible to enable the storage of renewable energy sources to chemical fuels with high energy density.

However, despite these advantages, as CO_2 is an awfully stable molecule, effective catalysis is essentially required in the process of CO_2 electrochemical reduction (CO_2ER). Currently, one of the most extensively employed catalyst category is metal nanoparticles (NPs).[9,10] To make the CO_2ER a cost-effective process, several criteria should be ideally met by an electrochemical catalyst.[11] First of all, to ensure the energy is efficiently converted, the catalyst should show high selectivity towards the desired products. Secondly, the catalyst should display high activity for the formation of the desired products, which, in electrochemical catalysis processes, is a low overpotential for the reduction reaction. Finally, the catalyst should stably exist under the reducing conditions.

Nevertheless, so far, to the best of our knowledge, few reported catalysts perfectly meets all these criteria.[11] The two main obstacles for practical applications of CO_2ER at present are the high reaction overpotentials (low energy efficiency) and poor product selectivity. The former is attributed to the high activation energy needed to make the reaction happen. The latter is because of the competing hydrogen evolution reaction (HER), which takes place at the same cathode surface and competes for the transferred electrons.

Experimentally, the ability of a given material to catalyze the electro-chemical reaction is normally measured by reaction overpotential, which is the potential difference between the thermal dynamical equilibrium potential and the potential at which the reaction is experimentally observed. As different materials display totally different reaction overpotential, directions are needed to make useful predictions of a given material's catalytic property in guiding experimental synthesis.

Nowadays, the big development of modern computational methods and their wide applications in scientific research have made it possible to offer sufficiently accurate estimations of key parameters necessary for the rational design of electrocatalysts, in particular the energy of interaction of reaction intermediates with catalyst surfaces. Density functional theory (DFT), which is one of the most popular and versatile methods used in computational calculation, is a good method in area of physics and chemistry to describe electronic structure of many-body systems. With this theory, the properties of a multi-electron system can be determined by using functionals, which in this case is the spatially dependent electron density. The good agreement between the DFT calculation results and the experimental data has made DFT a very useful tool for computational chemistry. During the past 30 years, DFT has been the dominant method for the quantum mechanical simulation of periodic systems, which can also be applied in the discipline of CO_2ER. Taking advantage of DFT calculations, the free energy diagrams of each reaction intermediates can be obtained to represent the evolution of CO_2 reduction on different catalysts. By comparing the most uphill free energy change, the better electro-catalyst with lower estimated reaction potential can be predicted.

1.2 Hypotheses

In order to rationally design and predict electro-catalysts for CO_2ER, computational tools are employed in this study to calculate the reaction pathway and evaluate the catalytic performance. During the entire study, three different types of approaches are hypothesized to improve the catalytic activity of metal NPs towards CO_2ER:

(1) According to the current research status of structural modifications, synthesis of small-sized particles, porous morphologies, and structures with metastable surfaces are useful strategies in designing excellent metal cathodes for CO_2ER.[12-14] However, the mechanistic understanding of the catalytic behaviors of these structures are still elusive. In the experimental process of synthesizing these types of metal nanostructures, large numbers of surface vacancies, edge atoms and corner atoms are created.[12,13] Since the low-coordinated nature of these atoms can result in raised d-band center relative to the Fermi level, the binding affinities of CO_2ER intermediates may alter greatly on these atomic sites.[15] Thus, we hypothesize the various low-coordinated atomic sites are responsible for the enhanced catalytic performances. To verify this hypothesis, different types of low-coordinated Cu sites have been simulated and the reaction pathways of CO_2ER were computed in Chapter 4.

(2) Surface alloying (doping) is an effective strategy in designing new metallic catalyst with enhanced catalytic ability. The local bimetallic areas provide different electronic structure from the monometallic ones, which may result in balanced adsorption behaviors for the key reaction intermediates and hence enhanced catalytic activity.[16,17] Approaches of surface alloying have successfully been applied in many electro-chemical catalytic reactions (HER, ORR, OER).[18-20] Since the catalytic activity of metal electrodes towards CO_2ER is largely due to the inappropriate binding affinities for the carbon or oxygen based adsorbates, we hypothesize that surface alloying approach can also work efficiently in designing excellent catalysts with lowered reaction potential. However, in CO_2ER domain, thus far, few works have focused on this type of approach and theoretical guidance is needed to navigate the experimental directions. In Chapter 5, a systematic

screening work on transition-metal doped Cu electrodes towards CO_2ER has been performed. By calculating the reaction pathways, several Cu surface alloy systems have been predicted as good CO_2ER catalyst due to their lowered energetics of CO_2ER and higher ones for HER.

(3) Recently, it has been discovered that when the size of metal structures shrinks to nanometer scale, the crystal structures of the noble metal nanomaterials may change and become distinct from their bulk counterpart.[21,22] Some properties of noble metals, for instances, the chemical stability[23], magnetic properties[24,25], and optical properties[26,27], have been reported to be phase-dependent. Since the electronic structures, which is a critical factor in determining the CO_2ER catalytic ability, of noble metals are quite sensitive to the crystal orientation, we hypothesize that altering the crystal phase of noble metals can be an alternative in changing their catalytic activities and designing efficient catalysts. In Chapter 6, studies of the catalytic capabilities of Cu, Au, and Pb in various phases （fcc, bcc, 2H, 4H, and sc） have been performed. It is believed the selected metals with their best-catalytic-phase will be of great help in guiding the experimental synthesis of new excellent catalysts.

1.3 Objectives and Scope

The overall objective of this thesis is to rationally design effective metallic electro-catalysts for advanced CO_2ER by using theoretical and computational tools. Candidates with low overpotential for CO_2ER and high overpotential for the competing HER are predicted as good catalysts. In this study, hypotheses are extensively applied on Cu electrode, since Cu is the only metal capable to catalyze CO_2 into hydrocarbons, which are of great importance for industrial uses.[9] For the purpose of a thorough investigation, metals with other product selectivity (HCOOH, CO, and H_2) in catalyzing CO_2ER are also analyzed. The detailed scopes of this study are presented as below.

(1) The perfect plain surface of Cu NP and four types of low-index Cu surfaces have been simulated to represent the full- and low-coordinated Cu surface atomic sites. The

catalytic activities of these surfaces were computed and compared to verify the hypothesis that the creation of large numbers of low-coordinated sites is responsible for the catalytic improvement in the commonly used structural modification approaches.

(2) A high-throughput of CO_2ER activity on various transition-metal doped Cu surfaces has been performed to screen out a proper Cu surface alloy (SA) as good catalyst for CO_2ER. The stability of different Cu SAs was firstly computed to find out those transition-metals who can stably alloy Cu at the topmost layer. The catalytic performances towards CO_2ER and HER were then calculated for these stable Cu SAs to identify those with good catalytic activity.

(3) The catalytic ability towards CO_2ER has been performed on Cu, Au, and Pb in various phases. Specifically, crystal phases of fcc, bcc, 2H (hcp), 4H, and sc were tested and the catalytic performances in these phases were compared.

1.4 Dissertation Overview

This thesis consists of the following 7 chapters:

Chapter 1 briefly provides the research background of the study, followed by an introduction of the research motivation, hypothesis, research objectives and scopes, the dissertation overview, and the findings and significances.

Chapter 2 comprehensively reviews the state-of-the-art approaches, both experimental and theoretical, used in designing effective catalysts towards CO_2ER. It also briefly introduces the fundamentals of CO_2ER under aqueous solutions conditions.

Chapter 3 systematically elucidates the theories behind the theoretical surface catalysis. The methods used to compute and predict the catalytic behaviors of theoretically designed catalysts have been elaborated. The reaction mechanisms and theoretical descriptors of CO_2ER and the competing HER have also been detailedly addressed.

Chapter 4 investigates the catalytic role of low-coordinated surface sites on Cu nanoparticles. Five different surfaces have been established in order to simulate the facet, edge, corner, and vacant sites on Cu NPs. Reaction behaviors of CO_2ER and HER on these simulated sites have been performed and the intrinsic reason responsible for the catalytic enhancement of the commonly employed structural-modification approach is revealed.

Chapter 5 screens the catalytic behaviors of various transition-metal doped Cu SAs. The stabilities of all the Cu SAs have been computationally assessed. Reaction performances of CO_2ER and HER on those stably existed Cu SAs were computed and the good candidates were summarized.

Chapter 6 analyzes the catalytic influence of phase-transformation on metal electrodes (Cu, Au, and Pb) towards CO_2ER. Crystal phases of fcc, bcc, 2H, 4H, and sc have been employed and the best candidate in improving the catalytic activity was summarized.

Chapter 7 concludes the results according to the hypothesis, and gives recommendations towards more advanced design of effective electro-catalysts for CO_2ER.

1.5 Findings and Outcomes/Originality

This research leads to several novel outcomes which are summarized below:

(1) The research on different Cu surfaces indicates that the estimated overpotentials of CO_2ER on various types of low-coordinated atomic sites are much lower than these on the full-coordinated sites. This result suggests reaction of CO_2ER can be boosted by the edges, corners, and the surface vacancies on the metal NPs. However, despite the acceleration of CO_2ER, the overpotentials of HER are also slightly lowered by the presence of low-coordinates sites. Considering that protons can compete the transferred electrons against CO_2 at low potential range, to take full advantage of the low-coordinated sites for catalyzing CO_2ER, high operation potentials are required, where both these two types of reactions are kinetically opened. This research gives a theoretical

explanation for the commonly employed methods of structural modifications in designing CO_2ER catalysts. We demonstrate that the creation of large numbers of low-coordinated sites on metal nanostructures can effectively enhance their ability in catalyzing CO_2ER, which is of great help in inspiring the experimental synthesis.

(2) By screening the catalytic activity of transition-metal doped Cu SAs, we demonstrate that alloying high concentration Cd into Cu surface can potentially be an effective strategy in catalyzing CO_2 into HCOOH. The formed Cd-Cd-Cu environment can dramatically decrease the overpotential for HCOOH generation and increase the overpotential for the unwanted HER. Moreover, since *CO cannot be captured by this surface, it prevents the yield of hydrocarbon products, leading to high selectivity of HCOOH. This prediction can help to synthesize more effective Cu based NPs for high catalytic performance of CO_2ER. Additionally, through the stability test of Cu SAs, only 8 kinds of transition metals (Au, Ag, Zn, Cd, Y, Sc, Pt, and Pd) can stably alloy Cu at the topmost surface. This finding is quite useful in predicting the stability of experimentally synthesized doping systems.

(3) Finally, by performing the CO_2ER reaction on the noble metals (Au, Cu, and Pb) in various crystal phases (fcc, bcc, sc, 2H, and 4H), we have demonstrated, for the first time, that phase-transformation is an effective strategy in designing metallic electrode of high catalytic performance towards CO_2ER. More importantly, we find that the binding affinities follow the trend of fcc < hcp-type < bcc. Considering that technologies of phase engineering are rapidly developing in recent years, we believe this pioneer work will, to a great extent, be of great significance in helping to construct new category towards effective electro-catalysts.

References

1 Finn, C. *et al.* Molecular approaches to the electrochemical reduction of carbon dioxide. *Chemical Communications* **48**, 1392-1399 (2012).

2 Friedlingstein, P. *et al.* Persistent growth of CO_2 emissions and implications for reaching climate targets. *Nature Geosci* **7**, 709-715 (2014).

3 Meinshausen, M. *et al.* Greenhouse-gas emission targets for limiting global warming to 2 C. *Nature* **458**, 1158-1162 (2009).

4 Tokarska, K. B. *et al.* The climate response to five trillion tonnes of carbon. *Nature Climate Change* **6**, 851-855 (2016).

5 Allen, M. R. *et al.* Warming caused by cumulative carbon emissions towards the trillionth tonne. *Nature* **458**, 1163-1166 (2009).

6 Raupach, M. R. *et al.* The relationship between peak warming and cumulative CO_2 emissions, and its use to quantify vulnerabilities in the carbon–climate–human system. *Tellus B* **63**, 145-164 (2011).

7 Lim, R. J. *et al.* A review on the electrochemical reduction of CO_2 in fuel cells, metal electrodes and molecular catalysts. *Catalysis Today* **233**, 169-180 (2014).

8 Qiao, J. *et al.* A review of catalysts for the electroreduction of carbon dioxide to produce low-carbon fuels. *Chemical Society Reviews* **43**, 631-675 (2014).

9 Hori, Y. *et al.* Electrocatalytic process of CO selectivity in electrochemical reduction of CO_2 at metal electrodes in aqueous media. *Electrochimica Acta* **39**, 1833-1839 (1994).

10 Peterson, A. A. *et al.* Activity Descriptors for CO_2 Electroreduction to Methane on Transition-Metal Catalysts. *The Journal of Physical Chemistry Letters* **3**, 251-258 (2012).

11 Kondratenko, E. V. *et al.* Status and perspectives of CO_2 conversion into fuels and chemicals by catalytic, photocatalytic and electrocatalytic processes. *Energy & Environmental Science* **6**, 3112-3135 (2013).

12 Mistry, H. *et al.* Exceptional size-dependent activity enhancement in the electroreduction of CO_2 over Au nanoparticles. *Journal of the American Chemical Society* **136**, 16473-16476 (2014).

13 Lu, Q. *et al.* A selective and efficient electrocatalyst for carbon dioxide reduction. *Nature Communications* **5**, 3242 (2014).

14 Chen, Y. *et al.* Aqueous CO_2 reduction at very low overpotential on oxide-derived Au nanoparticles. *Journal of the American Chemical Society* **134**, 19969-19972 (2012).

15 Durand, W. J. *et al.* Structure effects on the energetics of the electrochemical reduction of CO_2 by copper surfaces. *Surface Science* **605**, 1354-1359 (2011).

16 Stamenkovic, V. R. *et al.* Trends in electrocatalysis on extended and nanoscale Pt-bimetallic alloy surfaces. *Nature Materials* **6**, 241-247 (2007).

17 Nørskov, J. K. *et al.* Towards the computational design of solid catalysts. *Nature Chemistry* **1**, 37-46 (2009).

18 Greeley, J. *et al.* Computational high-throughput screening of electrocatalytic materials for hydrogen evolution. *Nature Materials* **5**, 909-913 (2006).

19 Greeley, J. *et al.* Alloys of platinum and early transition metals as oxygen reduction electrocatalysts. *Nature Chemistry* **1**, 552-556 (2009).

20 Forgie, R. *et al.* Bimetallic Ru electrocatalysts for the OER and electrolytic water splitting in acidic media. *Electrochemical and Solid-State Letters* **13**, B36-B39 (2010).

21 Fan, Z. *et al.* Crystal phase-controlled synthesis, properties and applications of noble metal nanomaterials. *Chemical Society Reviews* **45**, 63-82 (2016).

22 Kusada, K. *et al.* A route for phase control in metal nanoparticles: a potential strategy to create advanced materials. *Advanced Materials* **28**, 1129-1142 (2016).

23 Kim, J. *et al.* Structurally ordered FePt nanoparticles and their enhanced catalysis for oxygen reduction reaction. *Journal of the American Chemical Society* **132**, 4996-4997 (2010).

24 Li, Q. *et al.* New approach to fully ordered fct-FePt nanoparticles for much enhanced electrocatalysis in acid. *Nano Letters* **15**, 2468-2473 (2015).

25 Kim, J. *et al.* Dispersible ferromagnetic FePt nanoparticles. *Advanced Materials* **21**, 906-909 (2009).

26 Fan, Z. *et al.* Stabilization of 4H hexagonal phase in gold nanoribbons. *Nature Communications* **6** 7684 (2015).

27 Chakraborty, I. *et al.* A stable, quasi-2D modification of silver: optical, electronic, vibrational and mechanical properties, and first principles calculations. *Journal of Physics: Condensed Matter* **26**, 025402 (2013).

Chapter 2

Literature Review

This chapter starts with a brief description of the electrochemical CO_2 *conversion process and introduces the fundamentals of* CO_2 *reduction reactions. Two commonly used catalysis approaches, homogeneous and heterogeneous, are presented. The demand for an outstanding catalyst, which can catalyze the reaction both effectively, with low required overpotential to activate the reaction, and selectively, with high Faradaic efficiency towards one targeted product, is elucidated. Status of the currently researched techniques, both experimentally and theoretically, towards designing a remarkable electro-catalyst is extensively reviewed. Homogeneous catalysts are classified into metal complexes, conducting polymer based catalysts, and pyridinium. Their characteristics in* CO_2 *conversion are summarized. For heterogeneous ones, as the catalytic performances of conventional transition and post-transition metals are quite limited, structural and compositional modifications are intensively applied. Moreover, recently, metal compounds (oxide and dichalcogenide) have also been reported to behave prominently for* CO_2*ER. Finally, the newly investigated carbon-based materials, which can selectively reduce* CO_2 *into CO, are also reviewed.*

2.1 Electrochemical CO_2 Reduction

Electrochemical CO_2 reduction, by definition, is converting gaseous CO_2 into useful chemicals by means of electric power. Although suffered from high energy consumption and low energy efficiency, the electrochemical method has following advantages: (1) the whole process is controllable by electrode potentials and reaction temperature; (2) the overall chemical consumption can be minimized to only water once methods have been proposed to recycle the supporting electrolyte (see Figure 2.1); (3) electricity can be renewably generated (wind, solar, hydro, geothermal, tidal, and others); and (4) devices for the electrochemical reaction can be designed compact, modular, and easy for scale-up application.[1]

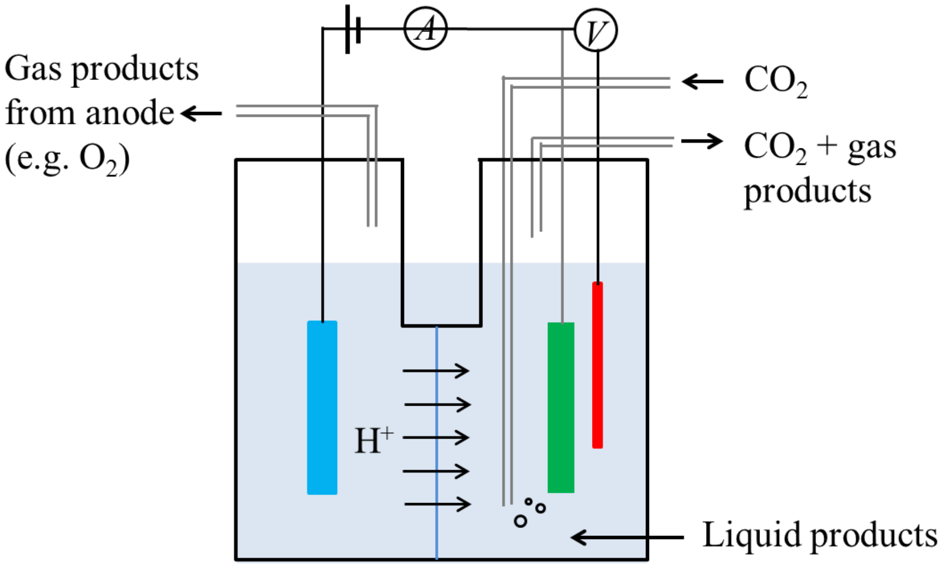

Figure 2.1 Schematic illustration of a common CO_2 electro-reduction device in laboratory.

A typical electrochemical CO_2 reduction device for laboratory use is illustrated in Figure 2.1. Oxidation reaction and reduction reaction take place at the anode and cathode surfaces, respectively. Hence, CO_2 is injected at the cathodic side. After the reaction, the unreacted CO_2 and gas products will be released from the same side, while the liquid products, if any, will stay in the solution.

Electrochemical reduction of CO_2 can precede through two-, four-, six-, and eight-electron transfer processes. Various products can be produced via different reaction pathways; the major products are formaldehyde (HCHO), carbon monoxide (CO), formic acid (HCOOH) or formate ($HCOO^-$) in basic solution, methane (CH_4), methanol (CH_3OH), and many others. The thermodynamic electrochemical reactions of CO_2 reduction and their corresponding standard electrode potentials in aqueous systems are summarized in Table 2.1.[2] The one-electron reduction of CO_2 to $CO_2^{\bullet -}$ has an E^0 of -1.90 V *vs.* NHE (standard hydrogen electrode) at pH = 7. Thus, compared with the mono-electron transfer process, multiple proton-coupled electron transfers are thermodynamically favored. However, since CO_2 is a terribly stable molecule, even with the help of catalysts, large energy input is still needed to activate the reduction reaction, resulting in extremely high overpotential (~1 V). A second major difficulty is the product selectivity. As shown in Table 1, reduction of CO_2 may lead to CO, HCOOH, HCHO, CH_3OH, CH_4, and even higher hydrocarbons. Besides, as the reaction takes place in aqueous solutions, another cathodic reaction, hydrogen evolution reaction (HER), will complete the electrons transferred on the cathode and reduce the faradaic efficiency for CO_2 reduction products.[3] It should be mentioned that the reactions presented in Table 2.1 are thermodynamic, showing only the tendency and possibility of each reaction, while the reaction mechanism or kinetics are not indicated.

Table 2.1 Selected standard potentials of CO_2 reduction reactions at 1.0 atm and 25 °C.

Electrochemical thermodynamic half-reactions	Electrode potential (V *vs.* NHE) under standard conditions
$CO_2(g) + e^- \rightarrow CO_2\bullet^-$	-1.90
$CO_2(g) + 2H^+ + 2e^- \rightarrow CO + H_2O$	-0.53
$CO_2(g) + 2H^+ + 2e^- \rightarrow HCOOH$	-0.61
$CO_2(g) + 4H^+ + 4e^- \rightarrow HCHO + H_2O$	-0.48
$CO_2(g) + 6H^+ + 6e^- \rightarrow CH_3OH + H_2O$	-0.38
$CO_2(g) + 8H^+ + 8e^- \rightarrow CH_4 + H_2O$	-0.24
$2H^+ + 2e^- \rightarrow H_2$	-0.42

Requirements for an excellent catalyst are low activation overpotential for the reaction, high product selectivity, and long-term stability. Unfortunately, so far, no such material is well-accepted to catalyze the electro-reduction of CO_2 to low-coordinated carbides both efficiently and selectively. Hence, in recent years, methods have been intensively reported to design an electro-catalyst with applicable catalytic performance toward CO_2 reduction.

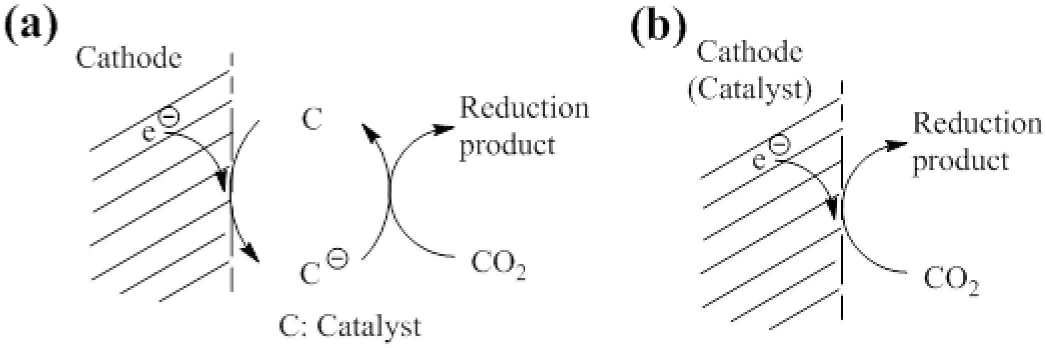

Figure 2.2 Two categories of catalysis process (a) homogeneous catalysis and (b) heterogeneous catalysis.

Generally, catalysis processes are classified into two groups, homogeneous and heterogeneous.[4] Accordingly, the catalysts used in CO_2 electro-reduction can also be divided into these two categories. As illustrated in Figure 2.2, homogeneous catalysis are catalytic reactions where the catalyst is in the same phase as the reactants, while heterogeneous catalysis refers to those where the catalyst and the reactants are in different phases. Specifically, in electro-chemical CO_2 reduction discipline, homogeneous and heterogeneous catalysts relate to those in liquid and solid phases, respectively. At the present stage, great achievements have been made by both these two kinds of catalysts; however, challenges still remain to design appropriate ones active enough for industrial applications. Reviews on the status of these two types of catalysts for CO_2 electro-reduction will be presented in the following sections.

2.2 Homogeneous Catalysts

Metal complex is the most typical homogeneous electro-catalyst for CO_2 reduction. The origins of transition metal complex that exhibit catalytic activity for CO_2 reduction can trace back to 1970s.[5] Through decades' efforts, this catalyst species has gained in breadth and intensity, however, some intrinsic limitations still hinder the catalytic effect of metal complexes. Hence, researchers still show great interests in designing suitable metal complex for remarkable CO_2 conversion performance. Besides this catalyst category, in recent years, several homogeneous catalysts that are non-metallic complexes have been proposed, which can be divided into two types: conducting polymers, and pyridinium derivatives.

2.2.1 Metal Complexes

A typical metal complex catalyst consists of a central metal, which is called the coordination center, and a surrounding array of bound molecules, that are in turn known as ligands (see Figure 2.3). The center metals, which, in most cases, are transition metals, can react with substrate as they exhibit unfilled or half-filled orbitals. Usually, CO_2 molecule can be absorbed by metal complex through binding with the center metal, activating the conversion process. Synergistically, the small organic ligands serve as electron donors and sometimes, assist the solubility of the complex.[6]

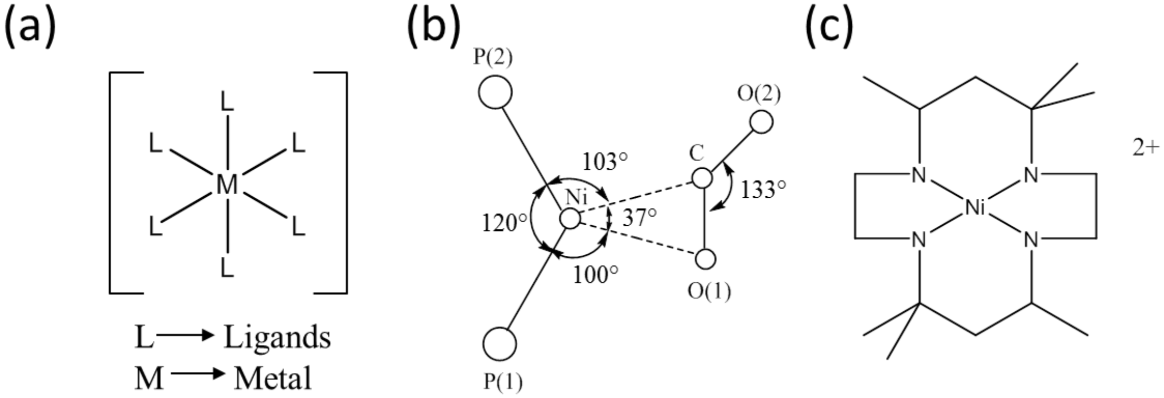

Figure 2.3 (a) Schematic of a typical metal complex. (b) Aresta catalyst for CO_2 absorption. (c) Eisenberg catalyst for CO_2 to CO.

The first transition metal complex that was able to stably react with CO_2 without any reverse reactions was reported by Aresta and Nobile in 1975.[7] In this breakthrough finding, a nickel complex $[NiX_2L_2]$ (X = Cl, Br; L = PCy_3, $PBu^n{}_3$, PEt_2Ph, PEt_3; Cy = cyclohexyl) was designed and CO_2 was found to bind to Ni through the carbon atom and one oxygen atom, with a significant bending structure (Figure 2.3). At this point, although CO_2 is just absorbed into the metal complex and no low-coordinated carbide was released, it did suggest that homogeneous metal complexes showed growth potentials to catalyze CO_2 under electro-catalysis treatment.

Another landmark was reported by Fisher and Eisenberg in 1980 using tetraazomacrocyclic complexes of cobalt and nickel (Figure 2.3).[8] For the first time, this paper quantitatively analyzed the reduction products in the reaction. Particularly, the two major products are gaseous: CO and H_2. Although mechanistic insight into the reaction was not proposed and very high potentials (-1.3 to -1.6 V *vs.* SCE) were required, the high current efficiencies (up to 98%) suggested homogeneous transition metal complexes could serve decently as electro-catalysts for CO_2 conversion to low-coordinated carbides. Ever since that, category of homogeneous CO_2 reduction catalysts has been systematically studied and based on different ligand type, three categories of metal complexes have been built up: metal complexes with (1) macrocyclic ligands, (2) bipyridine ligands, and (3) phosphine ligands.[9] At the present stage, metal complexes with center metals of cobalt[10,11], nickel[12,13], rhenium[14-16], ruthenium[17-19], manganese[20,21], and even medal metals[22,23] have been reported to be capable to convert CO_2 into other carbides. The reduction products can range from carbon monoxide[19,20,24], formic acid[13,25], formaldehyde[26], to hydrocarbon such as oxalate[23]. Compared with conventional metallic catalysts, although the required potentials are quite large[27] (starts from -1.25 V *vs.* SCE and can be as high as -2.2 V *vs.* SCE) and still need tremendous efforts to improve, the faradaic efficiency of CO_2 reduction products catalyzed by homogeneous catalysts is significantly high (more than 60%) and, in some cases, even reaches 100%[21].

Through years' efforts, the mechanisms behind homogeneous catalysis of CO_2 electro-reduction have been revealed and the simplified paradigm[4] is shown in Figure 2.4. For effective catalysis, the catalyst precursor in Figure 2.4 must take up electrons at a relatively low potential to give a reaction intermediate that can bind one or more equivalents of substrate. It should be mentioned that for CO_2 reduction, in most cases the substrate is CO_2 itself, however, it could also be species that is activated toward attack at CO_2. In both cases, a substrate complex is formed. The substrate complex can now continue to react with excess electrons and/or substrate, to products or regenerate either the reaction intermediate or the catalyst precursor. An important consideration is the reaction pathways that lead to catalyst deactivation. Under normal circumstances, these will occur at the stage of reaction intermediate or substrate complex. However, occasionally, they can be as simple as physical precipitation of a complex that appears in competition with the catalysis.

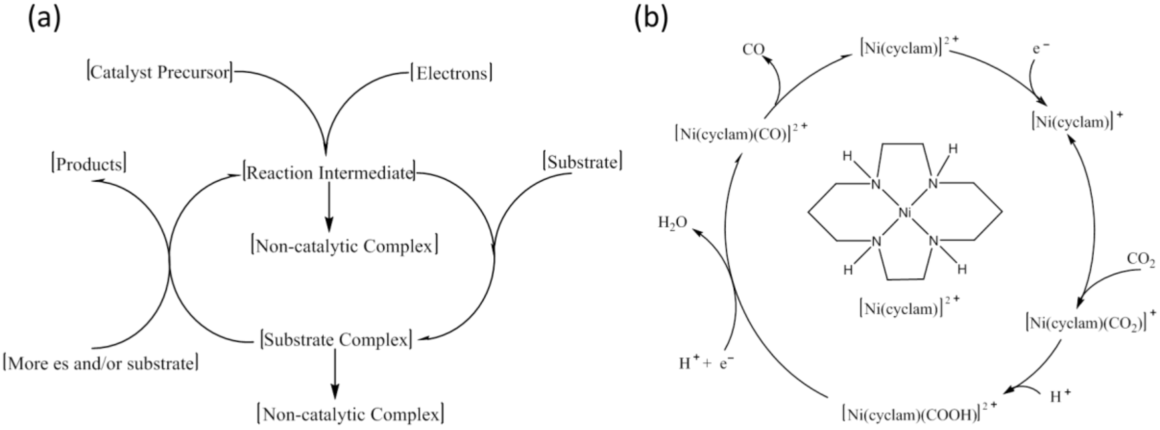

Figure 2.4 (a) The general electro-catalytic cycle for CO_2 reduction on homogeneous catalyst. (b) CO_2 reduction cycle on $[Ni(cyclam)]^{2+}$.

An example[28] of mechanistic cycle for homogeneous CO_2 reduction on metal complex is shown in Figure 2.4(b). The reaction precursor, nickel complex ($[Ni(cyclam)]^{2+}$), is first reduced to $[Ni(cyclam)]^{+}$ by taking one electron transferred in electrode. The $[Ni(cyclam)]^{+}$, thereby, is the reaction intermediate, as illustrated in Figure 2.4(a). The following step is the CO_2 binding with the reaction intermediate, forming a CO_2 complex. Next, the complex couples one proton in the solution to generate the $[Ni(cyclam)(COOH)]^{2+}$ complex. Following that, the newly formed nickel complex combines with another proton and electron pair to generate a CO complex, with one water molecule getting released. Finally, the carbon monoxide desorbs from the complex, leaving the catalyst precursor $[Ni(cyclam)]^{2+}$.

2.2.2 Non-metal Complexes

Electrochemically, conducting polymers enjoy several intrinsic advantages for catalysis uses, such as ease of synthesis, low cost, and good conductivities (particularly when doping or incorporation of other conducting components).[29,30] Due to the highly conjugated polymeric backbones, in most cases, conducting polymers can undergo rapid and reversible redox process, which is importance for electro-chemical applications.[31,32] In discipline of CO_2 conversion, two kinds of conducting polymers, polypyrrole (PPy) and polyaniline (PAn), have been proposed as electro-catalysts. Aydin et al. explored the CO_2 reduction performance of a PPy cathode under ambient conditions.[33] Significant current densities were observed between -0.3 V to -0.6 V versus Ag/AgCl and three kinds of reduction products (formic acid, formaldehyde, and acetic acid) were obtained. Compared with other homogeneous CO_2 reduction catalysts, although the faradaic efficiencies of CO_2 reduction products are slightly slow (~88% at the first hour), it is the first time that decent acetic acid production was reported. Koleli et al. developed a PAn based electrode and characterized its ability for CO_2 electro-reduction at ambient conditions.[34] Results indicted the reaction performed actively at -0.2 V *vs.* SCE. Still, the faradaic efficiencies were not high, with 12% formic and 78% acetic acid.

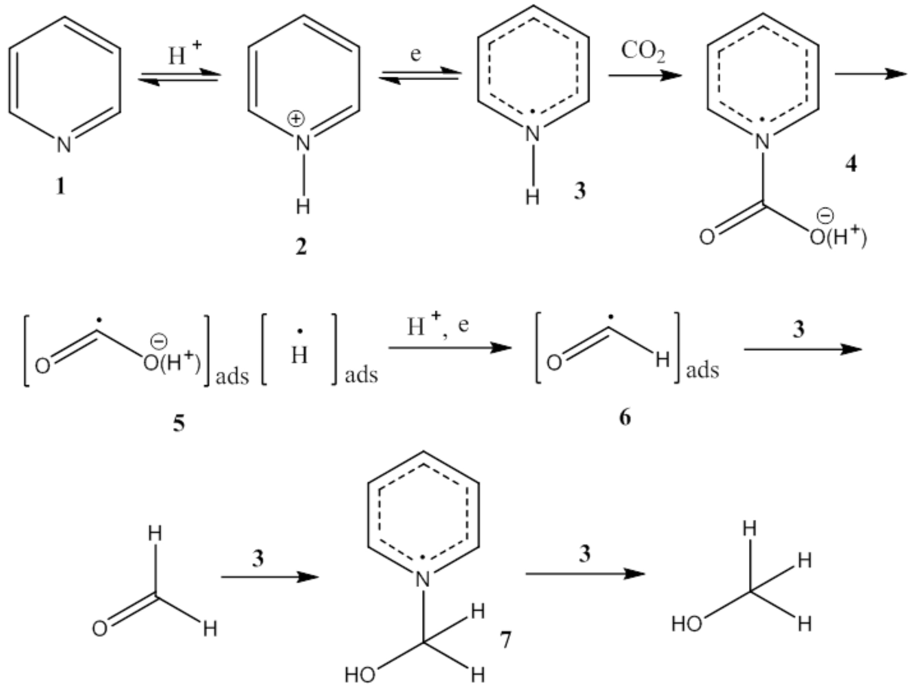

Figure 2.5 Proposed mechanism for pyridinium catalyzed reduction of CO_2 to methanol on Pt electrode.

It was firstly reported by Bocarsly and co-workers that pyridinium can serve as homogeneous CO_2 reduction catalyst when it is coupled to palladium electrode in aqueous solution.[35] Although the side reaction of hydrogen evolution (probably because of the role of Pd electrode) caused large energy loss in the process, the reduction product, methanol, displayed a Faradaic efficiency of 30%. Furthermore, the same research group reported that the substituted derivatives of pyridinium ion can also act as good CO_2 reduction catalyst when combined with Pt or Pd electrode.[36] The reduction reactions began at almost the same potentials with one more product being observed, the formic acid at a Faradaic efficiency of 11%. Ever since then, huge efforts have been spent on gaining the mechanistic view of pyridinium-catalyzed CO_2 reduction process. A plausible mechanism[36] for six-electron reductive conversion process from CO_2 to methanol has been proposed (Figure 2.5). First, the pyridine (1) in an acidic aqueous solution combines a proton to form a protonated pyridine. Subsequently, the newly generated protonated pyridine accepts one electron to form the pyridinyl radical. As the radical shows strong reduction ability, it reacts with carbon dioxide to generate a radical carbonate species (4), which is an important reaction intermediate in the whole process. Next, the carbonate species (4) is converted to a surface-bound hydroxyformyl radical species, which subsequently reacts with an adsorbed proton to generate a formyl radical species (6). Following that, species (6) reacts with the pyridinyl radical, forming HCOH, and this step repeats continuously to generate the final product, CH_3OH.

2.2.3 Summary for Homogeneous CO_2ER Catalysts

Years' efforts have proved that homogeneous catalysts can behave decently in electrochemical CO_2 reduction applications. Kinetically, the high chances of interactions between dissolved CO_2 and catalyst can achieve high reaction rates. Moreover, compared with solid-phase catalysts, the fluidic character of homogeneous molecular catalysts accomplishes a more straightforward approach than modifying the surface to design a suitable catalyst both efficiently and selectively. Based on the mechanistic development, complex structures for specific product have been rationally designed and, in some significant works, the acquired high performance (~100% Faradaic efficiency for CO_2 reduction product) can hardly be obtained by heterogeneous approaches, making the homogeneous techniques valuable for long-term research.

Nevertheless, besides these advantages, some aspects still need to be overcome.[6] First of all, the long-term catalysis stability is inadequate due to the partial decomposition during the conversion process. Secondly, in some cases, the products are also in the liquid phase, requiring tedious subsequent processes to separate the products from the solution. Thirdly, the products of majority of the works are CO and HCOOH, and only several works have reported the generation of hydrocarbons (CH_4 and CH_3OH), making the conversion less meritorious. In addition, selective production for hydrocarbon products requires unambiguous mechanistic insights, which cannot be satisfied so far. Finally, for metal complex catalysts, most approaches must rely on expensive metals (e.g. Ru, Ir, and Re), making the process costly. Therefore, future works are still needed to solve above drawbacks.

2.3 Heterogeneous Catalysts

Heterogeneously catalyzing CO_2 into low-coordinated carbides has been researched since the 19th century. Yet this topic has been systematically investigated in the last three decades.[37] Various products have been reported to be generated at the surface of the cathode materials. The most intensively investigated class of cathode materials is the transition and post-transition metals in either polycrystalline or single-crystalline form. However, as the catalysis ability of pure metallic materials is limited, tremendous efforts have been spent on developing novel catalysts by modifying the structure and composition of the metal surfaces. Besides metal based catalysts, recently, some heterogeneous catalysts that are metal-free have also been reported to efficiently catalyze CO_2 into other carbides.

2.3.1 Transition and Post-transition Metals

Depending on the type of reduction products, according to Hori and co-workers, pure metal electrodes can be classified into three groups (Figure 2.6).[38] Metallic Cu, the only member in the first group, is the unique one displaying the selectivity of hydrocarbons. It was found that the polycrystalline Cu electrodes in aqueous media could yield short-chain hydrocarbons (CH_4 and C_2H_4) with a high current density (~5 mA cm^{-2}) and Faradaic efficiency (~85% in total for CH_4 and C_2H_4). Although the required activation potential was quite high (>1 V *vs*. RHE), this breakthrough made a big step to the dream of making carbon-neutral fuels directly from earth-abundant CO_2. Density functional theory works[39,40] have demonstrated that, of all the commonly used fcc metals, the rate-limiting step for CH_4 formation (from an adsorbed CO species to CHO species) needs the lowest uphill energy gap on Cu surface, making Cu the only one possible to produce CH_4. The second group consists of Ag, Au, Zn, and Pd, which yield carbon monoxide as the main product. However, although the selectivity on these four metals is the same, theoretical work[41-43] has shown that the rate-limiting step of CO formation on Pd surface is different from that on the other three metals. On the Pd surface, the desorption of the chemisorbed CO molecule requires the highest energy input while the formation of adsorbed COOH species determines the reaction rate on Au, Ag and Zn. This difference may lead to different methodologies in tuning the catalytic abilities of these metals. The third class, which includes Pb, Hg, In, Sn, Cd, and Tl, is characterized by the formation of formate as the main product.

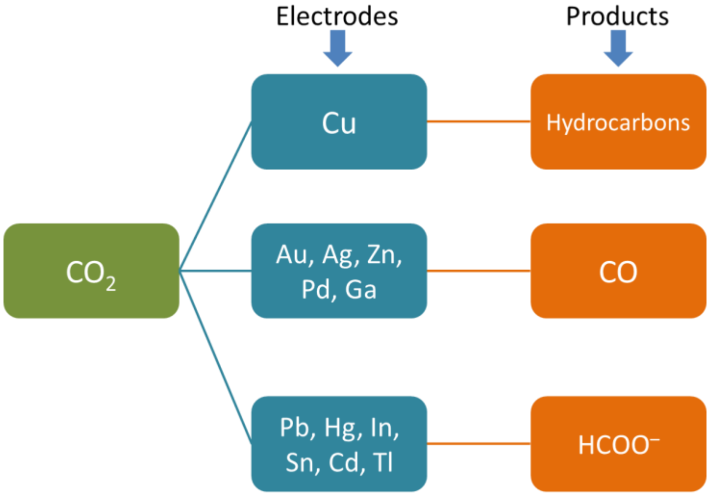

Figure 2.6 Product selectivity of CO_2ER on transition- and post transition-metals.

Nevertheless, it should be mentioned that the structurally simple electrodes were used in Figure 2.6. In fact, due to the poor performances (high overpotential and low energy efficiency) by pure metallic cathodes, structural and compositional modifications are usually applied to improve the catalytic properties of metal electrodes, which, in some cases, may change the reduction selectivity. Catalytically, the surface of a catalyst, which directly provides active sites for the adsorption of intermediates, and charge transfer, plays the key role in deciding the nature of the reaction. Recently, many metallic catalysts with unique structures and/or compositions have been developed for CO_2 electrochemical reduction. They displayed distinct catalytic activities from the corresponding bulk materials, which will be reviewed in the following sections.

2.3.2 Metals with Surface Structural Modifications

Size Effect. Size modification of metal particles is an efficient method used to adjust the binding interactions between the reaction intermediates and catalyst surfaces. Combining both theoretical and experimental approaches, the size effect on Au and Cu NPs has been reported by Strasser and Cuenya.[42,44] The results indicated the current density decreased with the increase of particle size, at certain potentials. Detailed characterization revealed that the numbers of low-coordinated atoms dramatically increased as the particle size shrunk, especially when it was less than 5 nm. Commonly, NPs are considered as an extended and stepped surface, hence, more step- and kink- like sites, containing large numbers of low-coordinated atoms, arise when the size of NPs is decreased.[45] Energetically, DFT calculations (see Figure 2.7) revealed that these low-coordinated atoms had stronger affinities towards the key reaction intermediates (*COOH in this case), thus leading to a lower uphill reaction pathway.[42] Consequently, the product selectivity and reaction activity can differ greatly from the metals in their bulk orientations. Based on Hori's data[46], a Au foil measured at E = -1.22 V *vs.* RHE showed 88.6% Faradaic efficiency toward H_2 and 11.4% toward CO. By contrast, Au particles in 3 nm and 4 nm size displayed ~18% selectivity toward CO under identical conditions. Other works on Pd[41] and Ag[43] particles suggest the same trend. These findings highlight the role of low-coordinated created by small sized particle in the conversion of CO_2.

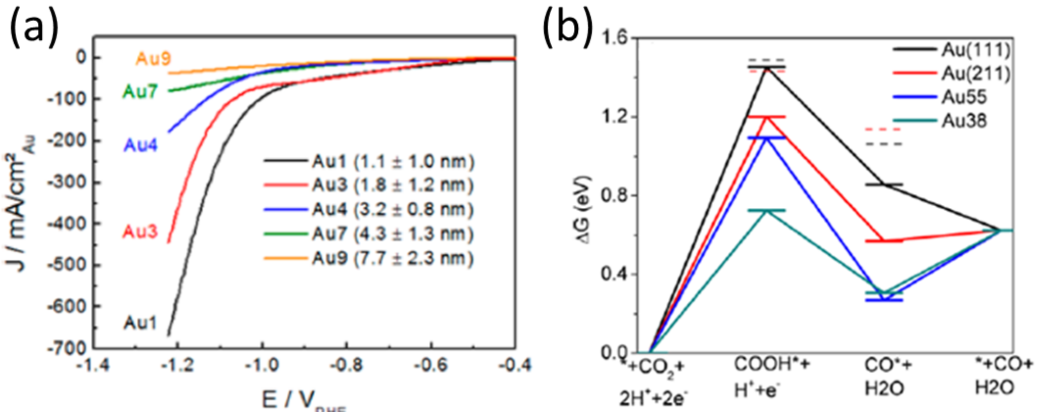

Figure 2.7 (a) Measured current density vs. applied potential for CO_2 on Au particles in different size. (b) Calculated free energy pathway of CO formation on different Au surfaces. Reproduced with permission from ref. 42 © 2014 American Chemical Society.

Metastable Surfaces. Kanan and his group investigated the catalytic performance of oxide derived Au particles towards CO_2 reduction.[47] The Au electrode was prepared by a two-step approach, first oxidizing into AuO_x and then reducing to Au. The derived Au particles showed distinct catalytic abilities from polycrystalline Au. Thermodynamically, on the oxide derived Au electrode, the CO_2 reduction reaction took place at an overpotential of 140 mV and obtained a 98% Faradaic efficiency of CO at the first 2h. By comparison, the reaction happened at the overpotential of more than 200 mV on polycrystalline Au electrode and the Faradaic efficiency of CO was only 40% at the first 2h. The TEM images displayed obvious grain boundaries in particle surface and the Powder X-Ray Diffraction (PXRD) pattern showed peaks of many high-index surfaces (Figure 2.8). Similar approaches[48,49] were also applied on Cu electrode and the same trends were discovered. These results indicated the key role of high-index surfaces for boosting the reduction reaction of CO_2. Geometrically, as atoms in high-index surfaces are all low-coordinated, these results further highlighted the catalytically active atoms with low coordination number.

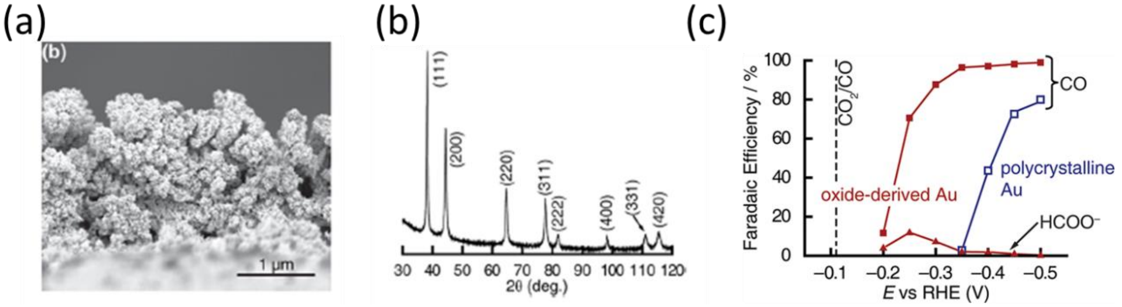

Figure 2.8 (a) SEM image of oxide derived Au particle. (b) PXRD of oxide derived Au particle. (c) Faradaic efficiency on polycrystalline Au and oxide derived Au. Reproduced with permission from ref. 47 © 2012 American Chemical Society.

Morphology Effect. In recent years, as a result of the technological progress in nanofabrication, catalysts with special morphologies and in highly complicated nanostructures have been prepared for CO_2 electroreduction. Branco et al. have studied the catalytic performance of polycrystalline Cu in 3D foam, honeycomb, and dendritic structure.[50] Compared with bulk Cu electrode, which mainly catalyzed CO_2 into CH_4, polycrystalline Cu in these unique morphologies preferred C_2H_4 and C_2H_6 formation. This is because that these surfaces contain numerous amounts of defects that can strongly bind reaction intermediates of C_1 species. As a consequence, the residence time is prolonged, and that leads to higher chances for C-C coupling, resulting in the selectivity of C_2 species. Ki Tae Nam and coworkers synthesized a concave rhombic dodecahedral Au catalyst (Figure 2.9) for CO_2 electro-reduction.[51] The reaction started at an onset potential of -0.23 V *vs.* RHE and the Faradaic efficiency of CO reached as high as 93% at -0.57 V *vs.* RHE. By contrast, reaction started at -0.42 V *vs.* RHE on Au film and scarcely any CO is generated at the same applied potential. Similar phenomenon was found on Ag electrode that nanocoralloid morphology significantly boosted the CO_2 reduction reaction with lowered overpotential and higher CO Faradaic efficiency.[52]

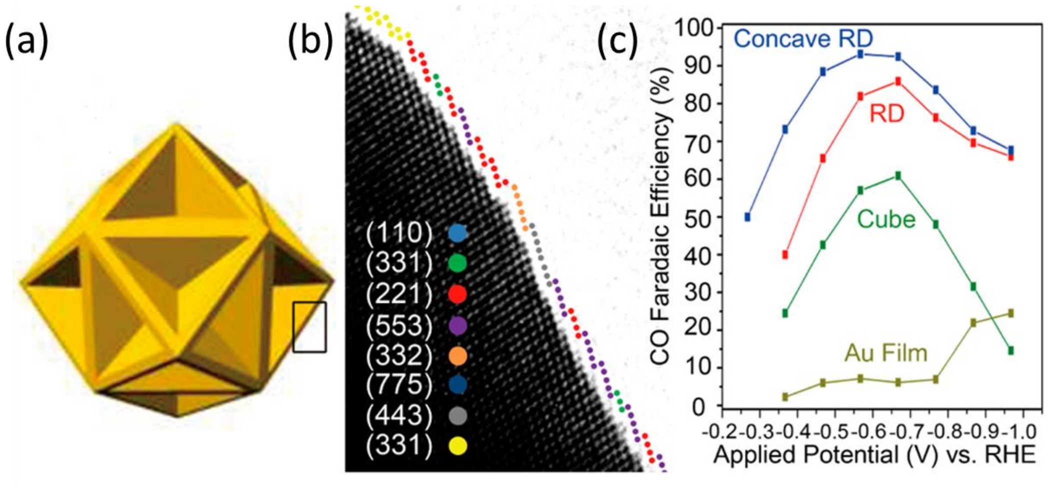

Figure 2.9 (a) Schematic illustration of concave rhombic dodecahedral Au particle. (b) Surface roughness of the concave rhombic dodecahedral Au. (c) CO Faradaic efficiencies on Au catalysts in different morphology. Reproduced with permission from ref. 51 © 2015 American Chemical Society.

Possibly, there are several reasons for the high performance of nnanostructured catalysts: (1) the largely increased specific surface areas that could enhance the anti-poison ability and provide more catalytically active sites, (2) the existence of abundant defective sites on the surfaces, and (3) the open and 3D morphologies that facilitate the mass transfer ability.

Porous Structures. Jiao Feng and coworkers investigated a nanoporous Ag electrode for CO_2 electro-reduction.[53] The highly curved hollow structure showed distinct catalytic property from polycrystalline Ag. On the nanoporous Ag electrode, the CO_2 reduction reaction began at an overpotential of 390 mV and achieved the highest current density of 8 mA cm^{-2}. However, on polycrystalline Ag, the reaction required an overpotential of 490 mV and the current density could only be as high as 0.005 mA cm^{-2}. The enhanced catalytic performance was most probably attributed to the large surface area and the curved internal surface created by the porous structure. The same strategy was applied on Cu electrode and similar trend was found.[54] These results indicate the feasibility of achieving high catalytic ability by creating nanoporous structures.

Summary on Structural Modifications. Tremendous efforts have been spent on improving the catalytic performance of metal catalysts using structural modification approaches. It has been proved that structural modification is a promising approach to design novel catalysts with high activity and selectivity.[55] Methodologically, structural modification directly changes the binding geometry, electronic structure, and adsorption strength of reaction intermediates. However, mechanistic insights of the reaction pathway on the modified surfaces, which is important for future experimental guidance, are still lacking. Based on the four structural modification approaches reviewed, it can be summarized that the intrinsic reasons for the improved catalytic ability are almost the same, i.e. the generated large numbers of low-coordinated atoms serving as catalytically active sites. Unfortunately, although several works have adopted theoretical method to explain the observed phenomenon, a general and systematical explanation, computationally, is still desired to rationally analyze the role of low-coordinated sites in CO_2 electro-catalysis process. Therefore, the first part of the thesis is to give theoretical support to the structural modification approaches by computing the CO_2 reduction reaction on different kinds of low-coordinated Cu sites (see details in Chapter3 & 4).

2.3.3 Metals with Compositional Modifications

Metal Overlayers. Catalysts in metal overlayer structures are prepared by introducing thin foreign metal layers on the host metal substrates. Due to the lattice strain effects and overlayer-substrate electron interactions, compared with the substrate metals, catalytic activities of the overlayer systems can be drastically changed.[56]

Cu, because of the unique properties in its bulk orientations, has been used as overlayers supported on various metal substrates for catalytic improvement. P. Strasser's group investigated the catalytic abilities of Cu overlayers in different thickness (changing from the range of monolayer to 15 nm thickness) supported on the substrate of polycrystalline Pt.[57] As illustrated in Figure 2.10, the ratio of CH_4/C_2H_4 was strongly dependent on the thickness of Cu overlayers, with Cu_{15nm}/Pt system showing the largest one at a wide potential range. The lattice mismatch between pure metallic Pt and Cu was about 9%, making the overlayer Cu under significant tensile strain. Moreover, the electronic structures of the Cu overlayers were also changed as a result of interacting with the substrate Pt metal. These two effects gradually diminished with the increasing of Cu overlayers. Hence, when the overlayer was thick enough, 15 nm for instance, its performance drew near to that of pure Cu. However, the overlayer system may suffer from surface reconstruction due to the strong interactions with reaction intermediates.

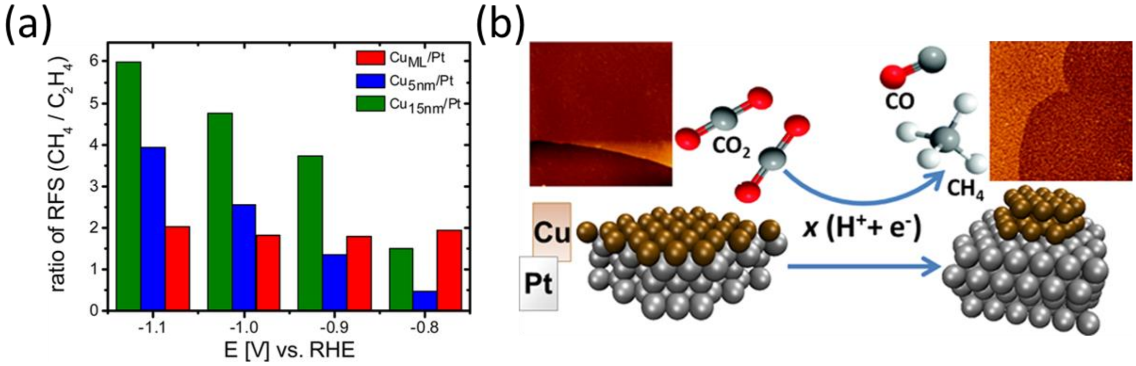

Figure 2.10 (a) Production ratio between CH_4 and C_2H_2 *vs.* applied potential on different Cu/Pt systems. (b) Schematic illustration for the surface reconstruction of monolayer Cu on Pt substrate. Reproduced with permission from ref. 57 and 58 © 2013 American Chemical Society.

In another work, by using in situ electrochemical scanning tunneling microscopy (EC-STM), Chorkendorff and coworkers observed dynamic surface reconstruction of Cu monolayer on Pt(211) and Pt(111).[58] Copper atoms aggregated into islands and parts of the substrate Pt were exposed after capturing CO intermediates (see Figure 2.10), which interacted more strongly with Pt rather than Cu. As Pt is an excellent catalyst towards HER, the Faradaic efficiency of CO_2 reduction products is decreased. Alternatively, adopting DFT approaches S. Back et al. screened the CO_2 reduction pathway on a series of metal overlayer and subsurface systems.[59] Five commonly used substrate metals, Cu, Pd, Au, Ag, and Pt, were chosen as the host metal substrate. Various guest metals, including Cu, Au, Ag, Re, Zn, Pd, Pt, Ir, Rh, W, V, Ta, and Os, were considered as the overlayer and subsurface metals. Taking advantage of the computational hydrogen electrode model, a volcano-like figure was generated (Figure 2.11), which predicted that the W/Cu subsurface system displayed the lowest energetic path to form CH_3OH. Several other overlayer/substrate combinations, such as Pd/Au[60] and Ag/Au[61], have also been explored. Besides the poor stability issues, it has been proved that overlayer approach is a useful method to design a catalyst with motivated selectivity.

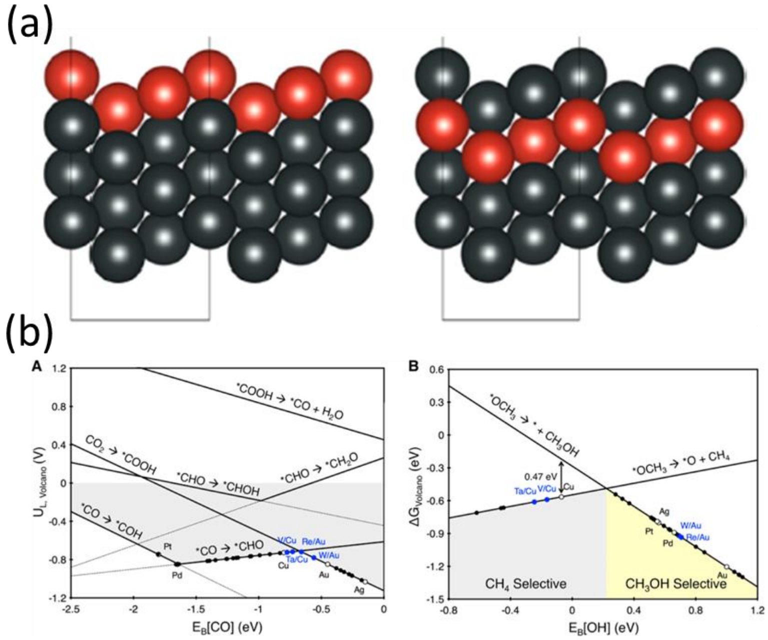

Figure 2.11 (a) Side view of two metal-metal overlayer systems. The left one is a system with one-layer guest metal coated on the substrate one. The right one is a near-surface alloy (NSA) with the second layer to be guest metals. (b) Plotted volcano plot on the designed systems. The figure plots the predicted limiting potential ($U_{L,volcano}$) as a function of the binding energy of CO and OH. In this figure, each line represents one elementary step involved in CO_2ER. The CH_3OH production is preferred at weaker (less negative) OH binding energies. In total, 27 stable NSAs and pure metals are calculated in the study. Those NSAs that are located close to the top of CO-analogous volcano (i.e., between Cu and Au) are marked in blue. Reproduced with permission from ref. 59 © 2015 American Chemical Society.

Alloy. Alloying approach has been long used as an effective method to tune the catalytic ability of metals. Cu-Au alloys with different compositions have been intensively explored in recent years.[62,63] Different from pure metallic Au, Au_3Cu NPs yielded more hydrogen and hydrocarbons with less CO production. Bulk Au is a commonly used catalyst for CO production, as *CHO species can hardly be formed, preventing the further hydrogenation process of adsorbed *CO intermediate. However, since Cu has a much higher affinity towards *CHO formation, the presence of Cu atoms on Au surface can stabilize *CHO and facilitate its further reduction into hydrocarbons.

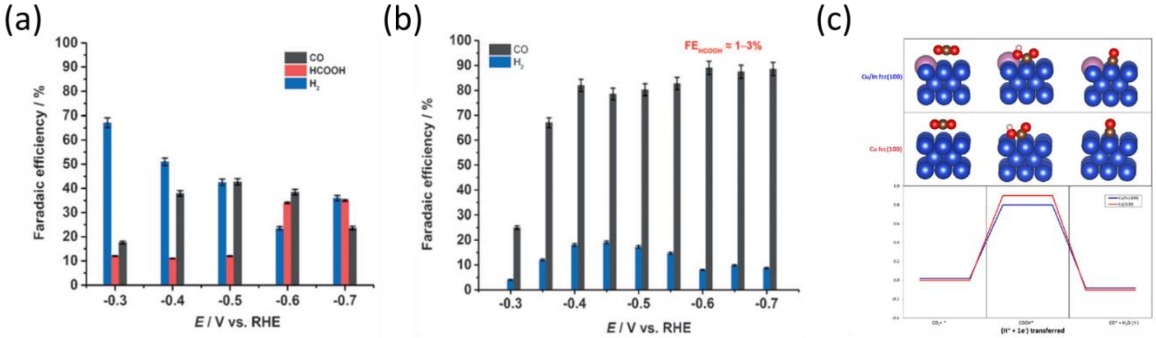

Figure 2.12 (a) Faradaic efficiency of CO_2ER on 0D copper. The bars in black, red, and blue represent CO, HCOOH, and H_2, respectively. The data is analyzed at –0.6 V *vs.* RHE in 0.1 M $KHCO_3/CO_2$. (b) Faradaic efficiency of CO_2ER on In doped Cu. The bars in black and blue represent CO and H_2, respectively. (c) Computed Free energy pathway on Cu(100) and In doped Cu(100). The reaction is CO_2ER to CO via a *COOH intermediate. The red line represents free energy pathway of clean Cu(100), while the blue line stands for the path on In doped Cu(100). The configurations of the corresponding states are also illustrated in the upper level. Reproduced with permission from ref. 67 © 2014 Wiley-VCH Verlag GmbH & Co.

Detailed study by Yang Peidong's group showed that two factors simultaneously affected the catalytic abilities of Cu-Au alloys.[64] First, alloys with different Cu/Au ratio will display different d-band center, affecting the binding strengths for various intermediates. Second, as *COOH bound the surface through two atoms (one C atom and one O atom), more chances would be created for the bimetallic surface to interact with it; hence, compared with *CO intermediate, which bound the surface only through one C atom, binding energies of *COOH species would be more sensible to the Cu/Au ratio. Consequently, these two aspects worked synergistically, making the Cu-Au alloy displaying different selectivity from the bulk Au or Cu electrode. The unique product selectivity created by the balanced binding affinities of Cu_3Au alloy was also computationally confirmed in a theoretical work reported by Hirunsit and coworkers.[65] More importantly, in the follow-up work[66] by Hirunsit, the methane and methanol formation on a series of Cu based alloys have been investigated. Of all the researched systems, only Cu_3Pd and Cu_3Pt favored the production of methanol. The other Cu alloys, Cu_3Ni, Cu_3Co, Cu_3Rh, Cu_3Ag, Cu_3Ir, and Cu_3Au, were all predicted to produce CH_4. Other alloyed systems, mainly based on Pt, have also been reported by various groups and unique product selectivity was found in Pt-Cu, Pt-Ru, and Pt-Pd systems. By adjusting the ratio between the two alloyed metals, it is believed that the selectivity of CO_2 reduction reaction can be dramatically tuned and forming only one targeted product is the long-term motivation for this approach.

Doped Metals. So far, although only several attempts have been tried by using doped bimetallic systems; some of the findings are appealing. Analogous to the alloying approach, doping with foreign metals can create unique bimetallic surface, which could provide modified binding sites for the reactants and intermediates.[55] Takanabe and coworkers investigated an In doped Cu electrode and compared its catalytic performance with 0D Cu particles.[67] In the tested potential range (0 V – -0.7 V *vs.* RHE), 0D Cu particles[48] showed 40% product selectivity for CO and 30% for HCOOH (the remaining part was H_2); by contrast, In doped Cu displayed a 90% Faradaic efficiency for CO and negligible production of HCOOH. The peak FE occurred at -0.7 V *vs.* RHE on 0D Cu, while on In doped Cu, only -0.5 V *vs.* RHE was needed to generate the highest energy conversion peak. Mechanistically, in order to explain the experimentally observed phenomenon, in the same report, the authors computed the CO formation pathway on both clean and In doped Cu surface (Figure 2.12). Energetically, after doping In into the Cu surface, the energy needed to activate the rate limiting step of CO formation (from CO_2 to an adsorbed *COOH species) was decreased evidently. This would lead to higher chances for CO formation reaction and thus modified product selectivity. This work highlighted the doping treatment for rationally designing electro-catalysts toward CO_2 reduction. Inspired by this breakthrough, more recently, systems of Sn[68], Co[69], Pt[70], and Ni[70] doped Cu systems have been studied to modify the selectivity of Cu electrode. Although more detailed mechanistic insights are still needed to guide further experimental synthesis, the doping method shows full potentials to be used as effective approach in designing excellent CO_2 electro-catalysts with targeted selectivity.

Summary on Compositional Modifications. Great efforts have been paid on compositional modifications and some of the results show outstanding potentials. The major issues and challenges associated with compositional approaches are the lack of mechanistic insights, which can provide guidance for experimental designs toward enhanced catalytic performance. Based on computational tools, although some pioneer works have been done to predict good catalysts in overlayer system[59] and alloying system[65,66], predictions of doped system are still in keen need. Hence, the second part of the thesis is to give theoretical predictions for the catalytic abilities of a series of doped systems with the substrate of Au, Ag, and Cu(see details in Chapter3 & 5).

2.3.4 Metal Composites

Metal Oxides. Recently, it is surprising that some believed low-performance metals show excellent catalytic activity in their oxide forms. Bocarsly and coworkers found that In-OH, rather than metallic In, was the real active site for producing formate in aqueous solution.[71] Hydroxide or oxide was also considered to be necessary on Pb surface to facilitate CO_2ER and suppress HER.[72] Similarly, another report by Kanan's group observed ~99% CO_2 reduction efficiency on SnO_x electrode in the low overpotential region, while only HER activity was showed on acid-etched Sn (oxide-free) catalyst.[73] Another intriguing system was reported by Sekimoto and coworkers.[74] It is believed that pure Ga is a low-efficient CO_2ER catalyst. Nevertheless, the oxide Ga_2O_3 was found to selectively generate as high as 80% formic acid in a 3.0 M KCl solution due to the preferred intermediate of *OCHO rather than *COOH, which was believed as advantageous to form formic acid. It should be mentioned that although Si and Sn doping were necessary in order to enhance the conductivity of Ga_2O_3, their trace amounts did not influence the catalytic activity significantly.

Metal Dichalcogenides. MoS_2 has been studied as effective HER catalyst[75,76], however, MoS_2 is also reported to serve as efficient CO_2 reduction catalyst. Asadi et al. investigated the catalytic behavior of layer-stacked bulk MoS_2 toward CO_2 electro-reduction.[77] A reasonable current density (65 mA cm^{-2} when overpotential was 0.65 V) and a low onset potential (54 mV) with 98% carbon monoxide efficiency were observed, which were far more desirable than most metal catalysts. The solution of ionic liquid electrolyte (EMIM-BF_4) was believed to play a crucial role in inhibiting HER and recuing the activation barrier for electron transfer. Moreover, the performance of Ag electrode, which was considered as a good CO formation catalyst, in the same electrolyte, was much poorer, indicating the unique catalytic behavior of MoS_2. Furthermore, Salehi-Khojin and coworkers found a series of transition metal dichalcogenide (MoS_2, $MoSe_2$, WS_2, and WSe_2) could behave actively as CO_2 electro-reduction catalysts, with the CO Faradaic efficiency being as high as 24%.[78] The calculated free energy diagram revealed that the metal dichalgenides showed lower energies that the normally used Ag catalyst (see Figure 2.13). More importantly, adopting computational tools, Kim and coworkers screened the CO_2 reduction performance on 61 2D covalent metals.[79] It was found that the covalent nature of the catalyst surface of 2D materials specifically stabilized COOH while keeping nearly zero affinity for CO, breaking the pre-existing scaling relationship between the COOH and CO binding energies of metals. This breakthrough suggested a strategy for overcoming the intrinsic limitations of metals or metal alloys, by expanding the domain of materials for CO_2 reduction electro-catalysts into a new realm of 2D covalent metals.

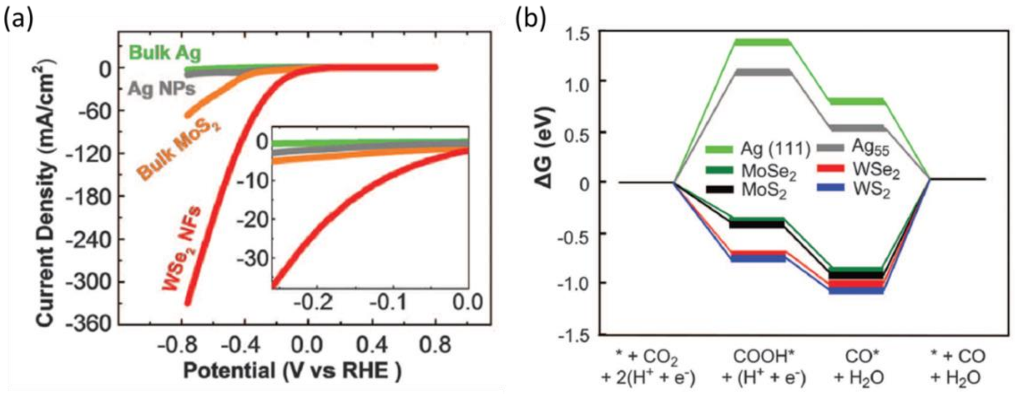

Figure 2.13 (a) Current density vs. applied potential on WSe_2 nanoflakes and other catalysts. (b) Computed free energy pathway on metal dichalcogenides and Ag surfaces. Reproduced with permission from ref. 78 © 2016 American Association for the Advancement of Science.

2.3.5 Carbon-based Catalysts

Single-layer carbon material and its derivatives have been long researched as electro-catalysts.[55] However, pure single layer graphene is chemically inert for CO_2 electroreduction reaction as no binding sites on graphene can serve actively for activating the adsorption of CO_2.[80] The first carbon-based material serving as electro-chemical CO_2 reduction catalyst was reported by Salehi-Khojin's group.[81] By doping nitrogen atom into the lattice of carbon nanofibers (CNFs), CO_2 was selectively catalyzed into CO with a 98% Faradaic efficiency. Although the authors failed to define the form of doped nitrogen atoms, it was believed that the locally doped sites were responsible for the catalytic performance.

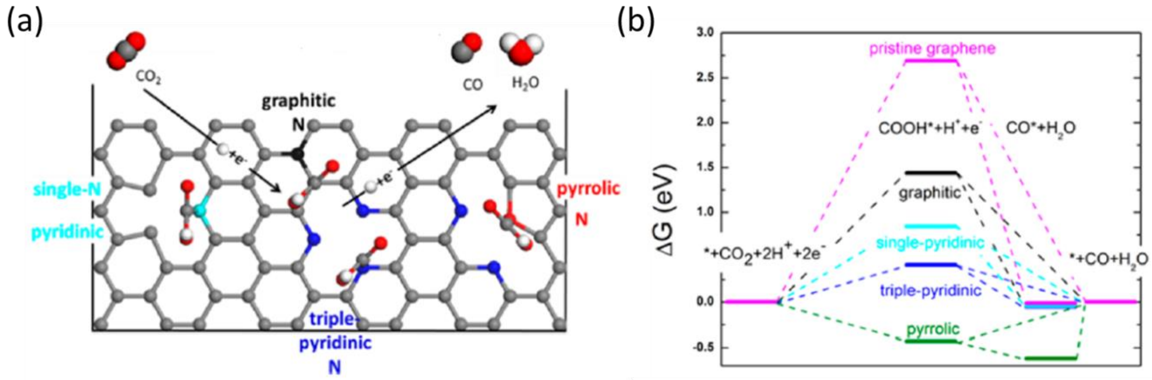

Figure 2.14 (a) Schematic of different kinds of doped N in the carbon lattice. (b) Computed free energy pathway on these doped N sites. Reproduced with permission from ref. 59 © 2016 American Chemical Society.

Following this, a more detailed work by Ajayan's group characterized three kinds of doped nitrogen in the lattice of carbon nanotube, pyridinic-N, pyrrolic-N, and graphitic-N (Figure 2.14).[82] In order to find out which of these three N atoms played the dominant role in the catalytic process, later work performed by the same group combined both experimental and computational tools.[83] Experimentally, four samples of nitrogen-doped graphene (NG) were synthesized under different temperatures. The temperature was used to tune the ratio of these three N atoms in the graphene lattice. The maximum FE and the corresponding potential shared the same trend as the content of pyridinic-N when plotted as a function of the concentration of different NG catalysts. However, no such a trend was observed for pydolic- or graphitic-N. The authors then computed the CO reaction pathway on these three doped sites. The figure of reaction coordinate indicated the triple-pyridinic N site showed the lowest energy difference between the states of *COOH and gaseous CO_2. This result strongly supported the experimentally observed phenomenon and hence, pyridinic-N was believed to play the dominant role in the CO formation process.

References

1 Agarwal, A. S., Zhai, Y., Hill, D. & Sridhar, N. The Electrochemical Reduction of Carbon Dioxide to Formate/Formic Acid: Engineering and Economic Feasibility. *ChemSusChem* **4**, 1301-1310 (2011).

2 Halmann, M. M. & Steinberg, M. *Greenhouse gas carbon dioxide mitigation: science and technology*. (CRC press, 1998).

3 Qiao, J., Liu, Y., Hong, F. & Zhang, J. A review of catalysts for the electroreduction of carbon dioxide to produce low-carbon fuels. *Chemical Society Reviews* **43**, 631-675 (2014).

4 Sullivan, B. P., Krist, K. & Guard, H. *Electrochemical and electrocatalytic reactions of carbon dioxide*. (Elsevier, 2012).

5 Collin, J. & Sauvage, J. Electrochemical reduction of carbon dioxide mediated by molecular catalysts. *Coordination Chemistry Reviews* **93**, 245-268 (1989).

6 Van Leeuwen, P. W. *Homogeneous catalysis: understanding the art*. (Springer Science & Business Media, 2006).

7 Aresta, M., Nobile, C. F., Albano, V. G., Forni, E. & Manassero, M. New nickel-carbon dioxide complex: synthesis, properties, and crystallographic characterization of (carbon dioxide)-bis(tricyclohexylphosphine)nickel. *Journal of the Chemical Society, Chemical Communications*, 636-637 (1975).

8 Fisher, B. J. & Eisenberg, R. Electrocatalytic reduction of carbon dioxide by using macrocycles of nickel and cobalt. *Journal of the American Chemical Society* **102**, 7361-7363 (1980).

9 Benson, E. E., Kubiak, C. P., Sathrum, A. J. & Smieja, J. M. Electrocatalytic and homogeneous approaches to conversion of CO_2 to liquid fuels. *Chemical Society Reviews* **38**, 89-99 (2009).

10 Elgrishi, N., Chambers, M. B. & Fontecave, M. Turning it off! Disfavouring hydrogen evolution to enhance selectivity for CO production during

homogeneous CO_2 reduction by cobalt–terpyridine complexes. *Chemical Science* **6**, 2522-2531 (2015).

11 Jeletic, M. S., Mock, M. T., Appel, A. M. & Linehan, J. C. A cobalt-based catalyst for the hydrogenation of CO_2 under ambient conditions. *Journal of the American Chemical Society* **135**, 11533-11536 (2013).

12 Froehlich, J. D. & Kubiak, C. P. Homogeneous CO2 reduction by Ni (cyclam) at a glassy carbon electrode. *Inorganic Chemistry* **51**, 3932-3934 (2012).

13 Collin, J. P., Jouaiti, A. & Sauvage, J. P. Electrocatalytic properties of (tetraazacyclotetradecane) nickel (2+) and Ni2 (biscyclam) 4+ with respect to carbon dioxide and water reduction. *Inorganic Chemistry* **27**, 1986-1990 (1988).

14 Keith, J. A., Grice, K. A., Kubiak, C. P. & Carter, E. A. Elucidation of the selectivity of proton-dependent electrocatalytic CO_2 reduction by fac-Re (bpy)(CO) 3Cl. *Journal of the American Chemical Society* **135**, 15823-15829 (2013).

15 Cosnier, S., Deronzier, A. & Moutet, J.-C. Electrocatalytic reduction of CO 2 on electrodes modified by fac-Re (2, 2'-bipyridine)(CO) 3 Cl complexes bonded to polypyrrole films. *Journal of molecular catalysis* **45**, 381-391 (1988).

16 O'Toole, T. R. *et al.* Electrocatalytic reduction of CO2 by a complex of rhenium in thin polymeric films. *Journal of Electroanalytical Chemistry and Interfacial Electrochemistry* **259**, 217-239 (1989).

17 Kang, P., Chen, Z., Nayak, A., Zhang, S. & Meyer, T. J. Single catalyst electrocatalytic reduction of CO_2 in water to H_2+ CO syngas mixtures with water oxidation to O_2. *Energy & Environmental Science* **7**, 4007-4012 (2014).

18 Ishida, H., Tanaka, K. & Tanaka, T. Electrochemical CO_2 reduction catalyzed by ruthenium complexes [Ru (bpy) 2 (CO) 2] 2+ and [Ru (bpy) 2 (CO) Cl]+. Effect of pH on the formation of CO and HCOO. *Organometallics* **6**, 181-186 (1987).

19 Chardon-Noblat, S., Deronzier, A., Ziessel, R. & Zsoldos, D. Selective Synthesis and Electrochemical Behavior of trans (Cl)-and cis (Cl)-[Ru (bpy)(CO) 2Cl2] Complexes (bpy= 2, 2'-Bipyridine). Comparative Studies of Their Electrocatalytic Activity toward the Reduction of Carbon Dioxide. *Inorganic Chemistry* **36**, 5384-5389 (1997).

20 Bourrez, M., Molton, F., Chardon-Noblat, S. & Deronzier, A. [Mn (bipyridyl)(CO) 3Br]: An abundant metal carbonyl complex as efficient electrocatalyst for CO_2 reduction. *Angewandte Chemie* **123**, 10077-10080 (2011).

21 Smieja, J. M. *et al.* Manganese as a substitute for rhenium in CO_2 reduction catalysts: The importance of acids. *Inorganic Chemistry* **52**, 2484-2491 (2013).

22 Tornow, C. E., Thorson, M. R., Ma, S., Gewirth, A. A. & Kenis, P. J. Nitrogen-based catalysts for the electrochemical reduction of CO_2 to CO. *Journal of the American Chemical Society* **134**, 19520-19523 (2012).

23 Angamuthu, R., Byers, P., Lutz, M., Spek, A. L. & Bouwman, E. Electrocatalytic CO_2 conversion to oxalate by a copper complex. *Science* **327**, 313-315 (2010).

24 Schrebler, R., Cury, P., Herrera, F., Gomez, H. & Cordova, R. Study of the electrochemical reduction of CO_2 on electrodeposited rhenium electrodes in methanol media. *Journal of Electroanalytical Chemistry* **516**, 23-30 (2001).

25 áMeser Ali, M. Selective formation of HCO 2–and C 2 O 4 2–in electrochemical reduction of CO_2 catalyzed by mono-and di-nuclear ruthenium complexes. *Chemical Communications*, **0**, 249-250 (1998).

26 Ramos Sende, J. *et al.* Electrocatalysis of CO_2 reduction in aqueous media at electrodes modified with electropolymerized films of vinylterpyridine complexes of transition metals. *Inorganic Chemistry* **34**, 3339-3348 (1995).

27 Finn, C., Schnittger, S., Yellowlees, L. J. & Love, J. B. Molecular approaches to the electrochemical reduction of carbon dioxide. *Chemical Communications* **48**, 1392-1399 (2012).

28 Froehlich, J. D. & Kubiak, C. P. The Homogeneous Reduction of CO_2 by [Ni (cyclam)]+: Increased Catalytic Rates with the Addition of a CO Scavenger. *Journal of the American Chemical Society* **137**, 3565-3573 (2015).

29 Liangliang, T. & Chunyang, J. Conducting polymers as electrode materials for supercapacitors. *Progress in Chemistry* **22**, 1610-1618 (2010).

30 Zhang, W.-J. A review of the electrochemical performance of alloy anodes for lithium-ion batteries. *Journal of Power Sources* **196**, 13-24 (2011).

31 Zheng, L. *et al.* The preparation and performance of flocculent polyaniline/carbon nanotubes composite electrode material for supercapacitors. *Journal of Solid State Electrochemistry* **15**, 675-681 (2011).

32 Sivaraman, P. *et al.* All solid supercapacitor based on polyaniline and crosslinked sulfonated poly [ether ether ketone]. *Electrochimica Acta* **55**, 2451-2456 (2010).

33 Aydin, R. & Köleli, F. Electrocatalytic conversion of CO_2 on a polypyrrole electrode under high pressure in methanol. *Synthetic Metals* **144**, 75-80 (2004).

34 Köleli, F., Röpke, T. & Hamann, C. H. The reduction of CO_2 on polyaniline electrode in a membrane cell. *Synthetic Metals* **140**, 65-68 (2004).

35 Seshadri, G., Lin, C. & Bocarsly, A. B. A new homogeneous electrocatalyst for the reduction of carbon dioxide to methanol at low overpotential. *Journal of Electroanalytical Chemistry* **372**, 145-150 (1994).

36 Barton Cole, E. *et al.* Using a one-electron shuttle for the multielectron reduction of CO_2 to methanol: kinetic, mechanistic, and structural insights. *Journal of the American Chemical Society* **132**, 11539-11551 (2010).

37 Kondratenko, E. V., Mul, G., Baltrusaitis, J., Larrazábal, G. O. & Pérez-Ramírez, J. Status and perspectives of CO_2 conversion into fuels and chemicals by catalytic, photocatalytic and electrocatalytic processes. *Energy & Environmental Science* **6**, 3112-3135 (2013).

38 Hori, Y. CO2-reduction, catalyzed by metal electrodes. *Handbook of fuel cells* (2003).

39 Peterson, A. A., Abild-Pedersen, F., Studt, F., Rossmeisl, J. & Nørskov, J. K. How copper catalyzes the electroreduction of carbon dioxide into hydrocarbon fuels. *Energy & Environmental Science* **3**, 1311-1315 (2010).

40 Peterson, A. A. & Nørskov, J. K. Activity descriptors for CO2 electroreduction to methane on transition-metal catalysts. *The Journal of Physical Chemistry Letters* **3**, 251-258 (2012).

41 Gao, D. *et al.* Size-dependent electrocatalytic reduction of CO_2 over Pd nanoparticles. *Journal of the American Chemical Society* **137**, 4288-4291 (2015).

42 Mistry, H. *et al.* Exceptional size-dependent activity enhancement in the electroreduction of CO_2 over Au nanoparticles. *Journal of the American Chemical Society* **136**, 16473-16476 (2014).

43 Rosen, J. *et al.* Mechanistic insights into the electrochemical reduction of CO_2 to CO on nanostructured Ag surfaces. *ACS Catalysis* **5**, 4293-4299 (2015).

44 Reske, R., Mistry, H., Behafarid, F., Roldan Cuenya, B. & Strasser, P. Particle size effects in the catalytic electroreduction of CO_2 on Cu nanoparticles. *Journal of the American Chemical Society* **136**, 6978-6986 (2014).

45 Haruta, M. Spiers memorial lecture role of perimeter interfaces in catalysis by gold nanoparticles. *Faraday Discussions* **152**, 11-32 (2011).

46 Hori, Y., Kikuchi, K. & Suzuki, S. Production of CO and CH_4 in electrochemical reduction of CO_2 at metal electrodes in aqueous hydrogencarbonate solution. *Chemistry Letters*, **14**, 1695-1698 (1985).

47 Chen, Y., Li, C. W. & Kanan, M. W. Aqueous CO_2 reduction at very low overpotential on oxide-derived Au nanoparticles. *Journal of the American Chemical Society* **134**, 19969-19972 (2012).

48 Li, C. W. & Kanan, M. W. CO_2 reduction at low overpotential on Cu electrodes resulting from the reduction of thick Cu_2O films. *Journal of the American Chemical Society* **134**, 7231-7234 (2012).

49 Li, C. W., Ciston, J. & Kanan, M. W. Electroreduction of carbon monoxide to liquid fuel on oxide-derived nanocrystalline copper. *Nature* **508**, 504-507 (2014).

50 Goncalves, M. *et al.* Selective electrochemical conversion of CO_2 to C2 hydrocarbons. *Energy Conversion and Management* **51**, 30-32 (2010).

51 Lee, H.-E. *et al.* Concave Rhombic Dodecahedral Au Nanocatalyst with Multiple High-Index Facets for CO_2 Reduction. *ACS Nano* **9**, 8384-8393 (2015).

52 Hsieh, Y.-C., Senanayake, S. D., Zhang, Y., Xu, W. & Polyansky, D. E. Effect of chloride anions on the synthesis and enhanced catalytic activity of silver nanocoral electrodes for CO_2 electroreduction. *ACS Catalysis* **5**, 5349-5356 (2015).

53 Lu, Q. *et al.* A selective and efficient electrocatalyst for carbon dioxide reduction. *Nature Communications* **5** 3242 (2014).

54 Kas, R. *et al.* Three-dimensional porous hollow fibre copper electrodes for efficient and high-rate electrochemical carbon dioxide reduction. *Nature Communications* **7** 10748 (2016).

55 Zhu, S. & Shao, M. Surface structure and composition effects on electrochemical reduction of carbon dioxide. *Journal of Solid State Electrochemistry* **20**, 861-873 (2016).

56 Mavrikakis, M., Hammer, B. & Nørskov, J. K. Effect of strain on the reactivity of metal surfaces. *Physical Review Letters* **81**, 2819 (1998).

57 Reske, R. *et al.* Controlling catalytic selectivities during CO_2 electroreduction on thin Cu metal overlayers. *The Journal of Physical Chemistry Letters* **4**, 2410-2413 (2013).

58 Varela, A. S. *et al.* CO_2 electroreduction on well-defined bimetallic surfaces: Cu overlayers on Pt (111) and Pt (211). *The Journal of Physical Chemistry C* **117**, 20500-20508 (2013).

59 Back, S., Kim, H. & Jung, Y. Selective heterogeneous CO_2 electroreduction to methanol. *ACS Catalysis* **5**, 965-971 (2015).

60 Plana, D., Flórez-Montano, J., Celorrio, V., Pastor, E. & Fermín, D. J. Tuning CO 2 electroreduction efficiency at Pd shells on Au nanocores. *Chemical Communications* **49**, 10962-10964 (2013).

61 Lates, V., Falch, A., Jordaan, A., Peach, R. & Kriek, R. An electrochemical study of carbon dioxide electroreduction on gold-based nanoparticle catalysts. *Electrochimica Acta* **128**, 75-84 (2014).

62 Zhao, W., Yang, L., Yin, Y. & Jin, M. Thermodynamic controlled synthesis of intermetallic Au 3 Cu alloy nanocrystals from Cu microparticles. *Journal of Materials Chemistry A* **2**, 902-906 (2014).

63 Christophe, J., Doneux, T. & Buess-Herman, C. Electroreduction of carbon dioxide on copper-based electrodes: activity of copper single crystals and copper–gold alloys. *Electrocatalysis* **3**, 139-146 (2012).

64 Kim, D., Resasco, J., Yu, Y., Asiri, A. M. & Yang, P. Synergistic geometric and electronic effects for electrochemical reduction of carbon dioxide using gold–copper bimetallic nanoparticles. *Nature Communications* **5** 4948 (2014).

65 Hirunsit, P. Electroreduction of carbon dioxide to methane on copper, copper–silver, and copper–gold catalysts: a DFT study. *The Journal of Physical Chemistry C* **117**, 8262-8268 (2013).

66 Hirunsit, P., Soodsawang, W. & Limtrakul, J. CO_2 Electrochemical Reduction to Methane and Methanol on Copper-Based Alloys: Theoretical Insight. *The Journal of Physical Chemistry C* **119**, 8238-8249 (2015).

67 Rasul, S. *et al.* A Highly Selective Copper–Indium Bimetallic Electrocatalyst for the Electrochemical Reduction of Aqueous CO_2 to CO. *Angewandte Chemie* **127**, 2174-2178 (2015).

68 Sarfraz, S., Garcia-Esparza, A. T., Jedidi, A., Cavallo, L. & Takanabe, K. Cu–Sn Bimetallic Catalyst for Selective Aqueous Electroreduction of CO_2 to CO. *ACS Catalysis* **6**, 2842-2851 (2016).

69 Grote, J.-P. *et al.* Screening of material libraries for electrochemical CO_2 reduction catalysts–Improving selectivity of Cu by mixing with Co. *Journal of Catalysis* **343**, 248-256 (2016).

70 Todoroki, N., Yokota, N., Nakahata, S., Nakamura, H. & Wadayama, T. Electrochemical Reduction of CO_2 on Ni-and Pt-Epitaxially Grown Cu (111) Surfaces. *Electrocatalysis* **7**, 97-103 (2016).

71 Detweiler, Z. M., White, J. L., Bernasek, S. L. & Bocarsly, A. B. Anodized indium metal electrodes for enhanced carbon dioxide reduction in aqueous electrolyte. *Langmuir* **30**, 7593-7600 (2014).

72 Lee, C. H. & Kanan, M. W. Controlling H^+ vs CO_2 reduction selectivity on Pb electrodes. *ACS Catalysis* **5**, 465-469 (2014).

73 Chen, Y. & Kanan, M. W. Tin oxide dependence of the CO2 reduction efficiency on tin electrodes and enhanced activity for tin/tin oxide thin-film catalysts. *Journal of the American Chemical Society* **134**, 1986-1989 (2012).

74 Sekimoto, T. *et al.* Highly selective electrochemical reduction of CO_2 to HCOOH on a gallium oxide cathode. *Electrochemistry Communications* **43**, 95-97 (2014).

75 Hinnemann, B. *et al.* Biomimetic hydrogen evolution: MoS_2 nanoparticles as catalyst for hydrogen evolution. *Journal of the American Chemical Society* **127**, 5308-5309 (2005).

76 Jaramillo, T. F. *et al.* Identification of active edge sites for electrochemical H_2 evolution from MoS_2 nanocatalysts. *Science* **317**, 100-102 (2007).

77 Asadi, M. *et al.* Robust carbon dioxide reduction on molybdenum disulphide edges. *Nature Communications* **5** 4470 (2014).

78 Asadi, M. *et al.* Nanostructured transition metal dichalcogenide electrocatalysts for CO_2 reduction in ionic liquid. *Science* **353**, 467-470 (2016).

79 Shin, H., Ha, Y. & Kim, H. 2D Covalent Metals: A New Materials Domain of Electrochemical CO_2 Conversion with Broken Scaling Relationship. *The Journal of Physical Chemistry Letters* **7**, 4124-4129 (2016).

80 Pykal, M., Jurečka, P., Karlický, F. & Otyepka, M. Modelling of graphene functionalization. *Physical Chemistry Chemical Physics* **18**, 6351-6372 (2016).

81 Kumar, B. *et al.* Renewable and metal-free carbon nanofibre catalysts for carbon dioxide reduction. *Nature Communications* **4** 2819 (2013).

82 Wu, J. *et al.* Achieving Highly Efficient, Selective, and Stable CO_2 Reduction on Nitrogen-Doped Carbon Nanotubes. *ACS Nano* **9**, 5364-5371 (2015).

83 Wu, J. *et al.* Incorporation of Nitrogen Defects for Efficient Reduction of CO_2 via Two-Electron Pathway on Three-Dimensional Graphene Foam. *Nano Letters* **16**, 466-470 (2015).

Chapter 3

Computational Methodology

This chapter begins with an overview of the strategy used to computationally predict new catalysts with effective activity. It also introduces the fundamental theories behind the theoretical surface catalysis: the role of catalyst, the Sabatier Principle to evaluate catalyst activity, the d-band center theory to estimate the binding affinity, the scaling relations to help rapidly screen the adsorption energy, and the Brønsted–Evans–Polanyi (BEP) principle to link the reaction energy to the activation energy. The methods used to describe the electronic structure of many-body system and the models employed to simulate the catalyst surfaces are concisely presented. Finally, the mechanism and theoretical descriptor of the two investigated reactions, the CO_2 *electro-reduction (*CO_2*ER) reaction and the competing hydrogen evolution reaction (HER), are explicitly elucidated.*

3.1 Overview of the Strategy

Converting the green-house CO_2 into useful chemicals helps establish a sustainable society but, unfortunately, requires effective catalysis.[1] During decades, tremendous efforts have been put on rationally modifying the catalyst surface in order to achieve advanced reaction performance. Nevertheless, the complexity of surface catalysis processes has made it a demanding task to build up a molecular-level understanding of heterogeneous catalysis.[2] Experimentally, various types of solid catalyst have been synthesized and applied into energy-related reactions. Although significant achievements have been made, it is, however, still difficult to accurately design excellent catalysts towards targeted reaction. Consequently, directions are desirably needed to provide useful predictions of a given material's catalysis activity towards a specific reaction.

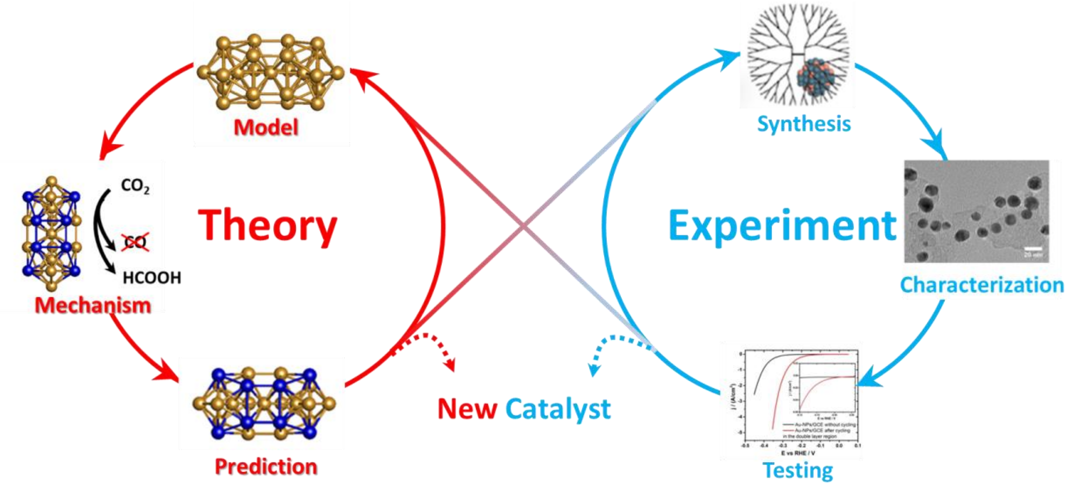

Figure 3.1 Smart design for new catalyst with combination of both theoretical and experimental approaches.

Nowadays, the great development of modern computational methods and their wide applications in scientific research have made it possible to offer sufficiently accurate estimations of key parameters necessary for the rational design of electrocatalysts, in particular the interaction energies of reaction intermediates with catalyst surfaces. As illustrated in Figure 3.1, simplified models can be simulated to represent the electro-catalysts or, in some cases, the most-abundant surfaces of the catalyst particles. Subsequently, different reaction pathways can be computed and the reaction mechanism, the most favored energy diagram for product evolution, can be estimated. Then, reliable predictions can be made. Inspired by the theoretically predicted models, oriented experiments can be logically performed through synthesis, characterization and testing. The combination of theoretical and experimental approaches has resulted in a better understanding of the atomic-scale properties that determine the macroscopic kinetics and the overall electro-catalytic activity. In this thesis, theoretical approach is performed to rationally predict new catalysts with enhanced catalytic activity for electro-chemical CO_2 reduction reactions.

3.2 Fundamentals of Theoretical Surface Catalysis

3.2.1 Catalyst Boosted Surface Reactions

Catalysis, coined by Baron in 1835, is a process in which a substance (catalyst) facilitates the rate of a chemical reaction without itself getting consumed during the reaction.[3] Catalysis can be classified into two types, heterogeneous and homogeneous, depending on whether the catalyst stays in the same phase as the reactants. Heterogeneous catalysis refers to those where the catalyst acts in different phase from the reactants while homogeneous catalysis are those where the catalyst and the reactants are in the same phase.

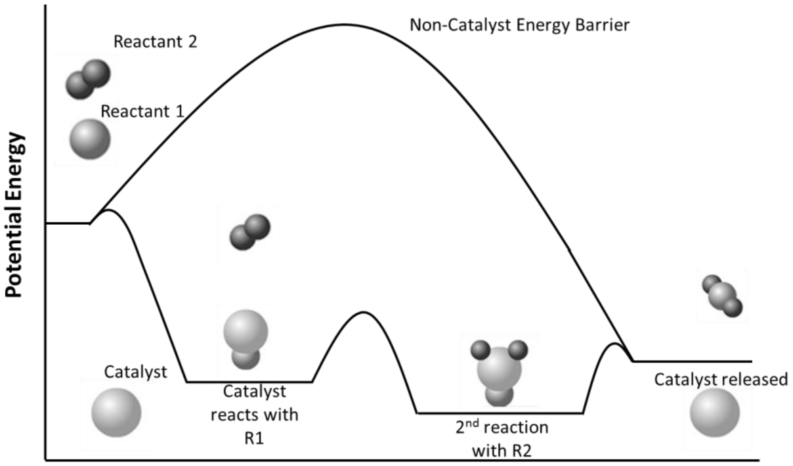

Figure 3.2 Reaction coordinates of non-catalyst approach and catalyst-boosted approach.

In electrochemical reactions, due to the ease of separating and recycling the catalyst, heterogeneous catalysis has been more popular than the homogeneous analogues.

Moreover, heterogeneous catalysts are typically more tolerant of extreme operating conditions, enabling them more advantageous in energy conversion reactions, where strong acidic or alkaline conditions are frequently applied.[4] Hence, it is of vital importance and concern for industrial society to understand the catalytic reactions in this class and improve the activity of the catalyst.

Mechanistically, the energy needed to activate a chemical reaction can be largely reduced by introducing a catalyst into the system. Usually, when a catalyst in solid state is used to speed up a chemical reaction, the overall process can be separated into a series of elementary steps, as illustrated in Figure 3.2. The role of the catalyst, in this process, is to provide active sites for the adsorption of the reactants, the breaking of the reactant bonds, the diffusion of the reaction intermediates, and the formation of reaction products, which end up being released from the catalyst surface.[4]

3.2.2 Adsorption on Catalyst Surface

Heterogeneously, as the catalysis processes take place at the interface, the interactions between the adsorbate species and the catalyst surface play key roles in the performance of the reaction. The adsorbate-catalyst interactions, however, can be in either physical or chemical form. These two kinds of interactions differ in various aspects, among which the operating force is the most crucial one that determines the interaction type.[5] For physisorption, the adsorbates are adhered to the adsorbent by weak van der Waals forces, making the process reversible when temperature is increased or pressure is decreased. In contrast, in chemisorption, the adsorbates are linked to the adsorbent by strong chemical bond, either covalent or ionic. Hence, chemisorption is an irreversible process and requires a high energy to activate.

In view of catalysis domain, it is the large numbers of active sites on the catalyst surface that accelerate the reaction rate. In some cases, the accelerated rate of reaction is simply because of an increased concentration of reactants on the catalyst surface, leading to a higher chance for them to crash and react. Hence, catalysis, in these cases, can result from physical adsorption of the reactants. However, in more cases, chemisorption is an essential step during catalysis, altering the adsorbed reactant to make it more receptive (changed geometric configuration) to chemical reaction. Therefore, unless otherwise stated, all the adsorption behaviors discussed in this thesis are chemisorption processes.

3.2.3 Sabatier Principle

Considering that the interactions between the reactants (or the related intermediates) and catalyst could be randomly different, it is necessary to find out the theory behind the apparently displayed adsorption affinity and define the optimal bond strength.

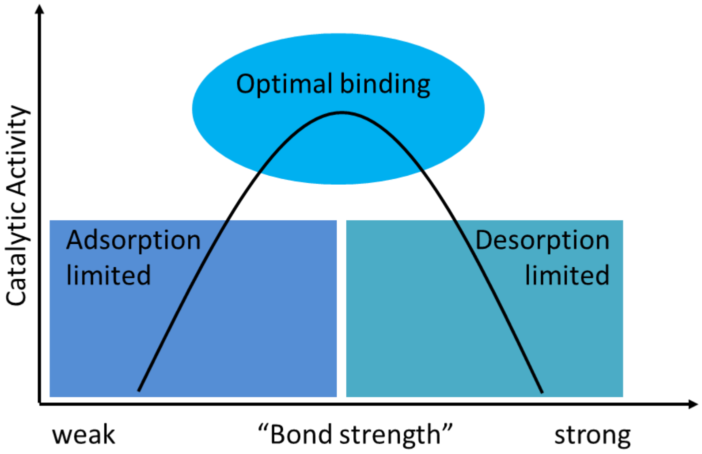

Figure 3.3 A schematic representation of the Sabatier principle.

Based on the current understanding of heterogeneous catalysis, a good catalytic surface should bind the reactants properly, neither too strongly nor too weakly.[6] In other words, if the interaction is too strong, the reaction intermediates or products will be difficult to get released from the catalyst surface, hence blocking the active sites of the catalyst. On the other hand, if the interaction is too weak, the reaction can hardly proceed since high activation energy is required. This concept was proposed by the French chemist Paul Sabatier in 1911, and has since become the main paradigm in heterogeneous catalysis. Based on this principle, if graphically plotting the reaction rate as a function of the catalyst-reactant interaction, the figure must past through a maximum, looking roughly like a volcano. Hence, plots in this type are called 'volcano plots'. Different types of interactions have been used to describe the properties of the catalysts, while the strength of chemisorption bond (binding energy) and the related free energy are usually chosen in electro-catalysis reactions.

3.2.4 The Chemisorption Bond and the *d*-band Center Theory

Considering that the interactions between the reactants (or the related intermediates) and catalyst could be randomly different, it is necessary to find out the theory behind the apparently displayed adsorption affinity and define the optimal bond strength.

The chemisorption bond between the adsorbate (or reaction intermediate) and the catalyst, however, can be complicated since it originates from the electronic interactions. To describe and predict the quantum mechanics of the reactants (atoms or molecules) interacting with a metal surface, the *d*-band center theory, proposed based on a simple one-electron model, has been established by Hammer and coworkers.[7]

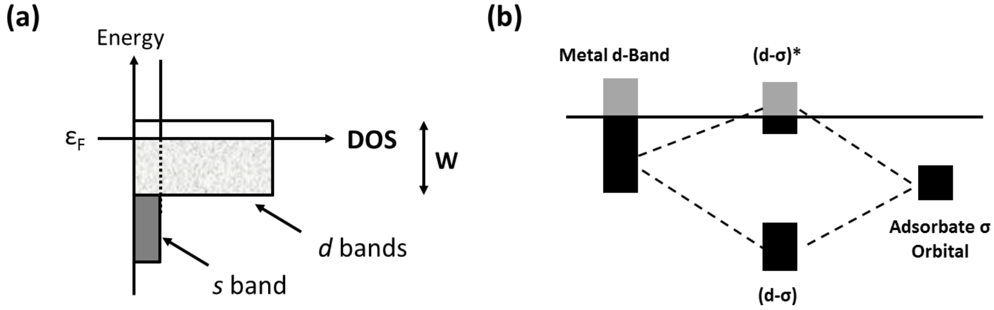

Figure 3.4 (a) Schematic illustration of the density of states of a transition metal, containing the broad *s* band the narrow *d* bands around the Fermi level, ε_F. (b). Bonding states between the adsorbate *σ* orbital and the metal *d*-band.

Electronically, the density of states for a transition metal consists of two parts, the broad *s* band and the narrow *d* band (see Figure 3.4(a)). Both parts contribute to the adsorbate-surface bond:

$$\Delta E = \Delta E_0 + \Delta E_d \tag{3.1}$$

where ΔE_0 is the bond energy contributed from the coupling between the adsorbate states and the *s* electrons of the transition metals, and ΔE_d is the contribution from the metal *d* band. For transition metals, since the *s*-bands are broad and quite similar, it is considered that ΔE_0 shows no sensitivity to different metals. Based on this reasonable assumption, it is the coupling between adsorbate balance states and the narrow metal *d*-states that determines the variation in binding energies (and hence the catalytic activities) for different chemisorption process.

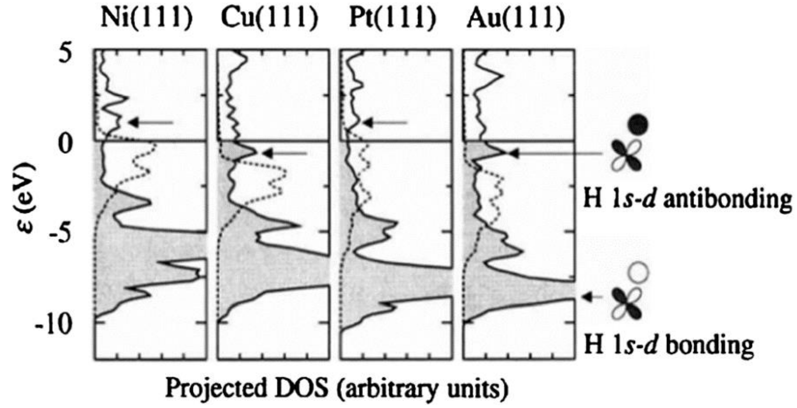

Figure 3.5 The projected density of states of atomic hydrogen chemisorbed on the (111) surface of Ni, Cu, Pt, and Au. The dashed lines show the PDOS of the four clean metal surfaces while the solid lines illustrate the PDOS after the chemisorption. Reproduced with permission from ref. 8 © 2009 Nature Publishing Group.

When the adsorbate valence states (σ orbitals) interact with the metal *d*-band, a bonding state and an antibonding state are generated, as illustrated in Figure 3.4(b). Unlike the gas-phase chemistry, where the strength of the bond is given by the number of electrons in the whole system, on a transition metal surface, the strength of the bond is determined by the filling of the antibonding states relative to the Fermi level. Since the antibonding states are always above the *d* states, the energy of the *d* states (the *d*-band center) relative to the Fermi level is a good as well as the first indicator of the bond strength: the higher the energy of the *d*-band center, the stronger the bond strength between the adsorbate and the catalyst.

Quantitative evidence for the d-band center theory is shown in Figure 3.5, where the atomic hydrogen chemisorption on the (111) surface of Ni, Cu, Pt, and Au is projected. From the projected density of states (PDOS) of the clean metal surfaces (the dashed lines), the d-band centers of Au(111) and Cu(111) stay quite far from the Fermi level, hence the antibonding states are filled and below the Fermi energy. This gives rise to repulsion interaction and leads to weak bond strength. The opposite is observed in the case of

Ni(111) and Pt(111). That is, if the d-band center is high and close to the Fermi level, the resulted antibonding states will be shifted above the Fermi level and remain empty, leading to strong bond strength. Therefore, performing the PDOS of *d* orbital and computing the *d*-band center can give general explanations of the achieved binding energies and roughly predict the surface reactivity for different adsorbates at specific sites.[8] Properly taking advantage of this strategy, the binding affinity of a given catalyst towards CO_2ER intermediates can be estimated.

3.2.5 Scaling Relations in Binding Energy

Things can be quite tedious when computing binding energies (or the related free energies) of various adsorbates on different catalysts. Although it is theoretically possible to obtain the electronic structures of complex systems and thus predict their catalytic activities, the repetitive computational works will result in low efficiency. Hence, it is important to develop approaches to rapidly screen the adsorption affinities for different adsorbed species on the catalyst surface.

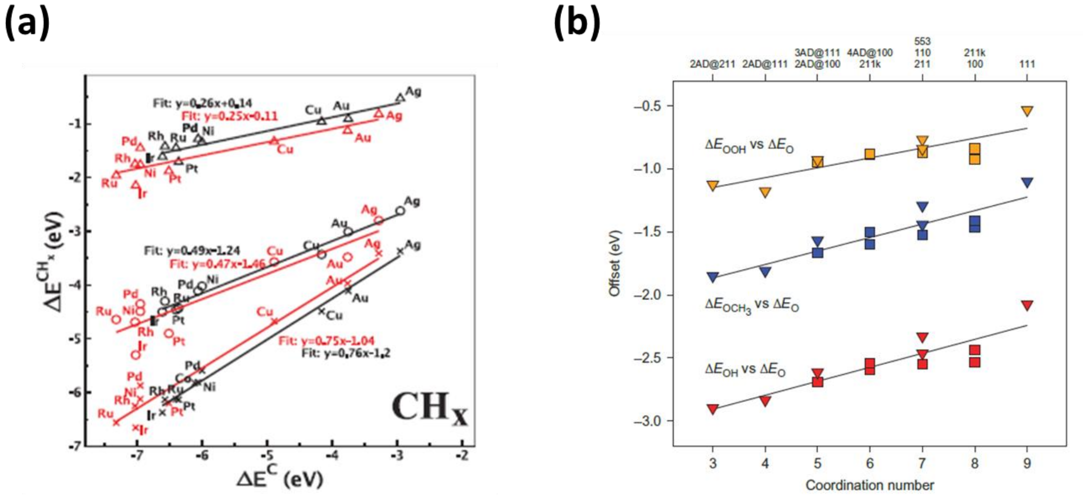

Figure 3.6 (a) Illustration of the scaling relations for adsorption energies of CH_x intermediates (crosses: $x = 1$; circles: $x = 2$; triangles: $x = 3$). The adsorption substrates are the most close-packed surfaces of the corresponding metals. (b). Illustration of the scaling relations for adsorption energies of *OH *vs.* *O (red), *OOH *vs.* *O (orange), and $*OCH_3$ *vs.* *O (blue). The types of adsorption sites are labeled at the top. The triangles represent hexagonal-symmetry sites,

and the squares represent sites with square or mixed hexagonal/square symmetry. Reproduced with permission from ref. 9 © 2007 American Physical Society.

The scaling relations, firstly discovered by Abild-Petersen and coworkers, define that the adsorption energies of hydrogen-containing molecules depend, in some cases, linearly on each other.[9] Quantitatively, this relation can be expressed as:

$$\Delta \mathrm{E}_2 = A_{1,2} \bullet \Delta E_1 + B_{1,2} \tag{3.2}$$

where ΔE_1 and ΔE_2 are the binding energies of species 1 and species 2 on a facet, respectively. The slope $A_{1,2}$ is the ratio of the number of bonds that species 1 lacks to reach its valence number and the number of bonds that species 2 lacks to reach its valence number. Examples of these ratios are shown in Figure 3.6: the scaling relation between *CH and *C has a slope of 3/4, while that between $*CH_2$ and *C has a slope of 1/2 (* represents the active sites on the surface, while * together with the binding species denotes an adsorbed state of the species). The offset $B_{1,2}$ is dependent on the binding species and so far there is no predictive power to estimate it.

Inspired by this finding, more recently, Federico *et al.* further discovered that besides the valence number, the coordination of the active sites also plays non-negligible role in forming the scaling relation.[10] The screened data of scaling relation (Figure 3.6(b)) displays obvious dependence on the coordination number of the surface sites, with changed number of the offset $B_{1,2}$. Therefore, the valence number of the adsorbate and the coordination number of the surface site concurrently determine the scaling relations.

The scaling relation was initially observed on pure metals and bimetallic surfaces[9], however, this phenomenon has been extended to nanoparticles[11] and various transition-metal compounds such as oxides[12], carbides[13], sulfides and nitrides[12], and metalloporphyrins and functionalized graphitic materials[14,15]. Based on this theory, computational processes of identifying new active electrocatalysts, in some cases, can be dramatically simplified.

3.2.6 Brønsted–Evans–Polanyi (BEP) Relation

From an energetical point of view, the low reaction rate is largely due to, in most cases, the high energy required for the activation. Introducing the catalyst into the system can dramatically decrease the activation energy; however, the activation energy cannot be completely eliminated. Thus, activation barriers still need to be computed for accurately predicting the catalytic activity of a given material. Unfortunately, so far the process to calculate the reaction barrier is quite resource-consuming since, mechanistically, the most reliable method requires thorough scanning of the whole potential energy surface. To resolve this problem, the Brønsted–Evans–Polanyi (BEP) principle has been extensively applied in theoretical catalysis in order to obtain a more simple and straightforward approach.[16-18]

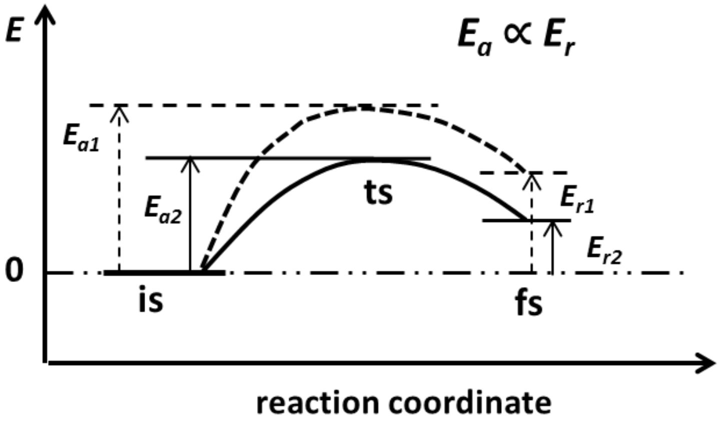

Figure 3.7 A schematic illustration of the Brønsted–Evans–Polanyi (BEP) principle on the positive correlation between activation energy and reaction energy. Is, ts, and fs represent initial state, transition state, and final state, respectively.

The main concept of BEP principle is that the difference in activation energy depends linearly on the reaction energy. This relationship can be expressed as:

$$E_a = E_r + \alpha \Delta H \tag{3.3}$$

where E_a is the activation energy of the reaction, E_r is the reaction energy between the initial state and the final state, ΔH is the reaction enthalpy, and α is the position of the transition state along the reaction coordinate ($0 \leq \alpha \leq 1$). Quantitatively, based on this relation, it is obvious that a higher final state in potential energy indicates a higher activation energy. Hence, for a specific reaction catalyzed by different catalysts, the state of each coupled intermediate can tell exactly the trend for the energetical reaction rate (the activation energy). Moreover, Bligaard and coworkers have investigated the implications of the BEP relation on the kinetics of surface-catalyzed chemical processes.[19] They found that the plotted turnover frequency verses the dissociative adsorption energy of the key reaction intermediate yields a volcano shape, which further supported the validity of taking advantage of BEP relation into computational catalysis. Therefore, of all the calculations in this dissertation, only the reaction energies are computed since they are precise enough to represent the reaction rate of the electro-chemical CO_2 reduction reaction and make useful predictions of decent catalysts.

3.3 Calculations and Models

3.3.1 Density Functional Theory (DFT)

Density functional theory (DFT), one of the most popular and versatile methods used in computational calculation, is commonly used in area of physics and chemistry to describe the electronic structure of many-body systems.[20] The agreement between the DFT calculation results and the experimental data has made DFT a very useful tool in computational chemistry. During the past 30 years, DFT has been the dominant method for the quantum mechanical simulation of periodic systems, which also includes the discipline of surface catalysis.

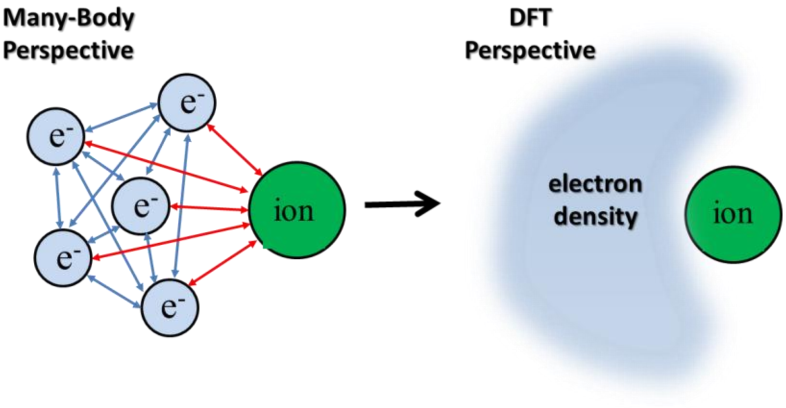

Figure 3.8 A schematic illustration of an interacting system described by many-body perspective and density functional theory (DFT) perspective.

Unlike the wavefunction based methods (the many-body perspective approach), DFT methods describe an interacting system via its electron density (Figure 3.8).[21] As it is known to all that, essentially, chemical reactions are the interactions between electrons. In principle, the quantum mechanical wavefunction contains all the information about a given system. For a case where only 10-100 electrons are involved, we can accurately obtain the wavefunction of the system by solving the Schrödinger equation, and hence the energy state. However, when the system contains N (N >> 100) electrons, it becomes, unfortunately, impossible to acquire the electronic information of the system due to the unaffordable computational cost. Alternatively, if we use the electron density to describe the electronic structure of a many-body system, which is the key concept of DFT methods, the computational cost issue caused by the structure size can be significantly solved as the electron density is a function of three coordinates regardless of the number of electrons.

Modern DFT begins in 1965 when Kohn and Sham demonstrated that the electron density of a complex interacting system could effectively, in a rigorous way, be obtained from simple one-electron theory.[22] Based on this K-S theory, the proposed equation (Kohn-Sham equation) for the total energy is expressed as a functional of spin-density in:

$$E[n_\uparrow, n_\downarrow] = T_S[n_\uparrow, n_\downarrow] + \int d_3 r n(r) v(r) + U[n] + E_{xc}[n_\uparrow, n_\downarrow] \qquad (3.4)$$

where $[n_\uparrow, n_\downarrow]$ is the total electronic density. The first term $T_S[n_\uparrow, n_\downarrow]$ is the non-interacting kinetic energy and is defined as

$$T_S[n_\uparrow, n_\downarrow] = \sum_\sigma \sum_i \theta_{\sigma i} \left\langle \psi_{\sigma i} \right| -1/2\nabla^2 \left| \psi_{\sigma i} \right\rangle \qquad (3.5)$$

The second term is the interaction of the electrons with the external potential $v(r)$. The third part is the Hartree electrostatic self-repulsion of the electron density, and is defined as

$$U[n] = 1/2 \int d^3 r \int d^3 r' \frac{n(r)n(r')}{|r - r'|} \qquad (3.6)$$

The last term is the exchange-correlation energy and is the only part that cannot be accurately obtained. This means, the exact ground-state energy and spin-densities of a many-electron interacting system can be exactly predicted only when the exchange-correlation energy is rationally approximated. In practice, two types of approximations, the local-spin density approximation (LDA) and the generalized gradient approximation (GGA), are extensively used.[23] According to the consistency between the KS computed trends and the experimentally observed ones, both approximations can provide reliable data to make useful predictions. However, based on a detailed study by Nørskov, the GGA methods offer more precise trends than LDA methods when dealing with surface bonding systems.[24] Therefore, the GGA approaches are employed in all the calculations of this work.

3.3.2 Simulation Model

For solid-liquid interface reactions, the surface of the catalyst plays the dominant role in deciding the catalytic activity since the active sites on the surface are responsible for the decrease of reaction barrier.

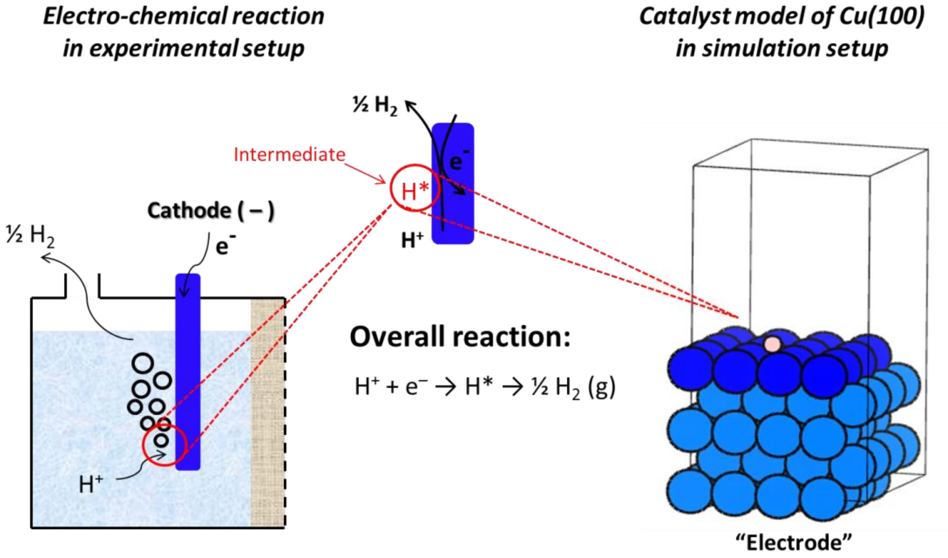

Figure 3.9 A schematic illustration of the connection between experimental situation and simulation model.

A simple simulation model of the catalyst surface and how it is correlated to the real situations are shown in Figure 3.9, where HER is used as an example. In the computational code, the unit cell in the black box is periodically repeated in three directions in order to establish the long solid surface. The upmost layer, which is highlighted in dark color, is the place where the reaction happens and the intermediates generate. The adsorption properties of the reaction intermediates, which are considered as the key factors determining the catalyst activity, are computed on the simulated catalysis surfaces. Under experimental conditions, the electrodes (serve as the reaction catalyst) are surrounded by aqueous environment; while in simulation, we use vacuum to represent this space. In most cases, this approximation does not affect the catalysis trend; however, in CO_2ER domain, some intermediates are sensitive to water and the solvation effect cannot be omitted.[25] For these cases, the quantitative influences of water solution on the binding affinities of these intermediates will be added to the total electronic energies by taking advantage of previous theoretical discoveries. More detailed explanation of solvation effect treatment is discussed later in this chapter.

3.4 Theoretical Descriptor for the Hydrogen Evolution Reaction (HER)

Although unwanted, the hydrogen evolution reaction (HER) is an inevitable reaction when CO_2 electro-reduction reaction is performed on liquid-solid interface. A good CO_2 conversion catalyst requires a relatively poor HER performance to avoid the low Faradaic efficiency for CO_2 reduction products. Hence, to predict good CO_2 reduction catalysts, their HER activities also need to be studied and computed.

3.4.1 Mechanism of HER

The mechanism of a very reaction is of vital importance to researchers as it reflects the reaction pathways which can be used as guidelines to design better catalyst for this reaction. Contributed to decades' effort, the mechanism of HER has been revealed and included in published textbooks for researchers' reference.[26]

Hydrogen evolution reaction (HER), which can be written as $H^{+}(aq)+e^{-}\rightarrow 1/2H_{2}(g)$, is a multi-step process within which proton gets one electron on the catalyst surface and forms a chemisorbed hydrogen atom and then molecular hydrogen gas. It is generally accepted that there are three possible reaction steps in this reaction (Figure 3.10).

The first step of HER, $H^{+}(aq)+e^{-} \rightarrow H*$ (* denotes an adsorption site on catalyst surface), which remains no controversial, is presented in Figure 3.10 (the blue arrow). In this step, a proton combines with an electron and adsorbs on the catalyst’ s surface to form a chemisorbed H atom, which is the only intermediate in HER. However, the subsequent H_2 gas formation may happen via two possible reaction pathways, Tafel pathway (red arrows in Figure 3.10) and Heyrovsky pathway (purple arrows in Figure 3.10). In Tafel pathway, which is confirmed for HER on Pt(111) surface[27], two chemisorbed hydrogen atoms combine together on the electrode surface and get released as H_2 gas. In Heyrovsky pathway, the transfer of a second electron to the adsorbed hydrogen atom is coupled with the transfer of another proton from the solution to evolve H_2 gas.

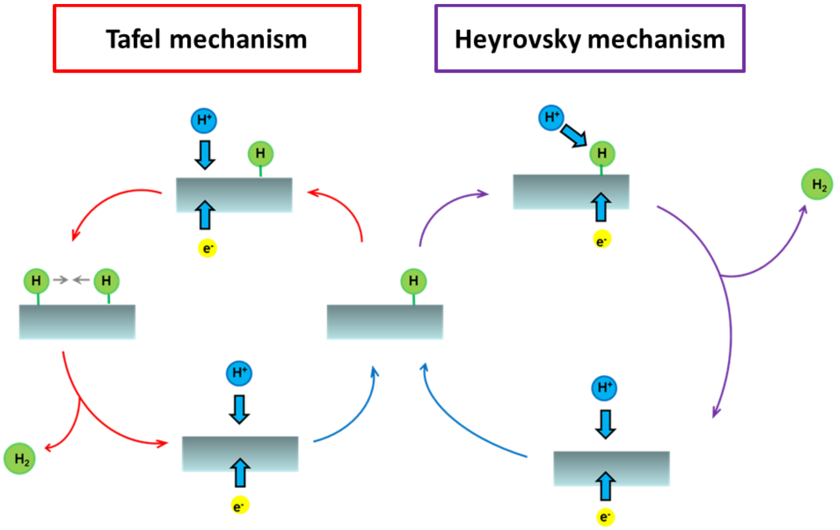

Figure 3.10 Two possible reaction pathways for electro-chemical hydrogen evolution reaction (HER).

Although studies on different materials suggest the existence of two different pathways for the second step of HER, both mechanisms are based on the same pre-step, the formation of a chemisorbed H atom. Hence, manipulation of materials’ ability of forming a chemisorbed hydrogen atom can provide guidance in designing better catalyst towards HER.

3.4.2 Theoretical Descriptor

Decades' efforts on theoretical and experimental design of HER catalysts have revealed the secrets of materials' HER catalysis activity and a complete and comprehensive theoretical system has been built up since the beginning of 21 century, through which researchers can match the experimental observation of a catalyst's HER catalysis performance and its theoretical descriptor.

As mentioned above, although different catalyst displays different pathway for the second step of HER, both pathways show that at least one H atom in the final gaseous hydrogen molecule is from the adsorbed H, which is the product from the first step of HER. Proposed by Jens K. Nørskov, the adsorption free energy of this H atom (ΔG_{H*}) is considered as the theoretical descriptor for HER.[28]

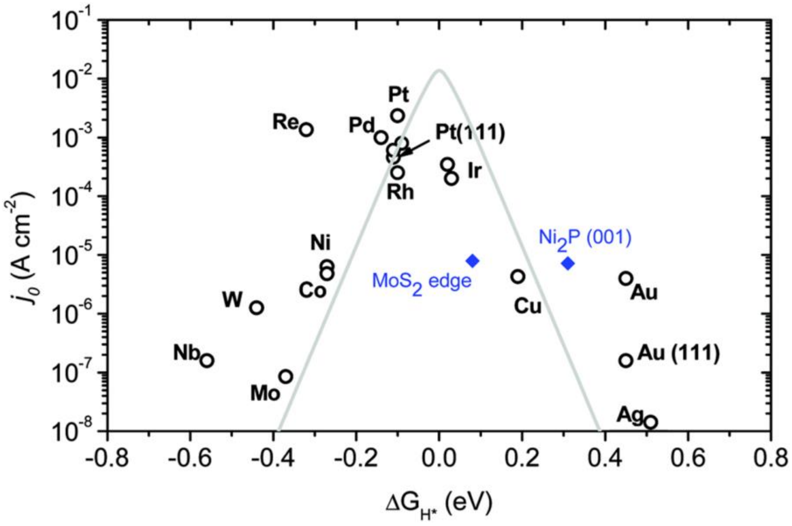

Figure 3.11 The generated volcano plot (the experimentally measured exchange current density, j_0, as a function of the theoretical H chemisorption free energy, ΔG_{H*}) for HER. Original data are taken from ref. 28 © 2005 The Electrochemical Society, Inc.

In this theory, the chemisorbed H atom is the only intermediate and ΔG_{H*} is calculated by the following equation:

$$\Delta G_{H*} = \Delta E_H + \Delta E_{ZPE} - T\Delta S_H \tag{3.7}$$

where ΔE_H is the electronic binding energy, ΔE_{ZPE} is the difference in zero point energy of H between the adsorbed phase and the gas phase and ΔS is the corresponding entropy difference. The electronic binding energy is defined as:

$$\Delta E_H = E(slab + H) - E(slab) - 1/2E(H_2) \tag{3.8}$$

where $E(slab + H)$, $E(slab)$, and $E(H_2)$ are the total electronic energies of the bonding system, the clean catalyst slab, and the gaseous hydrogen molecule, respectively. A volcano-shape figure is generated by plotting the experimentally used descriptor of the reaction rate, the exchange current density, as a function of this ΔG_{H^*}. Based on the Sabatier Principle, a good catalyst should have mediate interactions with the reaction intermediate, neither too strong nor too weak. Therefore, for the right part of the volcano ($\Delta G_{H^*} \gg 0$), where hydrogen binds too weakly, the lack of adsorption sites is the reason for the poor catalysis performance. While for the left part ($\Delta G_{H^*} \ll 0$), the strongly adsorbed hydrogen can hardly get released from the surface, leading to low reaction rate. Hence, a catalyst with a free energy around zero is considered as excellent, which is the case for Pt in the volcano plot.

3.5 Theoretical Descriptor of CO_2ER Reactions

3.5.1 Mechanism of CO_2ER

The electro-catalytic reduction of carbon dioxide is a complicated process as the multiple proton-electron transfer can lead to various products (P) and water:

$$CO_2 + n(H^+ + e^-) \leftrightarrow P + mH_2O \tag{3.9}$$

The most common products "P" in aqueous media include carbon monoxide (CO), formaldehyde (HCHO), formic acid (HCOOH), methanol (CH_3OH), and methane (CH_4). The standard electrode potentials for CO_2 reduction to various products in aqueous solution are summarized in Chapter 2. Although the potentials will differ greatly in real situations, it is still useful for estimating the tendency of each product.

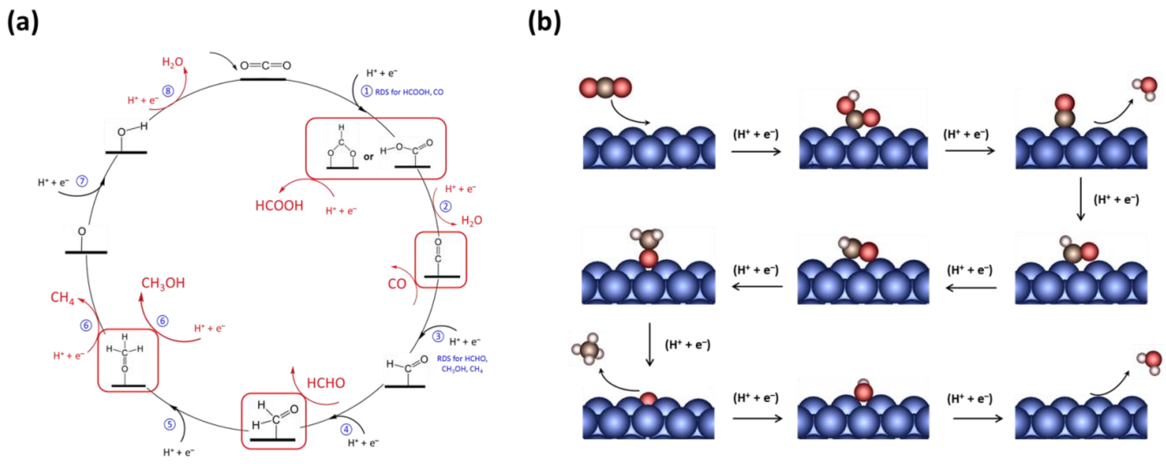

Figure 3-12 (a) The most economic reaction pathway for mono-carbides formation during CO_2 reduction processes. For each arrow, it represents an elementary step of proton and electron transfer. The steps for the generation of products have been highlighted by red cubes. (b) Side view of each elementary step on stepped Cu(211). The atoms in red, brown, white, and blue represent O, C, H, and Cu, respectively.

For catalyzed CO_2ER reactions, the multiple proton-electron transfer steps may generate numerous possible intermediates. However, not all intermediates are thermally stable and some of them can barely appear since extremely high energies are required. Thanks to decades' theoretical efforts, the most economic reaction pathways for the main products have been discovered and are shown in Figure 3.12.[29]

Based on the pathways in Figure 3.12 (a), the formation of various products originates from whether the transferred proton-electron pair is coupled to C atom or O atom. For example, at step 6, if the neutral H (proton-electron pair) binds to C atom, then C–O bond will break and CH_4 will be generated; however, if it interacts with the O atom, CH_3OH will be formed and directly get released from the catalyst surface. The formation of CO and HCHO, however, is another case where no H is transferred to the final step and the previously formed unstable intermediates can straightforwardly desorb from the catalyst to yield the final products. The generation of HCOOH may go through two possible approaches, via the intermediates of *COOH and *OCHO, respectively. The rate determining step (RDS), which determines the activity of the catalyst, for each product is also illustrated in the Figure 3.12. It should be mentioned that RDS may occasionally differ on the used catalyst; but for all the catalysts, lowering the energy barrier of RDS is always the motivated goal. To help establish a more deep original understanding of the adsorption models, side views of reaction intermediates involved in CO_2ER to CH_4 on stepped Cu(211) are summarized in Figure 3.12 (b). Based on this type of models, by computing the free energy state of the reaction intermediates, the evolution of CO_2 reduction process on a given catalyst can be quantitatively analyzed.

3.5.2 The Computational Hydrogen Electrode (CHE) Model

Originally designed to explain the overpotential of oxygen reduction reaction (ORR), the computational hydrogen electrode (CHE) model has been modified and proved to be effective in describing the multiple proton-electron transfer process during CO_2 electro-reduction.[25,30] In this technique, the reversible hydrogen electrode (RHE) is chosen as the reference and the reaction

$$H^+ + e^- \leftrightarrow 1/2H_2(g) \tag{3.10}$$

is assumed to be in equilibrium at zero voltage, all temperatures, all values of PH, and with H_2 at 101325 Pa pressure. Hence, thermodynamically, the chemical potential of a proton-electron pair can be considered as being equal to half of the chemical potential of molecular hydrogen in gas-phase at the potential of 0V *vs* RHE,

$$\mu[H^+] + \mu[e^-] = 0.5\mu[H_2(g)] \tag{3.11}$$

Taking advantage of the standard relation between the chemical and electrical potential, $\Delta G = -eU$, where e is the (positive) charge of an electron, the chemical potential of a proton-electron pair as a function of the applied potential can be expressed as

$$\mu[H^+] + \mu[e^-] = 0.5\mu[H_2(g)] - eU \tag{3.12}$$

By definition, the limiting potentials (U_L) of an elementary hydrogenation step is the potential at which the reaction becomes downhill, or exergonic in free energy. That is, taken the elementary step of CO hydrogenation (Equation. 3.13) as an example,

$$*CO + H^+ + e^- \rightarrow *CHO \tag{3.13}$$

where the asterisk, *, denotes that the species is an adsorbed one. The free energy change of this hydrogenation step will be

$$\begin{aligned}\Delta G_{elem} &= \mu[*CHO]-\mu[*CO]-\mu[H^{+}+e^{-}]\\ &= \mu[*CHO]-\mu[*CO]-0.5\mu[H_2(g)]+eU \end{aligned} \tag{3.14}$$

By the earlier definition, $\Delta G_{elem} = 0$ at $U = U_L$, so

$$U_L = -\frac{\mu[*CHO]-\mu[*CO]-0.5\mu[H_2(g)]}{e} = \frac{-\Delta G^{0V}_{elem}}{e} \tag{3.15}$$

Thus, the CHE model allows the potential (U) to be explicitly involved within the free energy change of each elementary step. However, two approximations are, at the same time, employed inside this system. The first one is the neglect of the barriers for proton transfer to adsorbates from the solution. Previous study has shown that the barrier for proton transfer is from 0.02 eV to 0.25 eV for *OH hydrogenation in aqueous solution.[31] Since 0.25 eV is quite surmountable at room temperature, the barrier for proton transfer is thus neglected in this CHE model. The other one is the exclusion of reaction barriers and coverage effects. More exact predictions surely require the inclusion of both factors; however, for the first indication of when different pathways in the electro-chemical reduction of CO_2 occur, it is reasonable to accept these approximations since it helps save a lot of computational resources.

3.5.3 Free Energy for CO_2ER Intermediates

The Gibbs free energy system in CO_2ER, however, is slightly different from the one defined in HER.[25] More rigorously, the free energy of each state is defined as (taken *CHO state as an example)

$$G(*CHO) = E_{elec} + E_{sol} + ZPE_{*CHO} + \int C_P dT - TS_{*CHO} \tag{3.16}$$

where E_{elec}, E_{sol}, ZPE, $\int C_P dT$, and TS are the electronic energy, the correction for solvation effect, the zero point energy, the enthalpy correction, and the entropy effect, respectively. The solvation effect refers to the slight change on the binding affinities of some adsorbed species due to the presence of aqueous environment. Previous study found that hydroxyl species (*OH) exposed to water is stabilized by approximately 0.5 eV[32,33], and hydroxyl that is indirectly bound to the surface through other atoms, such as *R-OH, may be stabilized by ~ 0.25 eV[31] (as shown for *COOH). Moreover, the solvent stabilization of adsorbed CO was also investigated and found to be 0.1 eV on Cu (111) surface.[25] These values are considered as independent on the catalyst type and hence can be applied to all catalyst models. The values of ZPE, $\int C_P dT$, and –TS of each adsorbate and gas molecule can be found in Table S1 and Table S2 in the appendix.

Electronic binding energy of each adsorbate in CO_2ER is defined as

$$\mathrm{E}_{CxHyOz} = E_{slab+CxHyOz} - E_{slab} - xE_C - yE_H - zE_O \tag{3.17}$$

where $E_{slab+CxHyOz}$, E_{slab}, E_C, E_H, and E_O are the total electronic energy of the bonding system, the clean slab, and the energies of C, H, and O atoms, respectively. The energy of C atom is referenced to graphene, while the energies of H and O atoms are referenced to gaseous H_2 and the difference between water and hydrogen molecule (H_2O – H_2), respectively. For stable adsorbates (CO and CH_2O), binding energies are also computed by referring to the energies of the stably existed gaseous state. Moreover, studies have found that theoretically calculated enthalpies of gas-phase molecules will differ greatly from the experimentally observed values when the molecules have a –OCO– backbone.[25,34] Hence, to correct this inconsistency and make more reliable predictions, a +0.45 eV is added to the total energies of CO_2 and HCOOH.

References

1 Lim, R. J. *et al.* A review on the electrochemical reduction of CO_2 in fuel cells, metal electrodes and molecular catalysts. *Catalysis Today* **233**, 169-180 (2014).

2 Calle-Vallejo, F., Koper, M. T. M. & Bandarenka, A. S. Tailoring the catalytic activity of electrodes with monolayer amounts of foreign metals. *Chemical Society Reviews* **42**, 5210-5230 (2013).

3 Bond, G. C. *Heterogeneous catalysis*. (Oxford University Press,New York, NY, 1987).

4 Mizuno, N. & Misono, M. Heterogeneous Catalysis. *Chemical Reviews* **98**, 199-218 (1998).

5 Mehlhorn, M. *et al.* Physisorption versus chemisorption of oxygen molecules on Ag(100). *The Journal of Chemical Physics* **144**, 134706 (2016).

6 Medford, A. J. *et al.* From the Sabatier principle to a predictive theory of transition-metal heterogeneous catalysis. *Journal of Catalysis* **328**, 36-42 (2015).

7 Hammer, B. & Nørskov, J. K. Theoretical surface science and catalysis—calculations and concepts. *Advances in Catalysis* **45**, 71-129 (2000).

8 Norskov, J. K., Bligaard, T., Rossmeisl, J. & Christensen, C. H. Towards the computational design of solid catalysts. *Nature Chemistry* **1**, 37-46 (2009).

9 Abild-Pedersen, F. *et al.* Scaling Properties of Adsorption Energies for Hydrogen-Containing Molecules on Transition-Metal Surfaces. *Physical Review Letters* **99**, 016105 (2007).

10 Calle-Vallejo, F., Loffreda, D., KoperMarc, T. M. & Sautet, P. Introducing structural sensitivity into adsorption–energy scaling relations by means of coordination numbers. *Nature Chemistry* **7**, 403-410 (2015).

11 Fu, Q., Cao, X. & Luo, Y. Identification of the Scaling Relations for Binary Noble-Metal Nanoparticles. *The Journal of Physical Chemistry C* **117**, 2849-2854 (2013).

12 Fernández, E. M. *et al.* Scaling Relationships for Adsorption Energies on Transition Metal Oxide, Sulfide, and Nitride Surfaces. *Angewandte Chemie* **120**, 4761-4764 (2008).

13 Vojvodic, A., Hellman, A., Ruberto, C. & Lundqvist, B. I. From Electronic Structure to Catalytic Activity: A Single Descriptor for Adsorption and Reactivity on Transition-Metal Carbides. *Physical Review Letters* **103**, 146103 (2009).

14 Calle-Vallejo, F., Martínez, J. I., García-Lastra, J. M., Abad, E. & Koper, M. T. M. Oxygen reduction and evolution at single-metal active sites: Comparison between functionalized graphitic materials and protoporphyrins. *Surface Science* **607**, 47-53 (2013).

15 Calle-Vallejo, F., Martinez, J. I. & Rossmeisl, J. Density functional studies of functionalized graphitic materials with late transition metals for oxygen reduction reactions. *Physical Chemistry Chemical Physics* **13**, 15639-15643 (2011).

16 Evans, M. G. & Warhurst, E. The activation energy of diene association reactions. *Transactions of the Faraday Society* **34**, 614-624 (1938).

17 Bell, R. P. The Theory of Reactions Involving Proton Transfers. *Proceedings of the Royal Society of London. Series A, Mathematical and Physical Sciences* **154**, 414-429 (1936).

18 Brønsted, J. & Pedersen, K. The catalytic decomposition of nitramide and its physico-chemical applications. *Z. Phys. Chem. A* **108**, 185-235 (1924).

19 Bligaard, T. *et al.* The Brønsted–Evans–Polanyi relation and the volcano curve in heterogeneous catalysis. *Journal of Catalysis* **224**, 206-217 (2004).

20 Gross, E. K. & Dreizler, R. M. *Density functional theory*. Vol. 337 (Springer Science & Business Media, 2013).

21 Parr, R. G. in *Horizons of Quantum Chemistry* 5-15 (Springer, 1980).

22 Kohn, W. & Sham, L. J. Self-consistent equations including exchange and correlation effects. *Physical Review* **140**, A1133 (1965).

23 Ziesche, P., Kurth, S. & Perdew, J. P. Density functionals from LDA to GGA. *Computational Materials Science* **11**, 122-127 (1998).

24 Hammer, B., Hansen, L. B. & Nørskov, J. K. Improved adsorption energetics within density-functional theory using revised Perdew-Burke-Ernzerhof functionals. *Physical Review B* **59**, 7413 (1999).

25 Peterson, A. A., Abild-Pedersen, F., Studt, F., Rossmeisl, J. & Nørskov, J. K. How copper catalyzes the electroreduction of carbon dioxide into hydrocarbon fuels. *Energy & Environmental Science* **3**, 1311-1315 (2010).

26 Lasia, A. Hydrogen evolution reaction. *Handbook of fuel cells* (2010).

27 Skúlason, E. *et al.* Density functional theory calculations for the hydrogen evolution reaction in an electrochemical double layer on the Pt (111) electrode. *Physical Chemistry Chemical Physics* **9**, 3241-3250 (2007).

28 Nørskov, J. K. *et al.* Trends in the exchange current for hydrogen evolution. *Journal of The Electrochemical Society* **152**, J23-J26 (2005).

29 Kortlever, R., Shen, J., Schouten, K. J. P., Calle-Vallejo, F. & Koper, M. T. Catalysts and reaction pathways for the electrochemical reduction of carbon dioxide. *The journal of Physical Chemistry Letters* **6**, 4073-4082 (2015).

30 Nørskov, J. K. *et al.* Origin of the overpotential for oxygen reduction at a fuel-cell cathode. *The Journal of Physical Chemistry B* **108**, 17886-17892 (2004).

31 Tripković, V., Skúlason, E., Siahrostami, S., Nørskov, J. K. & Rossmeisl, J. The oxygen reduction reaction mechanism on Pt (111) from density functional theory calculations. *Electrochimica Acta* **55**, 7975-7981 (2010).

32 Wieckowski, A. *Fuel cell catalysis: a surface science approach*. Vol. 1 (John Wiley & Sons, 2009).

33 Karlberg, G. & Wahnström, G. Density-functional based modeling of the intermediate in the water production reaction on Pt (111). *Physical review letters* **92**, 136103 (2004).

34 Blaylock, D. W., Ogura, T., Green, W. H. & Beran, G. J. Computational investigation of thermochemistry and kinetics of steam methane reforming on Ni (111) under realistic conditions. *The Journal of Physical Chemistry C* **113**, 4898-4908 (2009).

Chapter 4

Low-coordinated Cu Atoms in Electrochemical CO_2 Reduction Reactions

In this chapter, atomic-scale investigations have been computationally performed to reveal the role of low-coordinated sites on Cu electrode in catalyzing CO_2 electro-reduction reactions (CO_2ER). Four types of low-coordinated Cu sites – the planar (100) sites, the edged (211) sites, the cornered (532) sites, and the defective vacant-(111) sites, were simulated. Compared to the reaction states on the full-coordinated (111) sites, significantly lowered energy states have been observed on all these low-coordinated sites, suggesting the superior catalytic activity of the low-coordinated sites. Additionally, in the protonation step of $*OCH_3$ species, the formation of methane was found to be more thermally advantageous than the formation of methanol on low-coordinated sites, implying the selectivity for methane in hydrocarbon generation. Performances of the competing reaction, the hydrogen evolution reaction (HER), have also been computed on the simulated sites. Similar to CO_2ER, HER is also boosted on the low-coordinated sites, which indicates a high operation potential to take full advantage of low-coordinated sites for catalyzing CO_2ER. Finally, the d-orbital structures of these sites have been computed and the trend in d-band center confirms the validity of the free energy states and the accordingly drawn conclusions.

4.1 Introduction

Structural modifications have been extensively investigated as effective strategies to enhance the catalytic performance of metal nanoparticles. In CO_2 electro-reduction (CO_2ER) domain, various modification methods have been applied to metal particles in order to create structures with advanced catalytic activity. Among them, high-index surfaces[1,2], small-sized particles[3-5], curved morphologies[6,7], and porous structures[8] are frequently employed. Intrinsically, all these methods can effectively generate large numbers of low-coordinated atoms. Hence, it is proposed that low-coordinated atoms can catalyze the CO_2 reduction reactions more efficiently than the normally synthesized full-coordinated ones (Figure 4.1).

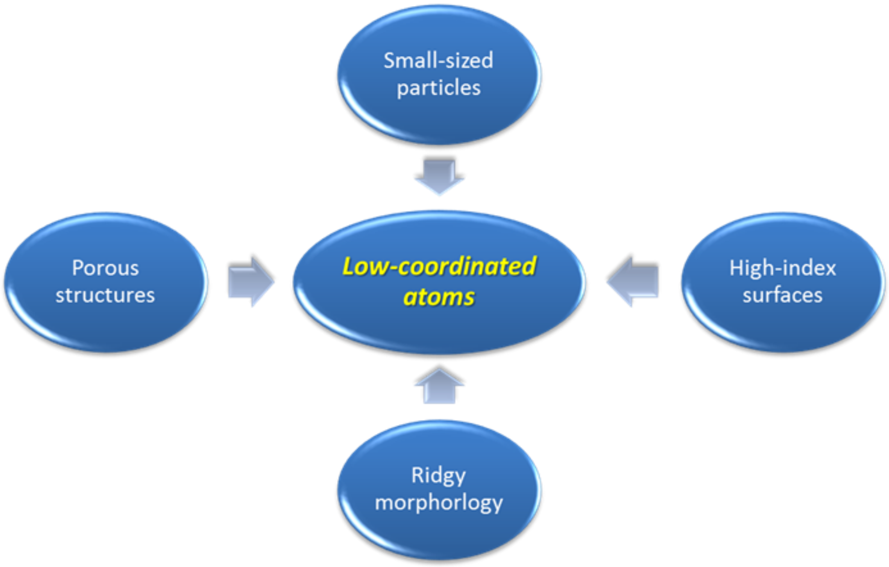

Figure 4.1 Hypothesis of the intrinsic reason for the catalytic performance on the currently employed structural modification approaches.

In this chapter, a systematical study on various kinds of low-coordinated Cu atoms and their catalytic properties for CO_2ER has been performed. In order to verify the proposed hypothesis, the full-coordinated atoms were represented by the atoms on (111) surface, while the low coordinated atoms were investigated on (100), (211) and (532) surfaces. Moreover, since vacancy defective site decreases the coordination number, a (111) surface with vacancy was also included for the study of low-coordinated atoms. For the purpose to have a comprehensive study on all the possible products from CO_2 reduction reaction, Cu was chosen as the catalyst electrode. Then theoretical calculations for the free energy of CO_2 reduction reaction into various kinds of products, including HCOOH, CO, CH_3OH, CH_4, and H_2, were performed and analyzed on the five above mentioned surfaces of Cu.

4.2 Computational Details

4.2.1 Calculation Models

A typical metal nanoparticle is composed of many facets (see Figure 4.2). Geometrically, three types of atoms can be identified based on their different local environments: full-coordinated facet atom, low-coordinated edge atom, and low-coordinated corner atom. Theoretically, all the surface areas can serve as active sites to catalyze CO_2ER in aqueous solutions. However, the diverse local environments can significantly alter the *d*-band structures of the surface metal atom, which is the key factor in determining the strength of surface-intermediate interaction. Hence, reaction rate may change greatly on these three types of atoms.

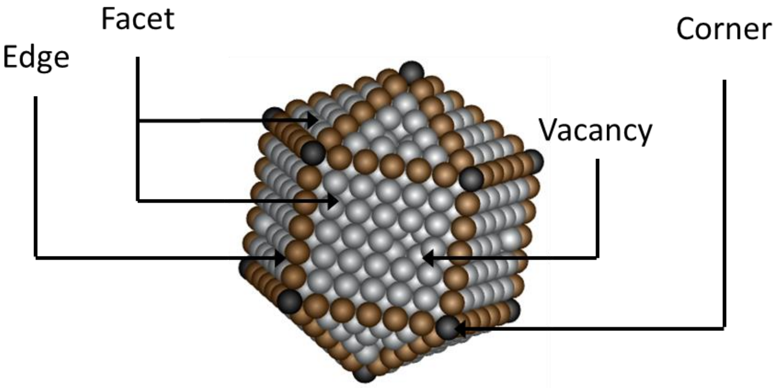

Figure 4.2 Illustration of the possible atomic sites on a metal nanoparticle.

Experimentally, metal nanoparticles are usually between 1 and 100 nanometers in size. Although particles in this range are still possible to be simulated, thousands of atoms are contained and extremely high computational resources are required for the calculation. Therefore, computationally, the (111) and (100) surfaces, the (211) surface, and the (532) surface are used to model the facet atoms, the edge atoms, and the corner atoms, respectively. Previous studies have revealed the validity of the obtained results based on these kinds of models.[9] However, although both (111) and (100) orientations are plain on the topmost surface, the coordination number of (111) surface atom is higher than that of the (100), comparatively making the (100) surface atom low-coordinated. In fact, the (111) surface is the most abundantly exposed one in experimental situations and the atoms on (111) surface has the highest coordination number among all the crystal surfaces. On the other hand, defective sites are inevitable under experimental conditions (Figure 4.2) and surface vacancies which make the surface atoms around low-coordinated. So the role of these vacancy sites on catalytic behaviors should also be taken into account and a (111) surface with vacancy, which is referred to as vac-(111) surface in the rest of this chapter, has been simulated to study the catalytic behavior of the low-coordinated atoms around the vacancy. In summary, the (111) surface represents the full-coordinated sites, while the other four kinds of atoms in (100), (211), (532), and vac-(111) surfaces stands for the low-coordinated atoms.

In order to achieve a thorough study of the low-coordinated sites, theoretical calculations have been performed on Cu electrodes, which is the only metal displaying the potential to catalyze CO_2 into various kinds of products, including CO, HCOOH, HCHO, CH_4, and CH_3OH. The calculated lattice constant of Cu is 3.68 Å, consistent with the experimentally measured value (3.62 Å) in papers.[10] For all the slab models, a four-layer model with 3 × 3 supercell was used in all situations. The periodic boundary condition has been employed to establish the long solid surface. To avoid the vertical interaction between the periodic images in z-direction, a 15 Å vacuum was added in call cases. During the structure optimization processes, the top two layers of the slabs and the adsorbates were allowed to relax until the most stable configurations were reached, while the bottom layers were kept fixed in their bulk positions.

4.2.2 Theoretical Methods

All the density functional theory (DFT) calculations were performed with the Vienna Ab-initio Simulation Package[11] (VASP). The projected augmented wave[12] (PAW) method was used to describe the ion-electron interactions. In order to achieve reliable results of catalyst-intermediate interactions, the revised Perdew-Burke-Ernzerhof[13] (RPBE) functional, which has proved to provide binding energies results close to experimental values, was chosen to describe the exchange and correlation effects. A cutoff energy of 500 eV was set for the expansion of the plane-wave basis set. All the structures were fully optimized until the residual forces on each atom were less than 0.05 eV/ Å without any constraints. Reciprocally proportional to the surface parameters, a Monkhorst-Pack[14] grid of 3 × 3 × 1 was used to carry out all the surface calculations. The computational hydrogen electrode[15] (CHE) model was used to calculate the free energies of each intermediate. More detailed procedures of this model have been explained in Chapter 3.

To characterize the stability of the vacant (111) surface, the surface energy (γ) and vacancy formation energy (E_{vac}) have been computed. The surface energy is defined as the energy required to form a surface from the bulk lattice, which is expressed as

$$\gamma = \frac{E_{slab} - nE_{bulk}}{A} \tag{4.1}$$

where E_{slab}, n, E_{bulk}, and A are the total electronic energy of the slab, the number of atoms in the slab, the electronic energy of a primitive cell containing one Cu atom, and the surface area of one side of the slab, respectively. Based on this definition, a smaller γ value indicates a more stable surface. The vacancy formation energy is defined as

$$E_{vac} = (E_{slab-vac} + E_{bulk}) - E_{slab-per} \tag{4.2}$$

where $E_{slab\text{-}vac}$, E_{bulk}, and $E_{slab\text{-}per}$ are the electronic energies of the vacant surface, the primitive cell containing one Cu atom, and the perfect surface, respectively. Under this definition, a small value of E_{vac} implies an easier vacancy formation situation.

4.3 Results & Discussions

4.3.1 Surface Properties

The perfect plain surfaces, (100) and (111), were firstly created (Figure 4.3). The (100) surface is a square-like lattice obtained by cleaving the fcc bulk with a Cu-Cu distance of 2.60 Å, while the (111) surface has a shape of hexagonal close-packed surface with the same Cu-Cu bond length as the (100) surface.

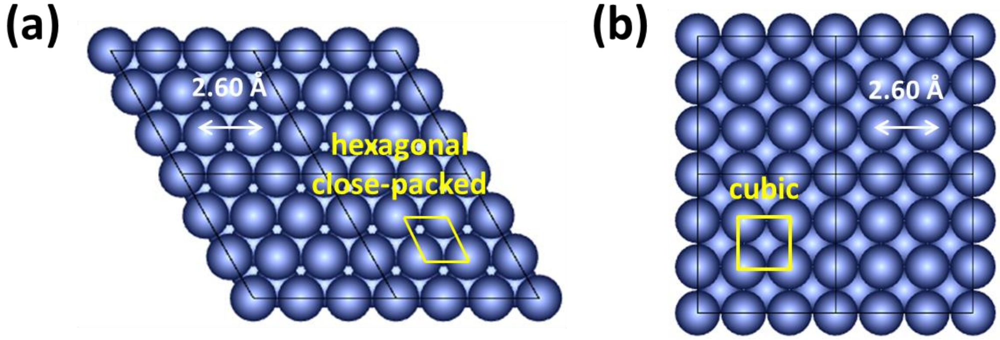

Figure 4.3 Top view of the two planar surfaces: (a) the full-coordinated (111) surface; (b) the low-coordinated (100) surface.

Top view of the other three simulated surfaces is illustrated in Figure 4.4. The (211) is a stepped surface with one line of atoms serving as the active sites for catalysis reactions (the highlighted dark blue atoms). The Cu-Cu bond length in (211) surface is also 2.60 Å, since, geometrically, (211) surface is a slant arrangement of the (111) plane. In the (532) surface, a single corner atom is located such that the bond length to the two neighbor atoms are 2.56 Å and 2.57 Å, respectively. For the vacant (111) surface, which is established to simulate the low-coordinated sites induced by the lattice vacancy defects, a larger Cu-Cu distance, 2.62 Å, is found than that in the perfect (111) surface in vacant (111) surface, this is due to the strain effect caused by the surface vacancies.

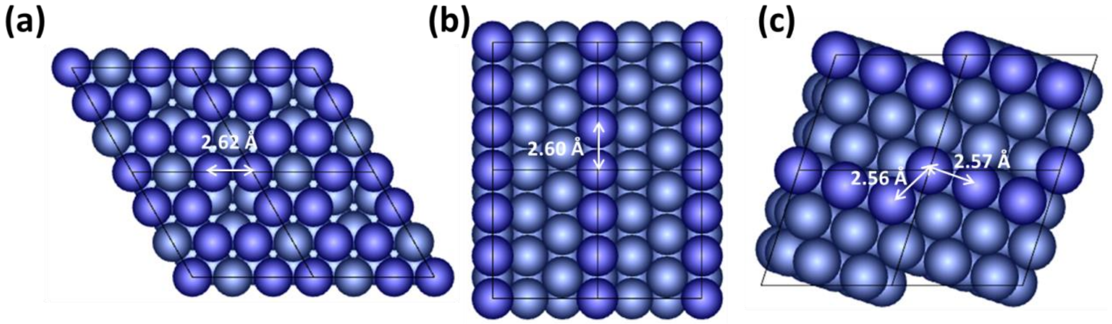

Figure 4.4 Top view of nonplanar surfaces: (a) vac-(111) surface; (b) (211) surface; (c) (532) surface. The low-coordinated atoms are highlighted in dark colour.

Table 4.1 Coordination number of the active sites on the simulated surfaces.

Surface	(111)	vac-(111)	(100)	(211)	(532)
Coordination number	9	8	8	6	5

The coordination number of the atoms in the above five simulated surfaces is presented in Table 4.1. The coordination number of the full-coordinated surface (111) site is 9, which is the highest value that an atom in fcc metal particles can have. While, the active atoms in the vac-(111) surface and (100) surface have 8 atoms to coordinate. On the edged (211) and cornered (532) surfaces, the coordination numbers of active atoms are even lower, with a value of 6 and 5, respectively.

In order to investigate the stability of the vacant surface, the surface energy and vacancy formation energy of the clean and vacant (111) surfaces have been calculated and summarized in Table 4.2. Thermodynamically, the vacant surface is less stable than the perfect surface, with a higher surface energy. This trend is consistent with the results from previous reports (Table 4.2), where surface vacancies on different Cu planes have been systematically studied. The small discrepancies (less than 0.12 J/m^2 in surface energy and 0.07 eV in vacancy formation energy) between the results in this work and previous studies are due to the variation in the used methods. Although vacant surface requires higher formation energy than the perfect surface, the energy gap is surmountable, implying the possibility of large scale creation.

Table 4.2 Calculated surface energy and vacancy formation energy of the perfect and vacant (111) surfaces from this work and literature.

	Perfect (111)	Vacant (111)
Surface energy (J m^{-2})	2.02 (1.96[16])	2.16 (2.04[17])
Vacancy formation energy (eV)	NA (no vacancy)	0.89 (0.82[17])

4.3.2 HCOOH Production

Based on the study by Hori and co-workers, the Faradaic efficiency of formic acid on Cu electrode can be as high as 9.4% in 0.1 M $KHCO_3$ at 18.5 °C.[18] As shown in Figure 12 in Chapter 3, the formation of HCOOH requires two proton-electron transfers. Interestingly, two possible mechanisms may lead to the same final product of formic acid, via an intermediate of *COOH and *OCHO, respectively. Based on the free energy pathway in Figure 4.5, for all the simulated surfaces, the formation of *OCHO intermediate, where the first transferred proton is coupled with the carbon atom, is energetically favored. The free energy differences between *COOH state and *OCHO state on these surfaces are more than 0.53 eV, indicating the great thermal advantage of *OCHO formation. This discovery is consistent with the results in previous studies, where the formic acid formation reaction is studied on Cu(211) surface.[19] The stronger binding of *OCHO intermediate may result from the co-interaction of the two O atoms with the catalyst surface, while only one C atom can interact with the catalyst in *COOH configuration.

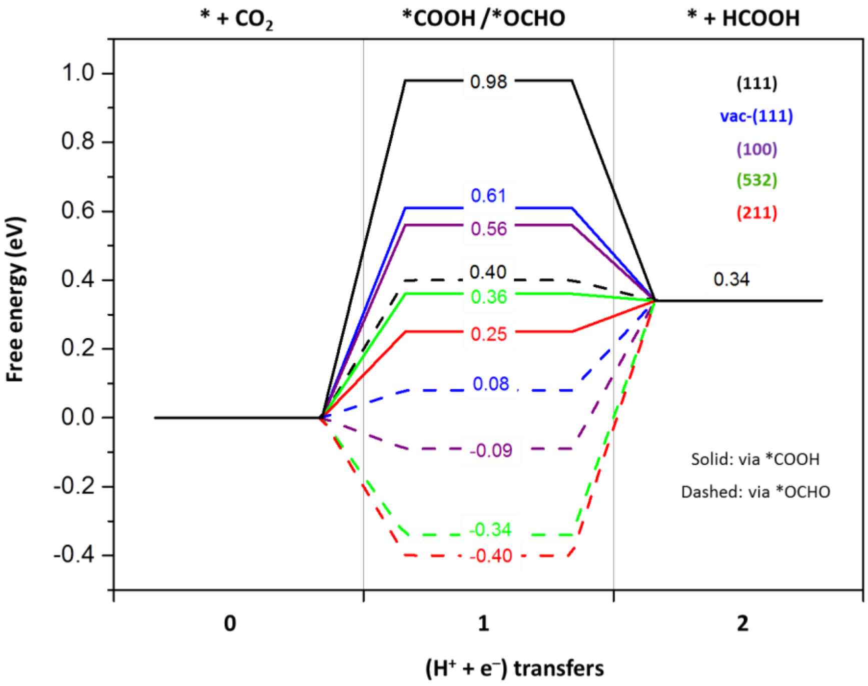

Figure 4.5 Free energy diagram for the lowest energy pathways to HCOOH on the simulated surfaces.

However, although *OCHO configurations are more stable than *COOH ones, the most economic pathway to generate HCOOH varies on different Cu sites. As summarized in Table 4.3, HCOOH formation prefers to go through a *COOH inter-state on (211) and (532) surfaces, while a *OCHO state is energetically favored on the rest three surfaces. On the full-coordinated (111) atoms, the highest uphill change in free energy to generate HCOOH is 0.40 eV. Comparatively, on the low-coordinated surfaces, the changes are much different from that of (111) atom. On the (100) surface, a slightly higher free energy, 0.43 eV, is required for the HCOOH generation. However, on the other low-coordinated surfaces, smaller changes in free energy are observed. On (532) and vac-(111) surfaces, a 0.36 eV and 0.26 eV uphill free energies, respectively, are needed. On the (211) surface, the free energy change is only 0.25 eV, which gives rise to an estimated limiting potential of -0.25 V (RHE). Hence, although the low-coordinated atoms in (100) surface displays a higher uphill free energy change, the overall trend on all the studied four low-coordinated sites indicates lowered free energy pathway to generate HCOOH. The advantage in free energy strongly suggests the HCOOH formation can be faster on the low-coordinated sites, thus proving the proposed hypothesis.

Table 4.3 Calculated free energy change of the rate-determining step and the corresponding reaction intermediate.

Surface	Most uphill change in free energy (eV)	Reaction intermediate
(111)	0.40	*OCHO
(100)	0.43	*OCHO
vac-(111)	0.26	*OCHO
(211)	0.25	*COOH
(532)	0.36	*COOH

4.3.3 CO Production

As an important industrial raw material, carbon monoxide is a major reduction product on noble metals in electro-chemical CO_2 conversion. However, on pure Cu electrode, the Faradaic yield of CO is quite low (1.3%, reported by Hori et al.).[18] Interestingly, R. Kas and co-workers have synthesized a three-dimensional porous hollow fiber copper electrode, which could selectively catalyze CO_2 into CO with a maximum Faradaic efficiency of 75% at a potential of 0.4 V (RHE).[20] The authors attributed the remarkable electro-catalytic performance to the defect-rich structure and the extraordinary mass transport conditions. In this section, theoretical investigations of the low-coordinated Cu atoms in catalyzing CO_2 into CO are systematically performed.

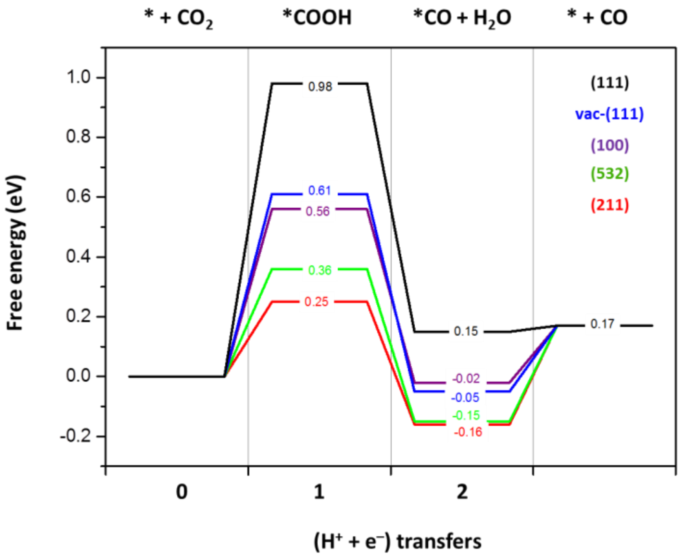

Figure 4.6 Free energy diagrams for the lowest energy pathways to CO on the simulated surfaces.

Three thermal steps are involved in producing CO from electrochemical CO_2 reduction reaction. As illustrated in Figure 4.6, the first transferred proton-electron pair combines the gaseous CO_2 at the catalyst surface and forms a *COOH binding intermediate. Following that, the second transferred proton-electron pair breaks the C-O bond and yields one H_2O molecule, leaving an adsorbed *CO state on the catalyst. Finally, the *CO directly desorbs from the catalyst surface and generates the carbon monoxide gas. According to the free energy diagram, among all the simulated Cu sites, the first and third elementary steps are uphill while the second step is downhill. Similar to the trend observed in HCOOH formation diagram, the intermediates bind most tightly to the stepped (211) surface and most loosely to the plain (111) surface. The free energy of *COOH on (211) surface is 0.25 eV, almost in line with the quarter value (74.5% decrease) of that on (111) surface (0.98 eV), suggesting the thermal advantage of the stepped sites. Additionally, the (532) surface can also significantly lower the energy state of the intermediates, with a free energy of 0.36 eV and -0.15 eV for the *COOH and *CO states, respectively. Moreover, although atoms in the vac-(111) and (100) surfaces show quite similar free energy states of each reaction coordinate, , obvious decrease in free energy can still be observed comparing to the free energy states of the full-coordinated (111) atom. Hence, the overall trends indicate the enhanced binding affinities of carbon based intermediates on low-coordinated Cu atoms.

Table 4.4 Predicted onset potentials and the rate-determining step of the simulated surfaces.

Surface	Theoretical estimated onset potential (V *vs.* RHE)	Rate-determining step
(111)	-0.98	$CO_2 + * + (H^+ + e^-) \rightarrow *COOH$
(100)	-0.56	$CO_2 + * + (H^+ + e^-) \rightarrow *COOH$
vac-(111)	-0.61	$CO_2 + * + (H^+ + e^-) \rightarrow *COOH$
(211)	-0.33	$*CO \rightarrow CO\uparrow + *$
(532)	-0.36	$CO_2 + * + (H^+ + e^-) \rightarrow *COOH$

The estimated potentials (RHE) at which the CO formation reaction will open on various Cu sites have been summarized in Table 4.4, together with the rate determining step. Interestingly, although the second elementary step ($*COOH + H^+ + e^- \rightarrow *CO + H_2O$) is always a downhill process, it will affect the onset potential if the free energy goes too low. The case was found on (211) surface, where the low energetic state of *CO makes the final elementary process the rate-determining step. This phenomenon is consistent with the Sabatier Principle in catalysis domain, stating that a good catalyst should bind the key intermediate with a proper strength, neither too strong nor too weak. Energetically, the average starting potential on the full-coordinated sites is higher than that on the low-coordinated sites. The predicted onset potential is only -0.33 V (RHE) on the (211) surface sites, almost one third of the value on (111) surface sites. Therefore, higher reaction rate of CO generation can be rationally expected on the defective Cu electrodes, where large numbers of low-coordinated sites are contained.

4.3.4 CH_3OH Production

Methanol is an important industrial raw material to synthesize gasoline, chloromethane, methylamine, and formaldehyde. Additionally, methanol can be used as a rough rocket fuel and as antifreeze in the cooling system of cars. The wide applications of methanol have made it an urgent demand to generate methanol through a sustainable approach. Although production rate of methanol is quite low on metallic Cu electrode (roughly 4 orders of magnitude less than that of methane), it has been found that methanol is one of the major reduction products at high applied potentials (-1.10 V *vs.* RHE).[21]

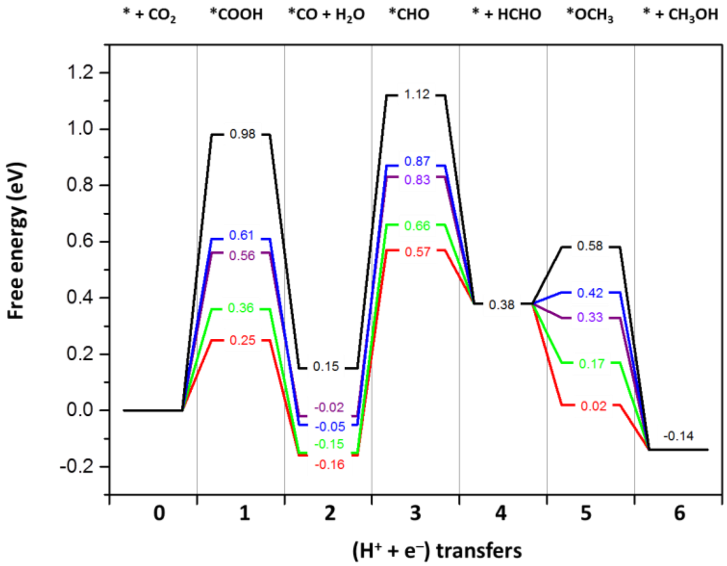

Figure 4.7 Free energy diagram for the production of CH_3OH on the simulated surfaces.

According to the reaction diagram in Figure 4.7, the CH_3OH formation reaction will open when the elementary step of *CO hydrogenation becomes exergonic. It has been reported that methanol could also possibly be produced via the formation of hydrated formaldehyde.[22] Hence, the state of formaldehyde chemisorption has also been calculated. Based on the results (Table 4.5), formaldehyde cannot adsorb on (111) and vac-(111) surface. Moreover, although it is possible for formaldehyde to adsorb on the other three low-coordinated surfaces, the free energy for the adsorbed state is much higher than the desorbed state, suggesting the difficulty of forming the *CH_2O species. Therefore, considering the thermal advantage of desorbing CH_2O from all these surfaces, it is expected that the formaldehyde pathway should be negligible in producing methanol.

Table 4.5 Free energy states of adsorbed and desorbed formaldehyde and free energy change of the rate-determining step for CH_3OH production.

	(111)	vac-(111)	(100)	(532)	(211)
G(*CH_2O) / eV	--	--	0.87	0.70	0.84
G(CH_2O + *) / eV	0.38	0.38	0.38	0.38	0.38
ΔG(*CO→*CHO) / eV	0.97	0.92	0.85	0.81	0.73

Among all the simulated surfaces, (111) requires the largest energy input to make this reaction happen; while (211) needs the lowest uphill change to generate CH_3OH. This trend is consistent with those obtained in other products. Compared with the perfect (111) surface, the free energy change has been lowered by only 0.05 eV (from 0.97 eV to 0.92 eV) on vac-(111) surface, suggesting the limited reaction enhancement on the surface vacancy site. On the other low-coordinated sites, obvious decreases on the free energy change have been observed. On the (100) and (532) surface sites, the free energy change of the rate limiting step has been lowered by 0.12 eV and 0.16 eV, respectively. The reaction requires the lowest energy input on (211) surface, where only 0.73 V (RHE) onset potential is estimated to be needed to produce CH_3OH. Hence, based on the above results, it can be rationally concluded that compared with the full-coordinated sites, the low-coordinated sites can catalyze CO_2 more effectively to produce methanol.

4.3.5 CH_4 Production

Based on Hori's study, the Faradaic yield of hydrocarbons on Cu electrode in CO_2 reduction can be as high as 72.3% at -1.05 V (RHE) in a 0.1 M $KHCO_3$ buffer.[18] Among all the hydrocarbons, methane is the dominant one at sufficient negative potentials. Mechanisms of CH_4 formation have been studied by many groups and interestingly, it has been found that two possible pathways may lead to methane production on different Cu surfaces. These two pathways differ in the hydrogenation step of the *CO species, where the next transferred proton and electron pair may attach to either the carbon atom or the oxygen atom. However, based on Nørskov's reports, the *CHO intermediate is preferred on Cu(211) surface.[23] In this study, since the focus is the low-coordinated Cu sites and the overpotential trend, the *CHO process is chosen as the reaction pathway for the calculation.

Reaction diagrams in Figure 4.8 have revealed the same rate-determining step to generate methane as methanol. The difference between methane and methanol generation comes from step 6, where the transferred proton-electron pair could interact with either a carbon atom or an oxygen atom. The product from elementary step 5 leaves an adsorbed $*OCH_3$ species on the catalyst surface. In step 6, if the proton-electron pair couples with the O atom, methanol will be produced and reaction will stop here. However, if the proton-electron pair interacts with the C atom and breaks the C–O bond, methane will be generated and the adsorbed *O species will be left on the catalyst surface.

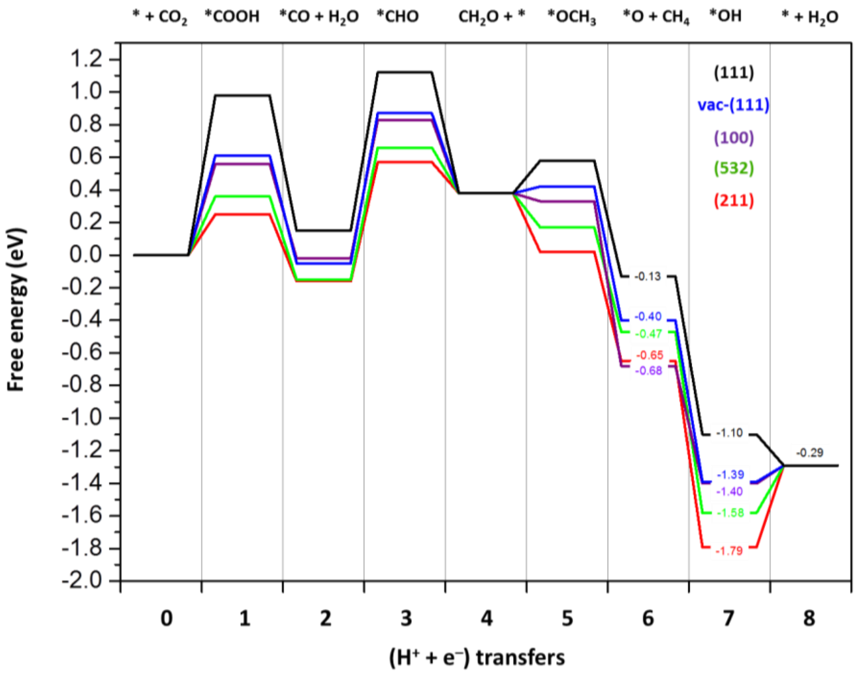

Figure 4.8 Free energy diagram for the production of CH_4 on the simulated surfaces.

Table 4.6 Free energy states of the production of methanol and methane.

	(111)	vac-(111)	(100)	(532)	(211)
G(CH_3OH + *) / eV	-0.14	-0.14	-0.14	-0.14	-0.14
G(CH_4 + *O) / eV	-0.13	-0.40	-0.68	-0.47	-0.65
ΔG (CH_3OH – CH_4) / eV	-0.01	0.26	0.54	0.33	0.51

The Gibbs free energy states of methanol and methane formation on the simulated surfaces are summarized in Table 4.6. It can be seen that the energy difference between CH_4 and CH_3OH formation is quite close on the full-coordinated atomic sites (-0.13 eV *vs.* -0.14 eV), suggesting the same chance for the formation of both products. Interestingly, things become very different on the low-coordinated sites, where much more stable states are found for methane formation. On the (100) surface sites, the energy difference is 0.54 eV, implying the enormous advantage of methane generation. Other low-coordinated sites also display obvious thermal preference for methane generation;

specifically, a 0.51 eV difference is found on (211) surface, while 0.26 eV and 0.33 eV are found on vac-(111) and (532) sites, respectively. Since the low-coordinated sites are more active than the full-coordinated ones, the real experimental situations are better represented by the trend on the low-coordinated sites than that on the full-coordinated sites. Hence, the thermal advantage of methane formation on the low-coordinated Cu atoms may rationally explain why methane is the main hydrocarbon product on Cu electrode in catalyzing CO_2 conversion while methanol only has trace yield.

4.3.6 Performance of HER

In solid-water interface systems, large numbers of hydrogen ions are contained regardless of whether the solution is acidic or basic. Hence, hydrogen evolution reaction (HER) must be taken into consideration, as it takes place at the same cathode surface and competes for the electrons against CO_2ER. Previous reports have proved that Cu(111) is not an excellent surface to catalyze HER, since the hydrogen atom binds loosely on it, making the chemisorptions free energy (ΔG_{H^*}) positively far from the optimal value (0 eV).[24]

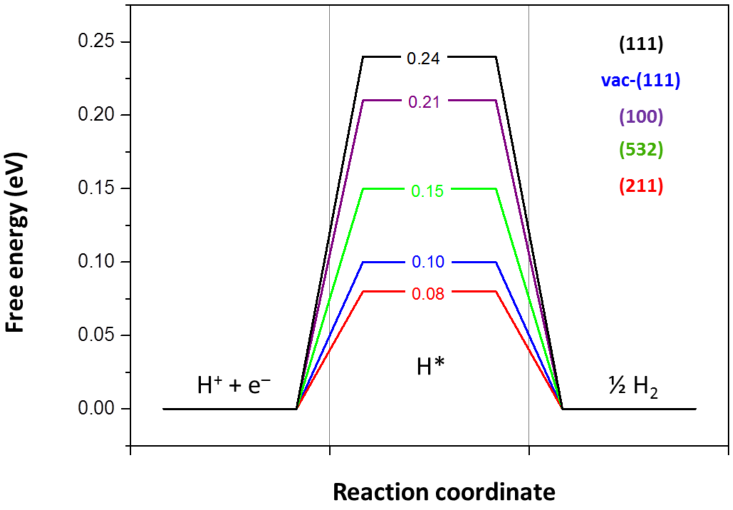

Figure 4.9 Free energy diagram of HER on the simulated surfaces.

As shown in Figure 4.9, the calculated free energy of H adsorption on the plain (111) is 0.24 eV. A ΔG_{H^*} in this value suggests the H chemisorptions process is the rate-determining step for HER. However, on the low-coordinated Cu sites, much lower values are obtained for the ΔG_{H*}; specifically, 0.21 eV, 0.10 eV, 0.15 eV, and 0.08 eV are generated on (100), vac-(111), (532), and (211) surfaces, respectively. Energetically, this trend is consistent with those discovered in CO_2ER, where the energy states of carbon based intermediates are all lowered on the low-coordinated sites. The lowered values imply enhanced HER activities on the low-coordinated Cu sites. In the process of catalyzing CO_2ER, HER is an unwanted reaction and a good catalyst should not boost HER. Unfortunately, although previous data has revealed an accelerated rate for all the CO_2 reduction reactions, the competing HER has also been boosted and this may lead to low Faradaic efficiencies for CO_2 reduction products at low applied potentials. Therefore, more careful structural modifications need to be created on the low-coordinated Cu sites in order to suppress HER.

4.3.7 *d*-band Structures

According to the theory proposed by Nørskov, the gravity center of metal *d*-band gives the final explanations to the binding affinities of different metal surfaces towards small adsorbates (those interacting with the surface through one single atom).[25] As detailedly elaborated in Chapter 3, a higher value of metal d-band center relative to the Fermi level gives rise to a stronger metal-adsorbate interaction, resulting in a lower thermal binding energy.

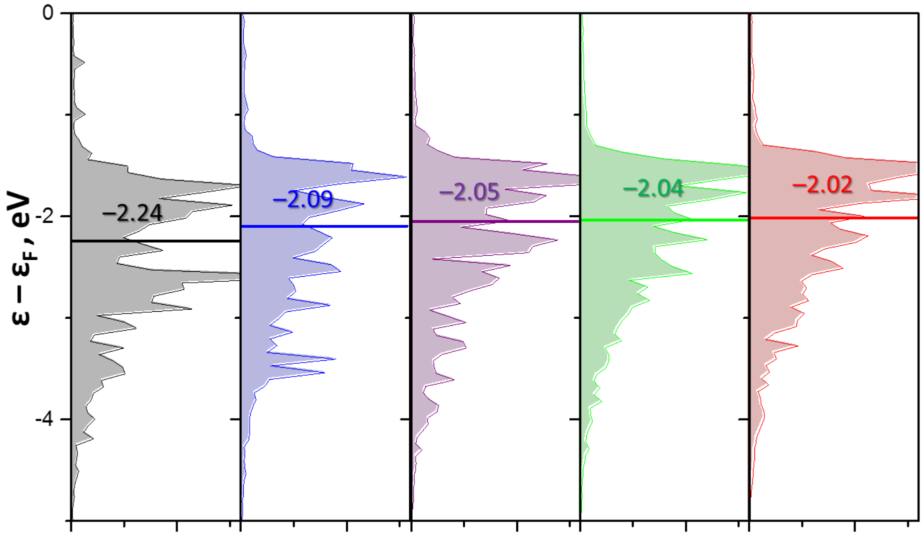

Figure 4.10 *d*-orbital density of states of the simulated surfaces.

In order to confirm the validity of the computed free energies, the projected density of states for each simulated surface has been calculated and the results are illustrated in Figure 4.10. The trend of the d-band center is obvious. Of all the low-coordinated atoms, their energetic center of d-orbital electrons is higher than that of the full-coordinated atom in the topmost layer of (111) surface. Specifically, (211) surface atom displays the highest d-orbital center, followed by (532) atom, (100) atom, vac-(111) atom, and clean (111) atom. This trend is precisely accordant with that of the binding energies for the adsorbed reaction intermediates, where the adsorbates bind most tightly on the (211) surface while most loosely on the clean (111) surface. The d-band center changes by 0.22 eV between the (111) atom and the (211) atom, consistent with the previously reported result, where an approximate 0.2 eV change was discovered between the d-band center of the atoms on the two Cu surfaces.[26] In other words, the d-band center clearly justifies the obtained trend in the free energies and the accordingly drawn conclusions.

In previous studies, researchers have investigated the structural effects on Cu nanoparticles. For example, Nørskov and coworkers have theoretically studied the reduction of CO_2 to CH_4 on Cu(211) and Cu(100), and proved that Cu(211) is more active than plain (100) surface.[26] Experimentally, R. Kas and coworkers found that the porous hollow fiber Cu electrode can catalyze CO_2 into CO with low reaction overpotential than Cu nanoparticles, suggesting the low-coordinated Cu sites are active for CO_2ER.[20] However, to the best of our knowledge, no one has systematically studied CO_2ER on all types of the low-coordinated Cu sites. In this work, we have performed a thorough study on the catalytic activity of four different types of low-coordinated Cu sites. Moreover, all possible reduction product of CO_2 on Cu particles, including hydrocarbons, HCOOH, CO et al. have been evaluated and a general reaction trend on the low-coordinated Cu sites was obtained. Since Cu is so far the only metallic candidate that can possibly catalyze CO_2 into hydrocarbons, it is believed that this systematical work is of significance to provide useful guidance for designing new promising electro-catalysts by using Cu.

4.4 Conclusions

To investigate the role of low-coordinated Cu sites in catalyzing CO_2 reduction reaction, five kinds of low-coordinated sites, together with one full-coordinated (111) surface, have been simulated and reactions for each mono-carbide formation have been performed on these simulated sites. The d-orbital center reveals the validity of the computed energetic states and the accordingly obtained conclusions.

(1) Of all the low-coordinated sites, lowered free energy states for CO_2ER intermediates are observed, resulting in decreased estimated onset potentials for the mono-carbides generation. Also, these results confirm that low-coordinated sites are responsible for the overall catalytic behaviors on Cu electrodes thus proving the hypothesis, since they are more catalytically active than the full-coordinated sites.

(2) The more economic energetic pathway in generating CH_4 rather than CH_3OH effectively explains why Cu can selectively catalyze CO_2 into methane. The protonation of $*OCH_3$ species plays the key role in determine the type of hydrocarbon product. The thermal advantage for H interacting with carbon atom results in the formation of CH_4.

(3) For the unwanted HER, the low-coordinated sites can also catalyze it more efficiently than the full-coordinated ones. Hence, although CO_2ER can perform actively on the low-coordinated sites, the unavoidable HER will, at the same time, compete for the transferred electrons and affect the Faradaic efficiency of CO_2ER products. Thus, in order to take full advantage of the low-coordinated sites for catalyzing CO_2ER, high operation potentials are required, where both these two types of reactions are kinetically opened.

References

1 Chen, Y., Li, C. W. & Kanan, M. W. Aqueous CO2 reduction at very low overpotential on oxide-derived Au nanoparticles. *Journal of the American Chemical Society* **134**, 19969-19972 (2012).

2 Li, C. W., Ciston, J. & Kanan, M. W. Electroreduction of carbon monoxide to liquid fuel on oxide-derived nanocrystalline copper. *Nature* **508**, 504-507 (2014).

3 Mistry, H. *et al.* Exceptional size-dependent activity enhancement in the electroreduction of CO_2 over Au nanoparticles. *Journal of the American Chemical Society* **136**, 16473-16476 (2014).

4 Gao, D. *et al.* Size-dependent electrocatalytic reduction of CO_2 over Pd nanoparticles. *Journal of the American Chemical Society* **137**, 4288-4291 (2015).

5 Reske, R., Mistry, H., Behafarid, F., Roldan Cuenya, B. & Strasser, P. Particle size effects in the catalytic electroreduction of CO_2 on Cu nanoparticles. *Journal of the American Chemical Society* **136**, 6978-6986 (2014).

6 Lu, Q. *et al.* A selective and efficient electrocatalyst for carbon dioxide reduction. *Nature Communications* **5**, 3242 (2014).

7 Lee, H.-E. *et al.* Concave rhombic dodecahedral Au nanocatalyst with multiple high-index facets for CO_2 reduction. *ACS Nano* **9**, 8384-8393 (2015).

8 Jianping, Q. *et al.* Preparation of a silver electrode with a three-dimensional surface and its performance in the electrochemical reduction of carbon dioxide. *Electrochimica Acta* **203**, 99-108 (2016).

9 Kuld, S. *et al.* Quantifying the promotion of Cu catalysts by ZnO for methanol synthesis. *Science* **352**, 969-974 (2016).

10 Straumanis, M. & Yu, L. Lattice parameters, densities, expansion coefficients and perfection of structure of Cu and of Cu–In α phase. *Acta Crystallographica Section A: Crystal Physics, Diffraction, Theoretical and General Crystallography* **25**, 676-682 (1969).

11 Kresse, G. & Furthmüller, J. Efficient iterative schemes for ab initio total-energy calculations using a plane-wave basis set. *Physical Review B* **54**, 11169 (1996).

12 Blöchl, P. E. Projector augmented-wave method. *Physical Review B* **50**, 17953-17979 (1994).

13 Hammer, B., Hansen, L. B. & Nørskov, J. K. Improved adsorption energetics within density-functional theory using revised Perdew-Burke-Ernzerhof functionals. *Physical Review B* **59**, 7413-7421 (1999).

14 Monkhorst, H. J. & Pack, J. D. Special points for Brillouin-zone integrations. *Physical review B* **13**, 5188 (1976).

15 Nørskov, J. K. *et al.* Origin of the overpotential for oxygen reduction at a fuel-cell cathode. *The Journal of Physical Chemistry B* **108**, 17886-17892 (2004).

16 Skriver, H. L. & Rosengaard, N. Surface energy and work function of elemental metals. *Physical Review B* **46**, 7157 (1992).

17 Tafreshi, S. S., Roldan, A. & de Leeuw, N. H. Density Functional Theory Study of the Adsorption of Hydrazine on the Perfect and Defective Copper (100),(110), and (111) Surfaces. *The Journal of Physical Chemistry C* **118**, 26103-26114 (2014).

18 Hori, Y., Wakebe, H., Tsukamoto, T. & Koga, O. Electrocatalytic process of CO selectivity in electrochemical reduction of CO_2 at metal electrodes in aqueous media. *Electrochimica Acta* **39**, 1833-1839 (1994).

19 Peterson, A. A., Abild-Pedersen, F., Studt, F., Rossmeisl, J. & Norskov, J. K. How copper catalyzes the electroreduction of carbon dioxide into hydrocarbon fuels. *Energy & Environmental Science* **3**, 1311-1315 (2010).

20 Kas, R. *et al.* Three-dimensional porous hollow fibre copper electrodes for efficient and high-rate electrochemical carbon dioxide reduction. *Nature Communications* **7** 10748 (2016).

21 Kuhl, K. P., Cave, E. R., Abram, D. N. & Jaramillo, T. F. New insights into the electrochemical reduction of carbon dioxide on metallic copper surfaces. *Energy & Environmental Science* **5**, 7050-7059 (2012).

22 Hansen, H. A. *et al.* Electroreduction of methanediol on copper. *Catalysis Letters* **143**, 631-635 (2013).

23 Peterson, A. A. & Nørskov, J. K. Activity Descriptors for CO2 Electroreduction to Methane on Transition-Metal Catalysts. *The Journal of Physical Chemistry Letters* **3**, 251-258 (2012).

24 Nørskov, J. K. *et al.* Trends in the exchange current for hydrogen evolution. *Journal of The Electrochemical Society* **152**, J23-J26 (2005).

25 Hammer, B. & Nørskov, J. K. Theoretical surface science and catalysis—calculations and concepts. *Advances in Catalysis* **45**, 71-129 (2000).

26 Durand, W. J., Peterson, A. A., Studt, F., Abild-Pedersen, F. & Nørskov, J. K. Structure effects on the energetics of the electrochemical reduction of CO_2 by copper surfaces. *Surface Science* **605**, 1354-1359 (2011).

Chapter 5

Cu Surface Alloys for Electrochemical CO_2 Reduction Reactions

*Surface alloying is a compositional modification strategy that has been employed in creating effective bimetallic surfaces with balanced binding affinity to adsorbates. Nevertheless, in the domain of CO_2ER, few works regarding surface alloys (SAs) have been reported. Therefore, in this chapter, we systematically screened the catalytic activity of Cu SAs doped by transition metals. The stabilities of various SAs have been tested in two aspects: the vertical segregation energy and the horizontal mixing energy. Eight transition metals (Au, Ag, Zn, Pd, Pt, Cd, Sc, and Y) were found to stably alloy Cu at the topmost layer. The computation results of their catalytic performances on CO_2ER and the competing HER showed that dopants of random Zn and small amount of Ag and Cd retain the same onset potential for generating CH_4 while significantly enlarge the one for the competing HER. Moreover, the presence of high doping concentration of Cd is identified as a promising candidate to have increased catalytic efficiency (decreased overpotential for CO_2ER and increased one for the unwanted HER) as well as improved product selectivity toward HCOOH due to its prevention of the hydrocarbon production (cannot capture *CO).*

5.1 Introduction

Compositional modifications have long been employed in heterogeneous catalysis as effective approaches to design excellent catalysts. The enhanced catalytic performance is attributed to the unique binding affinities of the local multi-metallic area to the key reaction intermediates, which may bring chances in producing binding energies close to the benchmark level.[1] Specifically, bulk alloying, surface doping, and metal overlayer coating are the three most commonly used treatments in compositional modifications (Figure 5.1).[2] In CO_2 electro-reduction reaction (CO_2ER) field, tremendous experimental efforts have been spent in creating decent catalysts through bi- or multi-metallic compositions.[3-6]

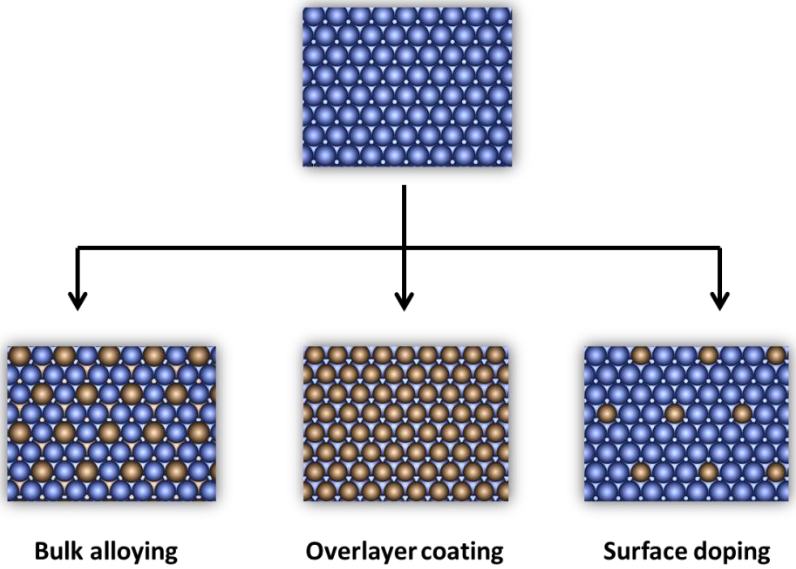

Figure 5.1 Three most commonly employed strategies of compositional modifications for advanced catalyst design.

Unfortunately, although compositionally modified catalysts with significant catalytic performances have been reported, theoretical investigations on the catalytic role of the multi-metallic surfaces are still lacking. For bulk alloying strategies, Hirunsit and co-workers have reported the reaction pathways of CO_2 electro-reduction to methane on several Cu bulk alloys (Cu_3Ag, Cu_3Au, Cu_3Pd, Cu_3Rh).[7,8] Adopting the scaling relation method, Yousung Jung and co-workers have computationally predicted the capabilities of methanol formation from CO_2 electro-chemical reduction on various types of metal overlayer systems, which provides useful guidance in directing the experimental synthesis.[9] However, so far no work has thoroughly and comprehensively studied the activities of doped metallic systems (surface alloys) in catalyzing CO_2ER. Therefore, in this chapter, a systematical study on the catalytic behaviors of transition-metal doped Cu particles (Cu surface alloys) towards CO_2ER has been performed to predict good candidates as CO_2 electro-chemical reduction catalysts (Figure 5.2).

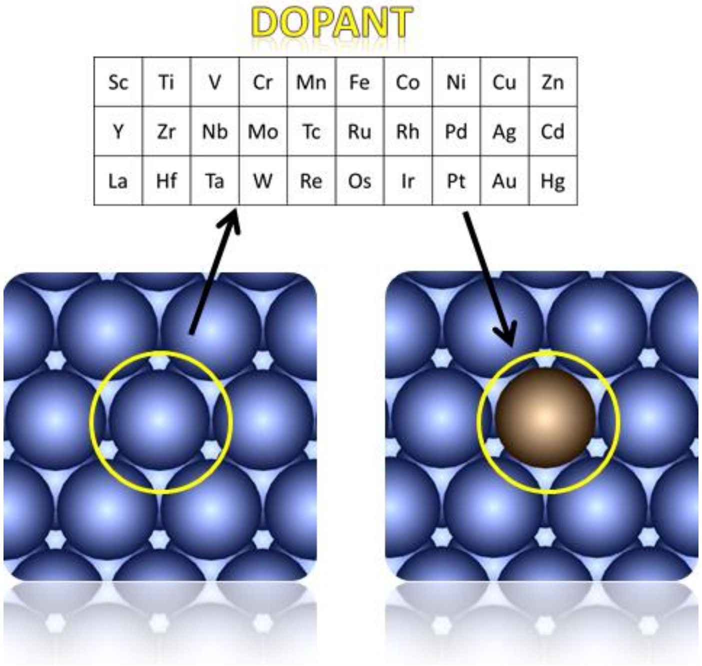

Figure 5.2 Schematic of the screening work on Cu surface alloys.

In the SA screening, Cu has been chosen as the substrate metal due to its unique catalytic activity towards electro-chemical CO_2 reduction reaction. Moreover, Cu is the only metal displaying the potential to catalyze CO_2 into hydrocarbons.[10] Since hydrocarbons have wide range of applications in industry, it is of vital meaning to research the catalytic behaviors of Cu surface alloys (SAs) in CO_2 reduction reaction. The stability of Cu systems alloyed with different transition metals was firstly tested. After performing the stability test, those stably existed SAs were selected and the scaling relations were plotted in order to build up the volcano plot for CO_2 reduction to methane. Meanwhile, the competing HER performance on these stable Cu SAs were also computed. By combining the results from the two reactions, the Cu SAs that can selectively enhance CO_2 reduction reaction while suppress HER are predicted as good candidates for CO_2 reduction catalysts.

5.2 Computational Details

5.2.1 Surface Stability

When one guest metal is doped into another metal particle, various phenomena may occur. The doped metal may form islands on the substrate or it may alloy into the first or deeper layer. The multiple observed possibilities have made it important to be able to categorize the doped bimetallic system. Hence, to screen the catalytic performance of different doping systems, the structure stability is the first thing that needs to be evaluated. In this section, applying the approach proposed by Nørskov, the stabilities of the surface alloys have been thermodynamically estimated from two aspects: the vertical segregation energy and the horizontal mixing energy.[11]

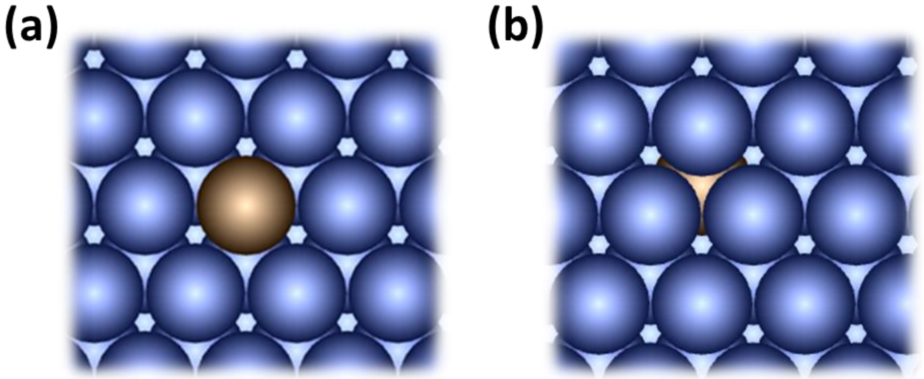

Figure 5.3 Illustration of the two vertical situations occurred when one metal is deposited onto another: (a) the deposited metal stays in the first layer of the substrate; (b) the deposited metal stays in deeper layers of the substrate.

The segregation energy is the electronic energy difference between a surface doped system and a sub-surface doped one (Figure 5.3) and is used to judge whether the dopant atom prefers to stay in the topmost surface or the deeper layer of the substrate. By definition, it can be written as:

$$E_{seg} = E_{sur} - E_{sub-sur} \quad (5.1)$$

where E_{sur} and $E_{sub-sur}$ are the total electronic energies of the Cu substrate with a surface dopant and with a sub-surface dopant, respectively. Computationally, the doping process is represented by substituting one atom in the slab models of Cu with one dopant.

Since the dopant atoms are the minority compared with the substrate ones, it is believed that this model could effectively describe the two possible doping systems and generate reliable trend to estimate the vertical stability.

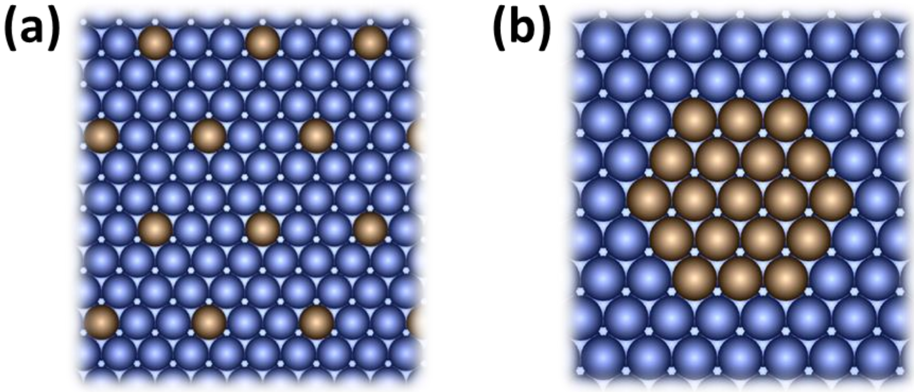

Figure 5.4 Illustration of the two horizontal situations occurred when one metal is deposited onto another: (a) the deposited metal alloys the substrate; (b) the deposited metal forms separated phases from the substrate.

The mixing energy is the surface energy difference between an alloying situation and a phase-separated one (see Figure 5.4). It describes whether the two types of metals will alloy or form separated phases. By definition, the mixing energy can be expressed as:

$$E_{mix} = \varepsilon_{alloy} - \varepsilon_{sep} \tag{5.2}$$

where ε_{alloy} and ε_{sep} are the surface energies of an alloying system and a phase-separated one, respectively. Since the supercell of the simulated slab model is not big enough to represent an island-isolated phase, a linear relationship among surface energies in slab models containing different percentages of isolated phase is assumed. This approach was firstly introduced by Nørskov and co-workers and had been proven to be reliable in predicting the horizontal stability of surface alloys.[11]

5.2.2 Structure Models

In order to describe the CO_2ER on different doped Cu particles, slab models are created using the (211) geometry.

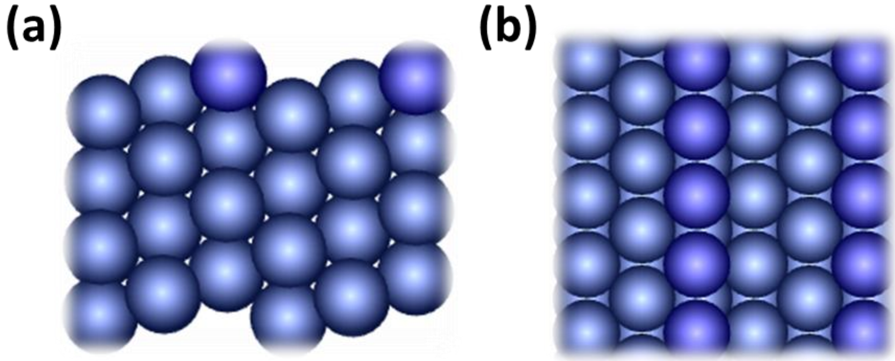

Figure 5.5 Illustration of the (211) orientation of Cu: (a) side view; (b) top view. The lines of edge atoms are highlighted in dark blue.

A detailed illustration of the (211) geometry is shown in Figure 5.5. A stepped-like surface is exposed with a line of atoms being possible to activate the catalysis reaction (the highlighted atoms in Figure 5.5). Theoretically, the active atoms on (211) surface can approximately represent the edge sites in metal nanoparticles, since both conditions have a line of atoms outside the bulk structure. It has been proved that the (211) geometry is the most active surface in hydrogenating the chemisorbed *CO species – a process of critical importance in hydrocarbon formation. Together with the fact that edge atoms are usually considered as the catalytically active sites, it is believed that the (211) surface is very representative in providing useful guidance in predicting the catalytic performance of doped Cu particles.

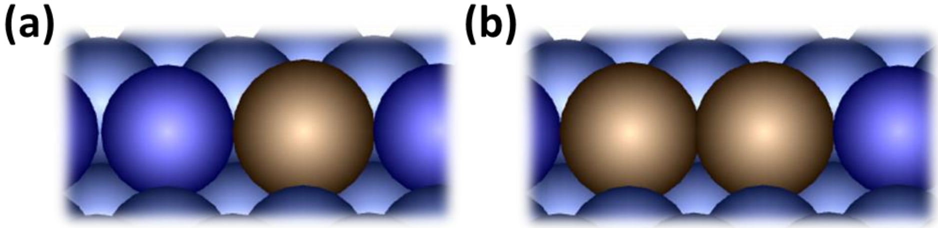

Figure 5.6 The two types of SA models used in this work: (a) low concentration doping, with a Cu-M-Cu edge; (b) high concentration doping, with a M-M-Cu edge.

To conduct a thorough study on the catalytic activity of doped Cu particles, all the transition metals except Hg have been taken into account. The exclusion of Hg is because it is a liquid metal so that the stability information cannot be reliably provided. Computationally, doping is created by substituting one active atom in Cu(211) symmetry with a dopant atom. As shown in Figure 5.6 (a), a local Cu-M-Cu environment can be obtained by low-percentage doping treatment. In order to make the study more comprehensive and complete, higher percentage doping conditions are also considered, where a M-M-Cu bond may occur. Hence, two types of doping models, the M1/Cu and the M2/Cu, have been systematically investigated to represent the low-percentage doping and high-percentage doping, respectively.

5.2.3 Theoretical Methods

Electronic energy calculations were performed using density functional theory (DFT) by the Vienna Ab-Initio Simulation Package[12] (VASP). The projected augmented wave[13] (PAW) method was used to describe ion-electron interactions. The revised Perdew-Burke-Ernzerhof[14] (RPBE) functional of the generalized gradient approximation (GGA) was adopted to describe the exchange and correlation effects. For all the geometry optimizations, a plane-wave cutoff energy of 500 eV was used. The doping systems in stepped (211) geometry were fully optimized until the residual force was less than 0.05 eV/Ǻ without any constraints. For all the calculations, the slab models were constructed using 4 periodically repeated layers, with the top two layers and the adsorbates being allowed to move to the lowest energy configuration while the other layers fixed to their bulk arrangements. A periodic 3 × 3 supercell with a 3 × 3 × 1 Monkhorst-Pack[15] k-point grid was used in all cases. In the z direction, at least 15 Å of vacuum was applied, preventing the models from vertical interactions. Dipole correction was used where necessary. The computational hydrogen electrode[16] (CHE) model was used to calculate the free energy state of each elementary step, detailed explanations of the model can be found in the Chapter 3.

5.2.4 Volcano Plot – Mathematical Details

A volcano-like plot can be generated based on the calculated binding energies, free energy corrections, and scaling relations between binding energies of reaction intermediates.[17] Firstly, according to the CHE model, the Gibbs free energy of an intermediate state, taking *CHO as an example, is given by

$$G(CHO) = E_B[CHO] + G_{corr}[CHO] \tag{5.3}$$

where $E_B[CHO]$ and $G_{corr}[CHO]$ denote the binding energy of *CHO and the Gibbs energy correction for *CHO state, respectively. The Gibbs energy correction contains the solvation correction, the entropy effect, the enthalpy effect, and zero point energy corrections. More detailed explanation about $G_{corr}[CHO]$ can be found in Chapter 3. Secondly, scaling relations can be found among adsorbed species, for example between $E_B[CHO]$ and $E_B[CO]$. This type of scaling relation can be written as

$$E_B[CHO] = a \times E_B[CO] + b \tag{5.4}$$

where *a* and *b* are the slope and the y-intercept of scaling relations, respectively. Converting the scaling relation into Gibbs free energy, the expression is

$$G(CHO) = a \times E_B[CO] + b + G_{corr}[CHO] \tag{5.5}$$

while the expression for G(CO) is

$$G(CO) = E_B[CO] + G_{corr}[CO] \tag{5.6}$$

Using the above relations, the Gibbs energy change of $*CO + (H^+ + e^-) \rightarrow *CHO$ can be simplified as

$$\begin{aligned} \Delta G &= G(*CHO) - G(*CO) - (\mu[H_2] - eU) \\ &= (a \times E_B[CO] + b + G_{corr}[CHO]) - (E_B[CO] + G_{corr}[CO]) - (\mu[H_2] - eU) \\ &= (a-1) \times E_B[CO] - eU + \text{constant} \end{aligned} \tag{5.7}$$

Following $U_L = -\frac{\Delta G^{0V}}{e}$, the limiting potential of each proton-electron transfer step, therefore, can be plotted as a function of $E_B[CO]$. The same procedure can be applied to generate OH-analogous volcano plots.

5.3 Results & Discussions

5.3.1 Stability of Cu Surface Alloys (SAs)

Catalytic activities of Cu surface alloys depend on the atomic structure (the local bimetallic area) of the catalyst surface, which may change with reaction conditions. To gain insight into the surface compositions, the thermodynamic stability of surface alloys was first checked. Stability is tested in two aspects, the vertical segregation energy and the horizontal mixing energy. As previously defined, a negative segregation energy value suggests the guest metal prefers to stay in the topmost surface of Cu substrate; while a negative value of mixing energy indicates the two types of metals will alloy rather than form separated phases.

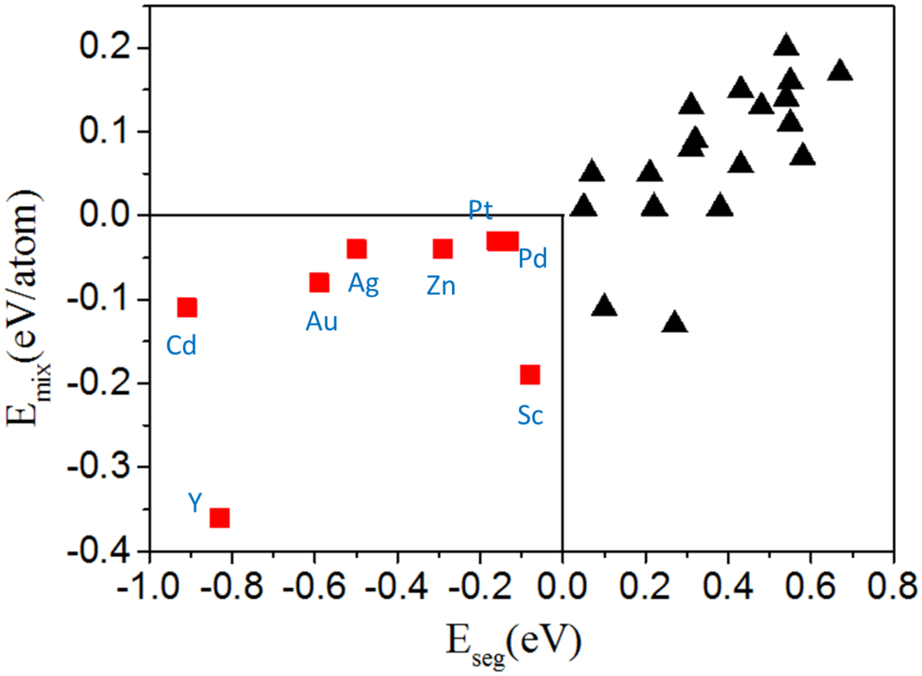

Figure 5.7 Results of the computed segregation energy (E_{seg}) and mixing energy (E_{mix}) on the Cu SAs. The red cubes highlight those who can stably alloy Cu at the topmost layer, with a negative value for both the mixing energy (E_{mix}) and segregation energy (E_{seg}).

In order to create a bimetallic surface, the dopant element must stay in the topmost surface of Cu, since reaction only takes place at the solid-water interface. Hence, it is essential for metals to have a negative value of segregation energy. In addition, since the bimetallic areas are quite small in a phase-separated situation, a negative mixing energy, which refers to an alloying configuration, is desired. Moreover, since the percentage of doping metals is quite low with respect to the substrate material, it is believed that an isolated phase can hardly occur under experimental conditions. Therefore, negative values of both the segregation energy and mixing energy are required for a proper doping metal.

Based on the stability results summarized in Figure 5.7, for the studied 27 transition metals, 19 of them have positive values for both the segregation energy and mixing energy, suggesting deeper layer penetration and separated phases are more preferred. The rest eight candidates – Sc, Au, Ag, Pt, Pd, Y, Cd, and Zn – prefers to alloy Cu at the very top layer, in either a stable or meta-stable form. Interestingly, a similar approach done by Nørskov and co-workers proves Au, Ag, Pd, and Pt can stay in the first layer of Cu. The absence of Sc, Y, Cd, and Zn is because they were not tested in Nørskov's paper, where only selected transition metals have been computed. It's important to note that no external force has been applied in this calculation. Experimentally, driven by the applied potentials, other metals may also be able to alloy Cu at the topmost layer, it is believed the thermal spontaneity of these eight metals can make it much easier for them to form surface alloys on Cu substrate.

To further investigate these eight dopants, the binding affinities of the corresponding SAs to the reaction intermediates have been evaluated. By computing the binding energies, two different situations were observed. For the first situation, the reaction energetics stay similar to that on clean Cu, since the scaling relations are found to suit the binding energies of reaction intermediates. For the other situation, the binding energies of reaction intermediates are found not to scale with each other. The former situation contains dopants of Au, Ag, Zn, Pt, Pd and low concentration Cd. The latter one involves dopants of Sc, Y, and high concentration Cd. In the following sections, the two situations are discussed separately.

5.3.2 Energetics on Au, Ag, Zn, Pd, Pt, and Cd1 Doped Cu SAs

Scaling Relations between Reaction Intermediates. As proposed by Nørskov et al., a possible route to reduce CO_2 to methane involves eight proton-electron pairs, giving rise to seven adsorbed intermediates (see Figure 3.7).[18] Previous results have found that correct predictions of the onset potential for methane formation can be obtained by taking advantage of the computational hydrogen electrode (CHE) analysis.[18] However, given there are seven intermediates in the reduction of CO_2 to methane; such an analysis involves an understanding of the problem in seven-dimensional space of adsorbate-surface interaction energies. Hence, in order to find out the energetic relations between the adsorbed intermediates, the scaling relations are employed in this study.

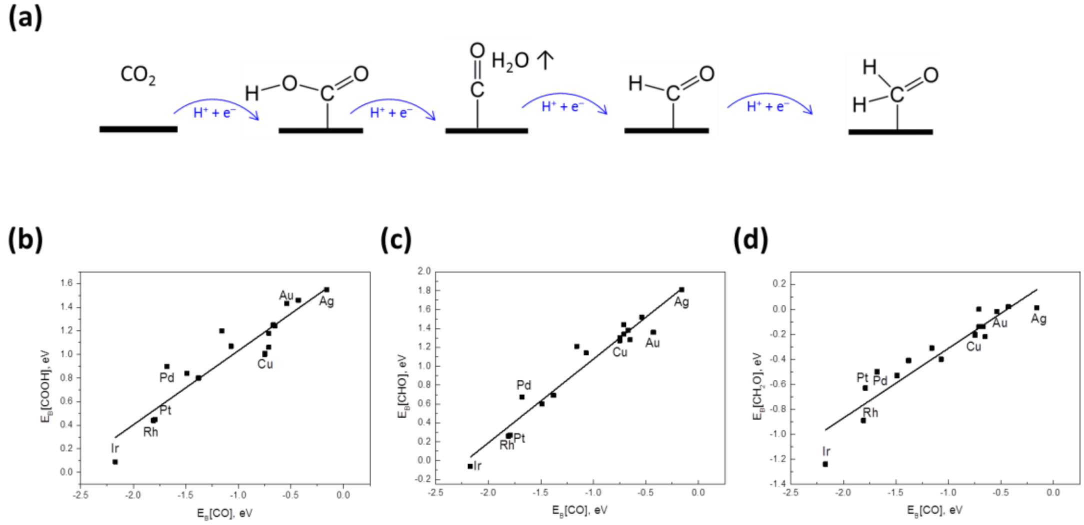

Figure 5.8 (a) The reaction pathway from CO_2 to CH_4 involving the carbon based intermediates. (b) E_B[COOH] (c) E_B[CHO] (d) E_B[CH_2O] as a linear function of E_B[CO].

According to Figure 5.8, the first four reaction intermediates roughly interact with the catalyst surface through a carbon atom. Based on the scaling relations, binding energies of these intermediates may correlate with each other. Hence, the binding energies of *COOH, *CH_2O, and *CHO are linearly plotted as a function of the binding energy of *CO. Similarly, the last three reaction intermediates are found to interact with the catalyst through a single oxygen atom. Therefore, binding energies of *OCH_3 and *O are plotted as a function of the binding energy of *O. Using this strategy, the dimensionality of this reaction network can be reduced from seven to two, making the search for trends within these doped Cu surface alloys tractable.

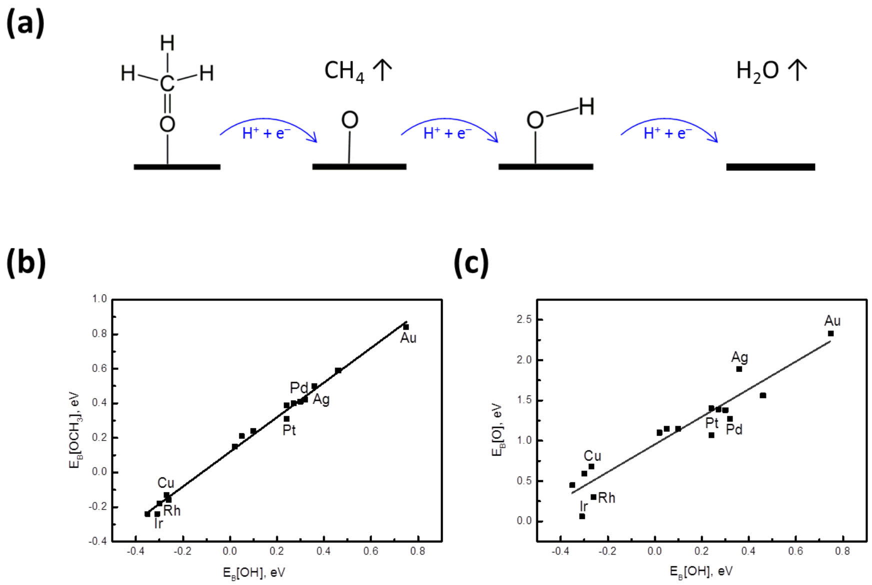

Figure 5.9 (a) The reaction pathway from CO_2 to CH_4 involving the oxygen based intermediates. (b) $E_B[OCH_3]$ (c) $E_B[O]$ as a linear function of $E_B[OH]$.

The full mathematical details of the scaling relations are summarized in Table 7. Based on the standard deviation values, the OH-based intermediates seem to fit the linear relation more perfectly than the CO-based ones. This is due to the appropriate binding geometry of the OH-based intermediates. From the adsorption point of view (Figure 5.10), it is clear that both $*OCH_3$ and *OH precisely interact with the catalyst surface through only one single atom. However, for CO-based species (such as *COOH and *CHO), their slant configurations may bring extra valence linkage between O atom and the surface metal atom, making the binding affinities less relevant with that of *CO. Nevertheless, the overall trend still suggests strong linear relations among the corresponding intermediates. The consistence of slope and intercept (with the difference in slope less than 0.18 and in intercept less than 0.07) between the data in this work and in other reports[9,17] further proves the validity of the obtained relations. The slight change between slope of $E_B[O]$ as a function of $E_B[OH]$ is because this work focuses on Cu surface alloys while in the referenced papers, pure fcc metals and metal over-layer structures are the scope.

Table 5.1 Linear scaling statistics presented in this study and other works (the data in the parenthesis).

Adsorbate	Reference	Slope	Intercept	R^2
COOH	CO	0.62(0.61[9])	1.65(1.64[9])	0.85
CHO	CO	0.89(0.86[9])	1.97(1.90[9])	0.94
CH_2O	CO	0.57(0.54[17])	0.26(0.25[17])	0.87
OCH_3	OH	1.00(0.97[17])	0.12(0.10[17])	0.99
O	OH	1.70(1.88[17])	0.95(0.97[17])	0.88

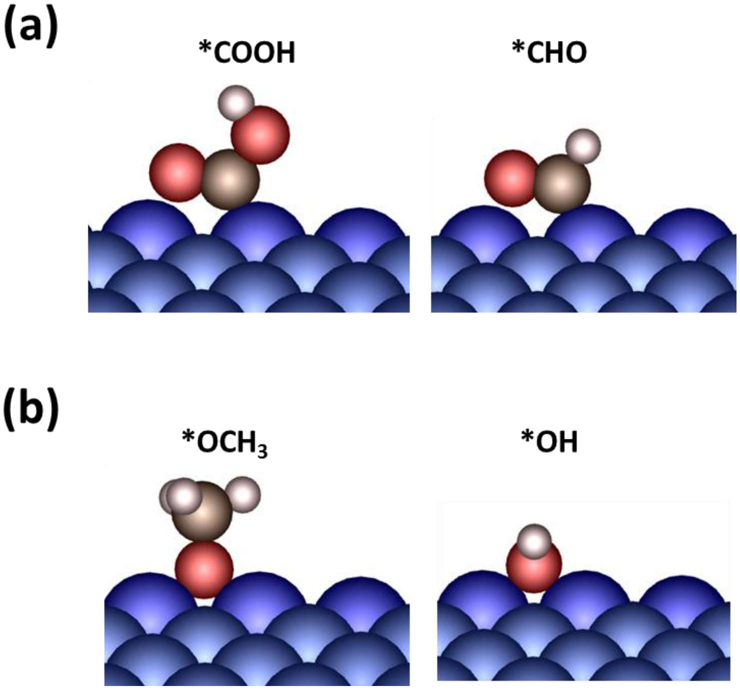

Figure 5.10 Side view of the most stable binding configurations of (a) *COOH and *CHO and (b) *OCH_3 and *OH on Cu(211).

Volcano Plot for CO_2 Reduction to Methane. Through the scaling relations and the computational hydrogen electrode model (CHE, see details in Chapter 3.4.2), the limiting potentials for each of the elementary steps can be estimated for every surface as a function of that surface's affinity for CO and OH. As illustrated in Figure 5.11, the solid lines describe the limiting potentials (U_L) of each elementary protonation reaction for CO_2 reduction to methane. As U_L is the potential at which the elementary step becomes exergonic, each limiting potential gives a first-order indication of the electrical potential at which the elementary reaction begins to have an appreciable rate. The dashed line in Figure 5.11 shows the equilibrium potential (0.17 V *vs.* RHE) for the reaction. The difference between the equilibrium potential and each U_L gives a first-order estimate of the overpotential for each elementary step. Therefore, the most negative U_L line dictates the theoretical overpotential for the CO_2 reduction to methane.

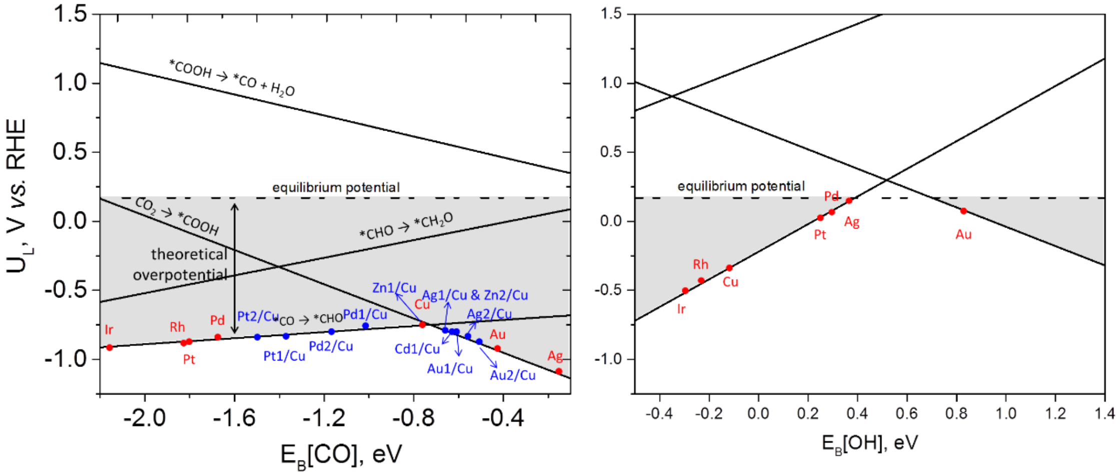

Figure 5.11 Limiting potentials (U_L) for elementary proton-transfer steps for CO_2 reduction to CH_4. Each line is the calculated potential at which the indicated elementary reaction step is neutral with respect to free energy, as a function of E_B[CO] or E_B[OH] on the surface of catalysts. The equilibrium potential for the overall electrochemical reduction of CO_2 to CH_4 is +0.17 V (vs. RHE), which is also indicated in the figure. Hence, the theoretical overpotential as a function of E_B[CO] or E_B[OH] can be represented by the distance between the equilibrium line and the most-negative limiting potential line (highlighted in gray). The elementary step of *CH_2O → *OCH_3 is excluded in this figure since it is independent to neither E_B[CO] nor E_B[OH].

The left pane of Figure 5.11 describes the limiting potentials of elementary steps that scale with E_B[CO]. According to the plots, for all the studied Cu surface alloys, the reaction will open when the elementary steps of *CO → *CHO and CO_2 → *COOH become exergonic. Similar to the data obtained by Peterson and co-workers[17], a volcano-like plot is established when the two lines of limiting potentials cross at E_B[CO] of -0.73 eV. For the present construction, Cu is the metal that stays closest (-0.75 eV) to the optimal point (the crossing point). This explains why Cu is the only metallic candidate that can selectively reduce CO_2 into methane. Moreover, the distance between the E_B[CO] of Cu and the optimal point is short, suggesting the short potential for the catalytic improvement. On the stable Cu surface alloys, Zn1/Cu interact CO with the same binding energy as Cu. Zn2/Cu and Ag1/Cu both show a E_B[CO] of 0.71 eV, implying their estimated overpotential to generate CH_4 are comparable as that of Cu. Additionally, Cd1/Cu binds CO with an energy of -0.70 eV, a point also suggesting similar overpotential as pure Cu. Meanwhile, we found that SAs of PdCu and PtCu bind CO very strongly with an energy of -1.07 eV, -1.16 eV, -1.49 eV, and -1.38 eV for Pd1/Cu, Pd2/Cu, Pt1/Cu, and Pt2/Cu, respectively, predicting quite high overpotential for CH_4 generation. On the contrary, Cu SAs having dopant of Au and large concentration of Ag bind CO too weakly (-0.67 eV for Au1/Cu, -0.54 eV for Au2/Cu, and -0.65 eV for Ag2/Cu), also suggesting poor activity for yielding CH_4. In summary, only ZnCu and low concentration SA of AgCu and CdCu exhibit proper binding affinity to the key reaction intermediate of CO, leading to decent catalytic activity for CO_2ER.

A similar plot is shown on the right-hand of Figure 5.11, which displays the limiting potentials of elementary steps that scale with E_B[OH]. Compared with the CO based intermediates, lower limiting potentials are required to make the elementary steps that involve OH based species exergonic. Based on the limiting potentials determined by E_B[OH], only the elementary step of $*OH \rightarrow * + H_2O$ requires external energy, indicating this step is an uphill step on many surfaces. According to previous report by Peterson and co-workers, the elementary steps of both $*OCH_3 \rightarrow *O + CH_4$ and $*O \rightarrow *OH$ display a downhill pathway on Cu(211), while a slight uphill path is observed on the step of $*OH \rightarrow * + H_2O$.[17]

It should be noted that the crossing point of the volcano plot in this work (-0.73 eV) varies slightly with previously reported one (-0.67 eV); the slight shift of the volcano plot is perhaps due to the inclusion of a large number of SAs as well as pure metals (18 surfaces in total) while the previous study[17] considered only 7 pure metals. Although electrocatalysts are not constrained to follow the reaction mechanism illustrated in Figure 5.11, it has been proved that this mechanism is the most economic one for CH_4 generation on Cu electrode.[18] For other mechanisms with the production of other types of hydrocarbons, there is always existence of *CO and *OH intermediates[19,20]; hence, it can be reasonably conclude that the small changes in E_B[CO] and E_B[OH] on Zn1/Cu, Zn2/Cu, Ag1/Cu, and Cd1/Cu will not alter the reduction selectivity of Cu.

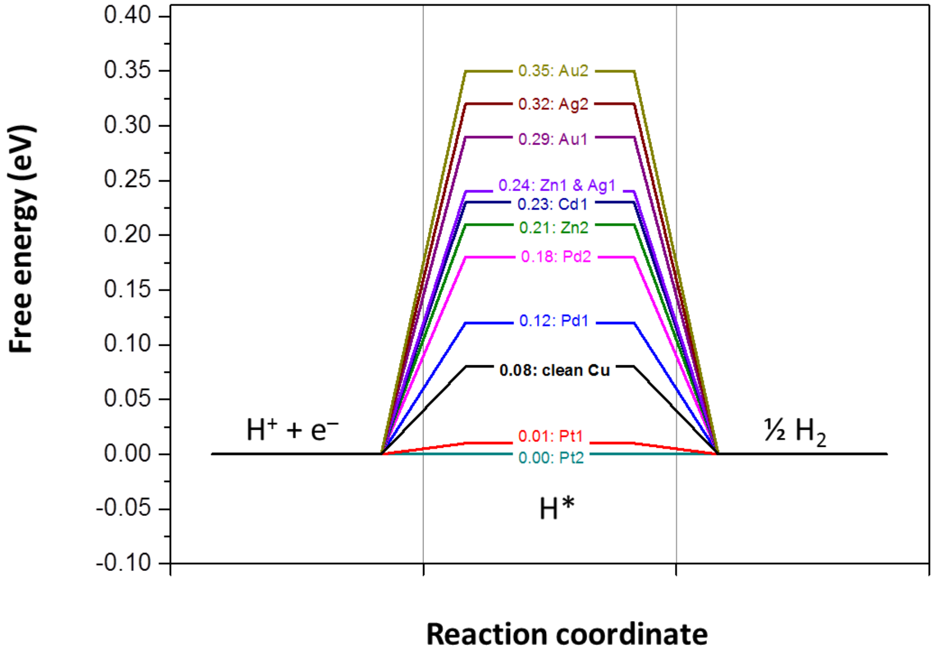

Figure 5-12 Reaction coordinate of HER on Au, Ag, Zn, Pd, Pt, and low concentration of Cd doped Cu SAs.

Performance of the Competing HER. The reaction of HER, which takes place at the same cathode surface, can inhibit the targeted CO_2ER, since HER has a less negative onset reaction potential than CO_2ER. To suppress HER and improve the Faradaic efficiency of CO_2 reduction products, the reaction overpotential of HER should be increased. To screen the HER performance, the volcano plot proposed by Nørskov and co-workers can be used.[21] In this system, an excellent HER catalyst should bind the hydrogen atom properly; either a very weak binding or a very strong binding will result in poor HER activity. In Back and co-workers' report, they suggested that rather than the strong hydrogen binding catalysts, the catalysts with weak hydrogen binding ability would be more advantageous for CO_2ER.[9] This is because if the H binds too strongly on the catalyst surface, it can occupy the active sites and reduce the available ones for CO_2ER. Moreover, as the surface coverage of H atoms increase, the H binding energy decreases, which lowers the reaction overpotential and thus enhances the HER on Cu.[21]

Hence, an ideal CO_2ER catalyst should possess relatively weak H binding to suppress the unwanted HER.

Detailed reaction coordinates of HER on the stable Cu surface alloys of AuCu, AgCu, ZnCu, PdCu, PtCu, and Cd1/Cu are shown in Figure 5.12. The ΔG_{H*} has been calculated to be 0.13 eV on pure Cu(211). For Pt-Cu surface alloys, the free energy states of chemisorbed H atom (0.01 eV for Pt1/Cu and 0.00 eV for Pt2/Cu) are quite thermal-neutral, suggesting their excellent HER activity. This is not surprising, since Pt and Pt alloys are the best known candidates for electro-chemically catalyzing HER. For dopants of Pd, Au, and Ag, an energetic rise of ΔG_{H*} is observed with the increase of dopant concentration. This is attributed to the poorer catalytic activity of these three dopant metals than metallic Cu.[21] With the increasing percentage of dopant concentration, the surface property will be more prone to the dopant metals.

As mentioned previously, a high free energy of H adsorption (weak H binding) is believed to give the electrode better performance in catalyzing CO_2 reduction, since the active sites remain uncontaminated by HER intermediate. On the edge sites of AuCu, AgCu, and ZnCu SAs, remarkable energetic enlargements (at least 0.16 eV) of the chemisorbed H state are found, in models of either low-concentration doping or high-concentration doping. Notably, in Au2/Cu system, ΔG_{H*} even reaches a value of 0.35 eV, estimating a 169% increase in reaction overpotential. The same phenomena is observed on Cd1/Cu, where a 0.23 eV (87.5% increase than Cu) of ΔG_{H*} has been calculated, implying a poor HER activity. Since the theoretical electrode potentials of hydrogen evolution in aqueous solutions is far more less than that of CO_2ER, suppressing HER in this scale is believed to help increase the Faradaic efficiency of CO_2ER products.[10]

Based on these results, we conclude doping small amount of Ag and Cd into Cu surface can lead to effective catalyst for CO_2ER, since the overpotential for hydrocarbon remains almost the same while the one for the unwanted HER is dramatically enlarged (more than 62.5%). This improves the electron transfer efficiency and thus increases the Faradaic efficiencies of CO_2 products. Moreover, for the dopant of Zn, both the small and high concentrations in Cu surface can create effective catalysis sites.

5.3.3 Energetics on ScCu, YCu, and Cd2/Cu

ScCu and YCu. When doping Sc and Y into the Cu surface, the energetics of CO_2ER intermediate change greatly due to the large lattice distortion. The scaling relations are found to be inapplicable to the SAs generated from the two dopants, neither to the low concentration model, nor to the high concentration one. The reaction pathway for CO_2 reduction to CH_4 on SAs of ScCu and YCu is illustrated in Figure 5.13. Different from the trend observed on clean Cu, the free energy rapidly goes down to a very low level from the first elementary step ($CO_2 \rightarrow *COOH$). At the second elementary step ($*COOH \rightarrow *CO + H_2O$), a slight uphill of free energy is observed on all these four models. However, the free energy starts to go down again on the following steps and the low energy level of *OH is too low to get released from the catalyst surface. Based on this diagram, it can be deduced that the two types of dopants cannot make the Cu SA effective in generating CH_4, since the oxygen based intermediates (*O and *OH) bind too strongly to the surfaces and hence poison them from adsorbing other intermediates. Moreover, On Sc2/Cu system, the free energy difference for the *OH species and an electron-proton pair to generate H_2O can be as high as 2.92 eV, estimating a -2.92 V (*vs.* RHE) onset potential to make it happen.

The competing HER on the above four models has also been computed (Figure 5.14). Similar to the trend observed in CH_4 pathway, lowered free energy states for *H are found on all the four surfaces. This is supported by the *d*-band center theory, which states that the trend of energetics for adsorbates on different surfaces should be the same as the *d*-band level of the surface atom determines the binding affinity of the surface model.[22] On the low doping concentration models (Sc1/Cu and Y1/Cu), the ΔG_{H*} is calculated to be -0.16 eV and -0.27 eV, respectively. These values suggest poor HER abilities, and estimat at least two-order higher overpotentials than the clean Cu, where ΔG_{H*} turns out to be 0.08 eV. For the high doping concentration models, the HER activities are even worse. The estimated overpotentials for Sc2/Cu and Y2/Cu are 0.84 V and 0.85 V (*vs.* RHE), respectively. For HER, catalysts with these overpotentials (more than 0.8 V *vs.* RHE) are considered as no activity. Therefore, it can be concluded that high concentration of Sc and Y in Cu surfaces can dramatically decrease the catalytic activity towards HER.

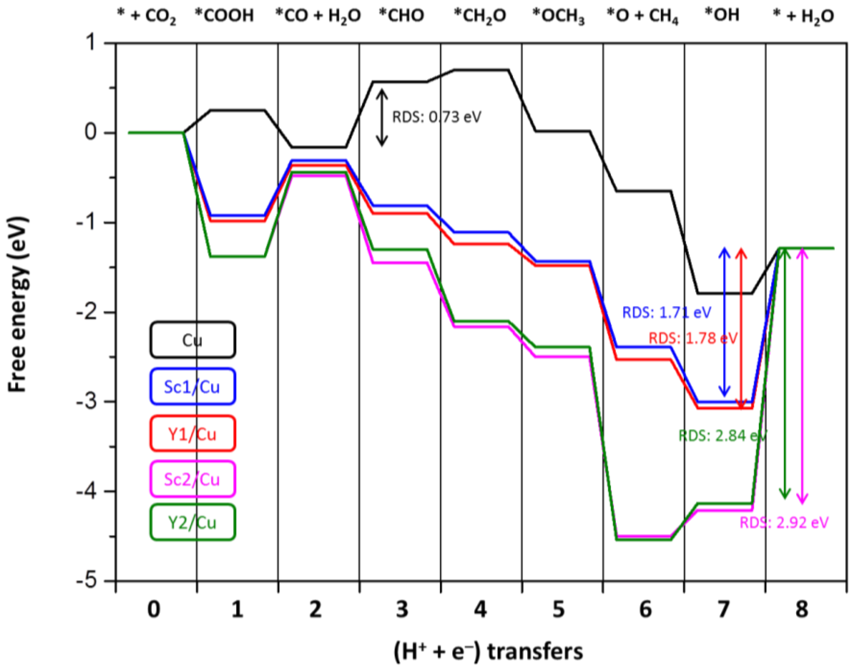

Figure 5.13 Reaction diagram of CO_2 reduction to CH_4 on Sc and Y doped Cu SAs.

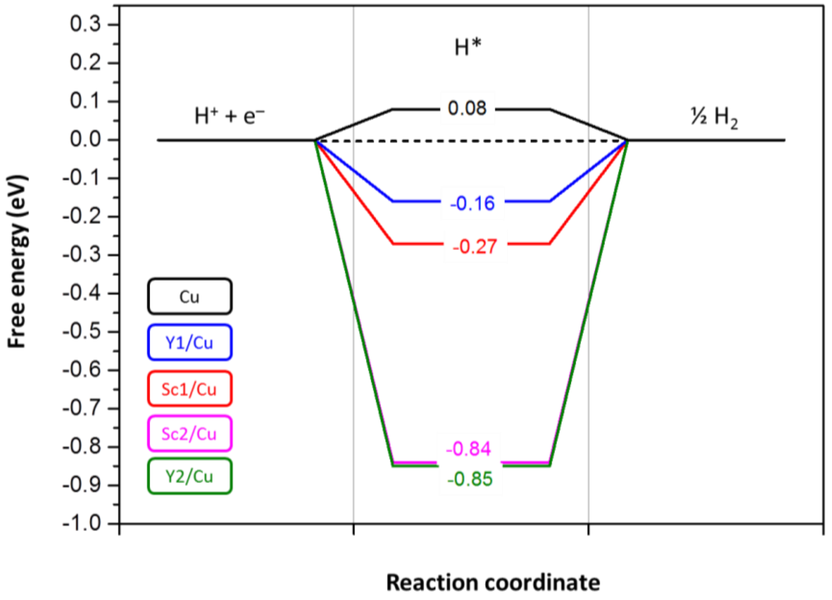

Figure 5.14 Reaction coordinate of HER on Sc and Y doped Cu SAs.

Combining the CO_2ER and HER results, the SAs of ScCu and YCu are considered as chemically inert for both reactions. One important observation from ScCu and YCu is that the binding energies of the reaction intermediates do not scale with each other. To find out the intrinsic reason for this disproportion, the configurations of *COOH on ZnCu and YCu are compared (Figure 5.15). According to Nørskov's work, the scaling relation works on the basis that the adsorbate interacts with the surface through only one single atom.[17,23] However, on ScCu and YCu, due to the large atomic radius of Sc and Y, the adsorbates cannot interact with the surface through only one atom. At least two atoms tightly bind to the surface, leading to extremely lowered binding energies (strong interactions). Since the binding configurations in this type do not fulfill the preconditions of the scaling relation, the observation of energetical disproportion of reaction intermediates is explained. Moreover, since the adsorbates are found to mainly interact with Sc and Y on the two types of Cu SAs, it is rational to conclude that the catalytic activity of pure Sc and Y play a decisive role in SA of ScCu and YCu. So far, to the best of our knowledge, neither of the two metals is found to be active in catalyzing CO_2ER.[10] Hence, the poor reaction performance of ScCu and YCu is further supported and explained.

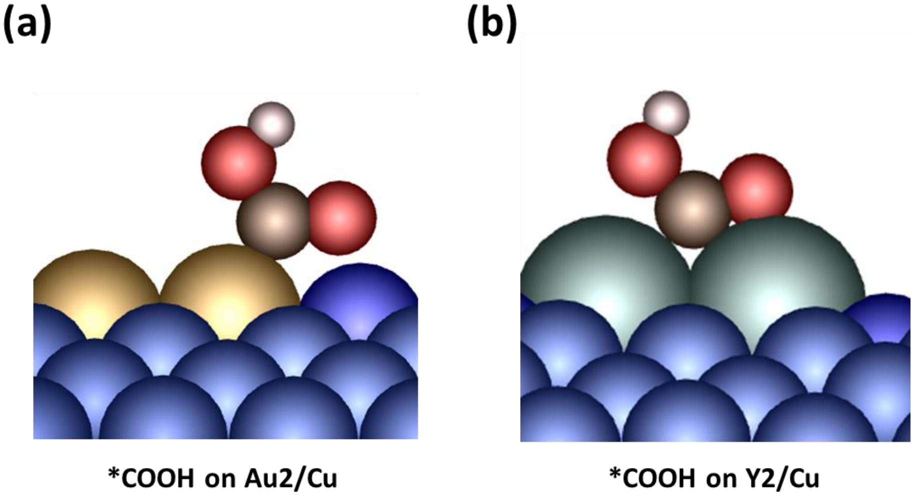

Figure 5.15 Side view of the most stable binding configurations of *COOH on (a) Au2/Cu and (b) Y2/Cu.

Cd2/Cu. For the low doping concentration model (Cd1/Cu), the energetics of Cu is not significantly changed and the scaling relations are found to be applicable. Hence, its catalytic performance is summarized in the previous sections of this chapter. On Cd2/Cu model, reaction selectivity of CO_2ER is found to be very different from Cd1/Cu. It has been noticed that one important reaction intermediate, *CO, cannot be captured by Cd2/Cu. Since formation of CH_4 must go through a *CO state[18], the failure of CO adsorption onto the Cd-Cd-Cu edge may prevent this surface from generating CH_4. Alternatively, the states of *COOH and *OCHO are observed to be stable on Cd2/Cu, leading to a selectivity towards HCOOH. From the reaction diagram in Figure 5.16, a 0.90 eV gap needs to be overcame to produce HCOOH through a *COOH intermediate. However, the gap is reduce to 0.31 eV if the reaction goes through a *OCHO intermediate, estimating a 0.31 V (*vs.* RHE) onset potential. Moreover, the computed free energy of *H is 0.50 eV, predicting an overpotential of 0.50 V (*vs.* RHE) for the competing HER. Since HER is considered to be active at 0.08 V (*vs.* RHE) on clean Cu, the overpotential is enlarged by 0.42 V on Cd2/Cu. Noting that 0.50 V is higher than 0.31 V, HER will not suppress the catalytic activity of Cd2/Cu in generating HCOOH from CO_2.

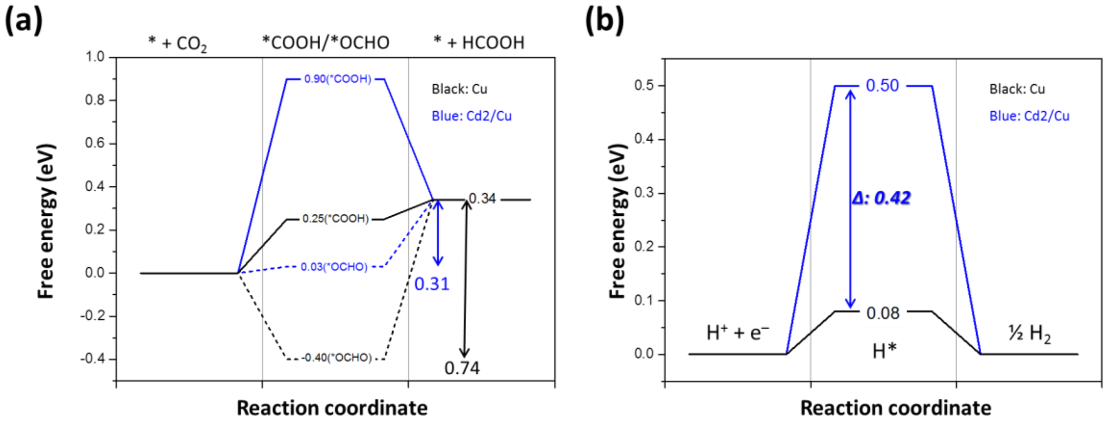

Figure 5.16 Reaction diagrams of (a) CO_2 reduction to HCOOH and (b) HER on Cd2/Cu.

According to Hori's work, pure Cd metal can selectively catalyze CO_2 into HCOOH, with a Faradaic efficiency of 78.4%.[10] Moreover, reported by Jovanov and coworkers, HCOOH is the major reduction product when using AuCd alloy as the catalyst for CO_2ER.[24] Considering a Cd-Cd bond is created on the Cd2/Cu model, we attribute the unique reaction selectivity of HCOOH to the interaction between the *COOH / *OCHO intermediate and the adjacently located Cd atoms. On the Cd2/Cu model CO_2 is selectively reduced into HCOOH and the generation of hydrocarbons is suppressed due to the presence of Cd-Cd-Cu bond.

5.4 Conclusions

Doping for surface alloy formation has been long proved to be effective in creating active local catalytic sites. By doping In into the lattice of Cu, Takanabe and coworkers found the In-Cu bimetallic surface can selectively catalyze CO_2 into CO with a much lower overpotential than 0D Cu particles.[25] Ever since that, systems of Sn[26], Co[27], Pt[28], and Ni[28] doped Cu systems have been studied to modify the selectivity of Cu electrode. Though doped Cu has been proved to be efficient for CO_2ER, there is no guidelines to provide useful predictions for the catalytic activity of a given system, given the numerous available dopant candidates. Hence, in this work, by performing a high-throughput screening study, the CO_2ER nature of twenty-nine transition metal doped Cu systems have been revealed. All these selected dopants are commonly used ones and have been employed in plenty of catalysis reactions. As doping is a straightforward and easily-controlled approach, it is believed that this work is of significant importance to help design new promising surface alloyed Cu catalyst for enhanced CO_2ER.

In summary, to screen a suitable Cu SA system with enhanced catalytic activity for CO_2ER, we employed DFT calculations to calculate the energetics of the reaction performance on various transition metal doped Cu SAs. The results are concluded as follows:

(1) The stability results show only eight transition metals (Cd, Au, Ag, Sc, Zn, Pd, Pt, and Y) can stably alloy Cu at the topmost layer. Although other metals may also alloy Cu at the surface when driven by external energy input under experimental conditions, the thermal spontaneity of these candidates can make it much easier for them to form surface alloys on Cu substrate.

(2) When doping small amount of Ag, Cd and random amount of Zn into the Cu surface, the reaction overpotentials for CH_4 are calculated to remain almost the same as that on pure Cu. By contrast, the overpotentials for the competing HER is dramatically increased. Hence, SAs in these types are considered to be able to increase the Faradaic efficiencies of hydrocarbon products.

(3) All the reaction intermediates are found to bind too strongly on ScCu and YCu. Hence, Dopants of Sc and Y result in completely no catalytic activity towards CO_2ER.

(4) When doping high concentration of Cd into Cu surface, the created Cd-Cd bonding environment will effectively catalyze CO_2 into HCOOH. The Cd2/Cu catalyst exhibits several advantages for HCOOH production comparing to Cu: (i) it has lower onset potential for HCOOH formation (0.31 V *vs*. RHE), (ii) it cannot adsorb*CO species and hence prevent the generation of hydrocarbons, (iii) it efficiently suppresses the unwanted HER.

References

1 Calle-Vallejo, F., Koper, M. T. & Bandarenka, A. S. Tailoring the catalytic activity of electrodes with monolayer amounts of foreign metals. *Chemical Society Reviews* **42**, 5210-5230 (2013).

2 Zhu, S. & Shao, M. Surface structure and composition effects on electrochemical reduction of carbon dioxide. *Journal of Solid State Electrochemistry* **20**, 861-873 (2016).

3 Kortlever, R., Peters, I., Koper, S. & Koper, M. T. Electrochemical CO2 reduction to formic acid at low overpotential and with high faradaic efficiency on carbon-supported bimetallic Pd–Pt nanoparticles. *ACS Catalysis* **5**, 3916-3923 (2015).

4 Rasul, S. *et al.* A Highly Selective Copper–Indium Bimetallic Electrocatalyst for the Electrochemical Reduction of Aqueous CO_2 to CO. *Angewandte Chemie International Edition* **54**, 2146-2150 (2015).

5 Varela, A. S. *et al.* CO2 electroreduction on well-defined bimetallic surfaces: Cu overlayers on Pt (111) and Pt (211). *The Journal of Physical Chemistry C* **117**, 20500-20508 (2013).

6 Luc, W. *et al.* Ag–Sn Bimetallic Catalyst with a Core–Shell Structure for CO_2 Reduction. *Journal of the American Chemical Society* **139**, 1885-1893 (2017).

7 Hirunsit, P., Soodsawang, W. & Limtrakul, J. CO2 electrochemical reduction to methane and methanol on copper-based alloys: theoretical insight. *The Journal of Physical Chemistry C* **119**, 8238-8249 (2015).

8 Hirunsit, P. Electroreduction of carbon dioxide to methane on copper, copper–silver, and copper–gold catalysts: a DFT study. *The Journal of Physical Chemistry C* **117**, 8262-8268 (2013).

9 Back, S., Kim, H. & Jung, Y. Selective heterogeneous CO_2 electroreduction to methanol. *ACS Catalysis* **5**, 965-971 (2015).

10 Hori, Y., Wakebe, H., Tsukamoto, T. & Koga, O. Electrocatalytic process of CO selectivity in electrochemical reduction of CO_2 at metal electrodes in aqueous media. *Electrochimica Acta* **39**, 1833-1839 (1994).

11 Christensen, A. *et al.* Phase diagrams for surface alloys. *Physical Review B* **56**, 5822 (1997).

12 Kresse, G. & Furthmüller, J. Efficient iterative schemes for ab initio total-energy calculations using a plane-wave basis set. *Physical Review B* **54**, 11169 (1996).

13 Blöchl, P. E. Projector augmented-wave method. *Physical Review B* **50**, 17953-17979 (1994).

14 Hammer, B., Hansen, L. B. & Nørskov, J. K. Improved adsorption energetics within density-functional theory using revised Perdew-Burke-Ernzerhof functionals. *Physical Review B* **59**, 7413-7421 (1999).

15 Monkhorst, H. J. & Pack, J. D. Special points for Brillouin-zone integrations. *Physical review B* **13**, 5188 (1976).

16 Nørskov, J. K. *et al.* Origin of the overpotential for oxygen reduction at a fuel-cell cathode. *The Journal of Physical Chemistry B* **108**, 17886-17892 (2004).

17 Peterson, A. A. & Nørskov, J. K. Activity Descriptors for CO2 Electroreduction to Methane on Transition-Metal Catalysts. *The Journal of Physical Chemistry Letters* **3**, 251-258 (2012).

18 Peterson, A. A., Abild-Pedersen, F., Studt, F., Rossmeisl, J. & Norskov, J. K. How copper catalyzes the electroreduction of carbon dioxide into hydrocarbon fuels. *Energy & Environmental Science* **3**, 1311-1315 (2010).

19 Nie, X., Esopi, M. R., Janik, M. J. & Asthagiri, A. Selectivity of CO2 reduction on copper electrodes: the role of the kinetics of elementary steps. *Angewandte Chemie International Edition* **52**, 2459-2462 (2013).

20 Nie, X., Luo, W., Janik, M. J. & Asthagiri, A. Reaction mechanisms of CO 2 electrochemical reduction on Cu (111) determined with density functional theory. *Journal of Catalysis* **312**, 108-122 (2014).

21 Nørskov, J. K. *et al.* Trends in the exchange current for hydrogen evolution. *Journal of The Electrochemical Society* **152**, J23-J26 (2005).

22 Hammer, B. & Nørskov, J. K. Theoretical surface science and catalysis—calculations and concepts. *Advances in Catalysis* **45**, 71-129 (2000).

23 Abild-Pedersen, F. *et al.* Scaling properties of adsorption energies for hydrogen-containing molecules on transition-metal surfaces. *Physical Review Letters* **99**, 016105 (2007).

24 Jovanov, Z. P. *et al.* Opportunities and challenges in the electrocatalysis of CO_2 and CO reduction using bifunctional surfaces: A theoretical and experimental study of Au–Cd alloys. *Journal of Catalysis* **343**, 215-231 (2016).

25 Rasul, S. *et al.* A. A Highly Selective Copper–Indium Bimetallic Electrocatalyst for the Electrochemical Reduction of Aqueous CO_2 to CO. *Angewandte Chemie* **127**, 2174-2178 (2015).

26 Sarfraz, S., Garcia-Esparza, A. T., Jedidi, A., Cavallo, L. & Takanabe, K. Cu–Sn Bimetallic Catalyst for Selective Aqueous Electroreduction of CO_2 to CO. *ACS Catalysis* **6**, 2842-2851 (2016).

27 Grote, J.-P. *et al.* Screening of material libraries for electrochemical CO_2 reduction catalysts–Improving selectivity of Cu by mixing with Co. *Journal of Catalysis* **343**, 248-256 (2016).

28 Todoroki, N., Yokota, N., Nakahata, S., Nakamura, H. & Wadayama, T. Electrochemical Reduction of CO2 on Ni-and Pt-Epitaxially Grown Cu (111) Surfaces. *Electrocatalysis* **7**, 97-103 (2016).

Chapter 6*

New Crystal Phases for Electrochemical CO_2 Reduction Reactions

This chapter explores the effect of phase transformations on the catalytic activity of metals towards CO_2ER. Since reduction of CO_2 may lead to different products on different metals, calculations have been performed on three typical metals – Cu, Au, and Pb – to represent the selectivity of hydrocarbon, CO, and HCOOH, respectively. Catalytic reactions of CO_2ER on metals in crystal symmetries of fcc, bcc, 2H, 4H, and sc have been intensively investigated. For sc symmetry, only passive metal (such as Au) in this phase is found to be stable under CO_2ER conditions; lattice rearrangement from sc to hcp is observed on active metals. For the other symmetry, a general trend of binding affinity to the CO_2ER intermediates of fcc < hcp-type (2H and 4H) < bcc is observed on all these metals, suggesting phase transformation can be an effective in targetedly tuning the catalytic activity of metals. On Au and Pb, since their original symmetry is fcc, converting the fcc phase into bcc type can result in a 25.2% and 21.3%, respectively, decreased onset potential for catalyzing CO_2ER.

*This chapter has been substantially prepared to be submitted.

6.1 Introduction

Strategies of structural and compositional modifications have been intensively investigated in order to design metal nanoparticles with fine-modified structures and components, and thus to regulate the catalytic activities. Through years' efforts, significant developments have been achieved. However, these achievements are based solely on the bulk structures of metals; the crystal orientation of the used metal candidates remains unchanged and the components in the synthesized bi- or multi-metallic particles are miscible in bulk forms. Hence, although developments have been made, strategies in these forms have an obvious limitation; that is, no matter how small the size of NP is or how many guest metals there are, the intrinsic properties of the components are still dependent on the original bulk structures.

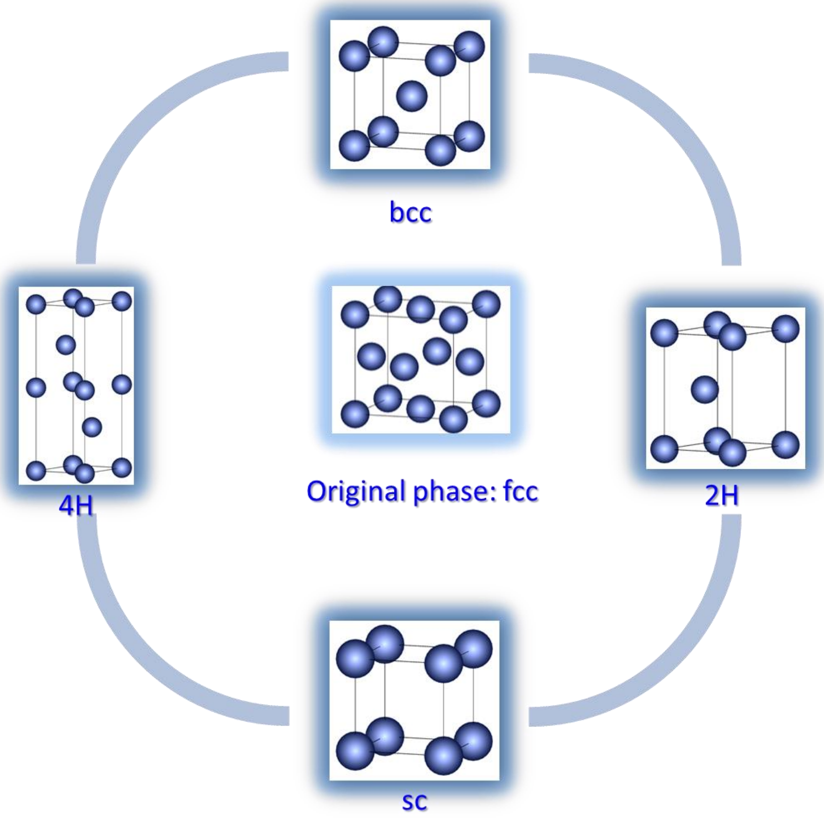

Figure 6.1 Illustration of the overall strategy of phase transformation.

Recently, it has been discovered that when the size of noble metals decreases to the scale of nanometer, the surface energy, among the systemic energy, dominates.[1] Consequently, the crystal symmetry of noble metals may rearrange and differ from their bulk counterpart.[1-5] This provides new horizons in advanced materials design by bringing in new materials in nanometer scale, whose structures are inaccessible in their original bulk states (see Figure 6.1). Notably, the functional properties of noble metals can be systematically manipulated by modifying their crystal orientations. So far, distinctive chemical stability[6,7], magnetic properties[8,9], electrical properties[10,11], and optical properties[4,12] have been reported in phase-transformed noble metal nanomaterials. However, despite the pioneer studies on the functional properties of phase-engineered noble metals, the status of catalytic behaviors for metal NPs in transformed phases still remains to be elucidated. Hence, it is of vital importance to provide a theoretical view in predicting the catalytic performances of phase-transformed metal NPs.

It would be an ideal strategy to obtain enhanced catalytic activity by manipulating the phase of metals. The catalytical sensitivity of metal nanoparticles on size, morphology, solutions, and components has been long explored. To achieve decent CO_2ER performances on metallic nanoparticles, tremendous efforts have been put on synthesizing small-sized particles[28], forming porous structures[31], employing high K^+ and Na^+ concentration[32], and introducing guest metals to create bi- and multi-metallic sites[33]. However, in all these approaches, the intrinsic crystals of metals remain since the bulk structures never change. If we move forward from the consideration that the crystal structure should be the same regardless of the particle size and morphology, controlling the synthesis of crystal phases may open a new horizon to the nanomaterials with structures that are unachievable in their bulk states. In this work, the motivation is to explore the catalytic activity of phase-engineered fcc metals towards CO_2ER.

Since the electronic structure of noble metals, which plays the key role in determining the catalytic activity, is quite sensitive to the bulk symmetry, it is hypothesized that phase-transformation can optimize the electronic structure of noble metals, thus lead to improved catalytic behavior towards CO_2 electrochemical reduction (CO_2ER). To verify this hypothesis, theoretical calculations have been performed on Cu, Au, and Pb, in various phases (fcc, 2H, 4H, bcc, and sc). These three metals are chosen to represent the three possible reduction selectivity occurred under aqueous CO_2ER conditions, Cu for hydrocarbons, Au for CO, and Pb for HCOOH (Figure 2.6). For each metal, the lattice constants in theses corresponding symmetries were first computed to establish the crystal surfaces. Following that, the energy levels of the *d*-band center for the surface atoms were calculated to provide a first-order estimate of the binding affinity towards adsorbates. The energetics of CO_2ER on these surfaces were then detailedly computed and analyzed.

6.2 Computational Details

6.2.1 Various Crystal Phases

For most transition and post-transition metals, face centered cubic (fcc), body centered cubic (bcc), and hexagonal close packed (hcp or 2H) are the normal bulk crystal phases. However, besides the already achieved synthesis of phase-transformations among these three types of symmetries[1,3,13,14], recent works have also reported the phase transformations on metal and metal alloys from fcc to simple cubic[15] (sc) and 4H[1,16]. Hence, it is believed that these five crystal phases can be converted from one to another and we thus choose all these five types of crystal phases to study the effect of phase-transformation on the catalytic activity of metals.

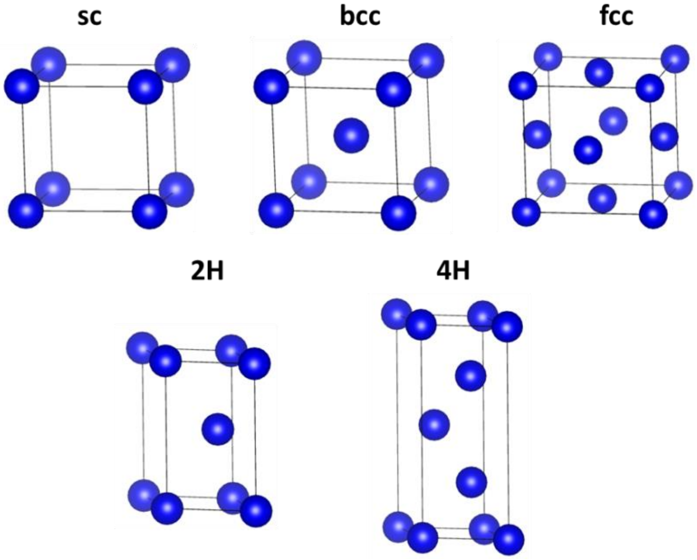

Figure 6.2 Bulk symmetries of the investigated crystal phases in this work.

The unit cells of these five kinds of crystal structures are illustrated in Figure 6.2. The phases of sc, fcc, and bcc are among the cubic system, where the unit cell is in the shape of a cube. For sc symmetry, each atom occupies one corner site of the cube and thus shares equally between eight adjacent cubes. In bcc system, one atom stays in the center of the cube and other atoms at the corners. The fcc system has six atoms on the faces of the cube, that each gives exactly one half contribution. Together with the corner atoms, this gives to a total of 4 atoms per unit cell. The 2H and 4H arrangements belong to the symmetry of hexagonal close packed, with a stacking sequence of “AB” and “ABCB” along the [001] direction, respectively. For each crystal arrangement, the most close-packed surface is chosen to represent the catalytic performance of the corresponding phase, since it always has the lowest surface energy and hence is most abundantly exposed from experimentally synthesized nanoparticles. Specifically, the (100) orientation is employed for sc phase, and the (110) for bcc, (111) for fcc, and (001) for 2H and 4H. However, two different surfaces can be exposed in $(001)_{4H}$ direction due to the “ABCB” stacking sequence (Figure 6.3). We believe the A (or C) terminated slab and the B terminated slab will result in different d-orbital structures of the surface atoms and hence different catalytic activity. Therefore, for the 4H symmetry, both the A or C terminated slab model (4H–A, C) and the B terminated one (4H–B) are taken into consideration.

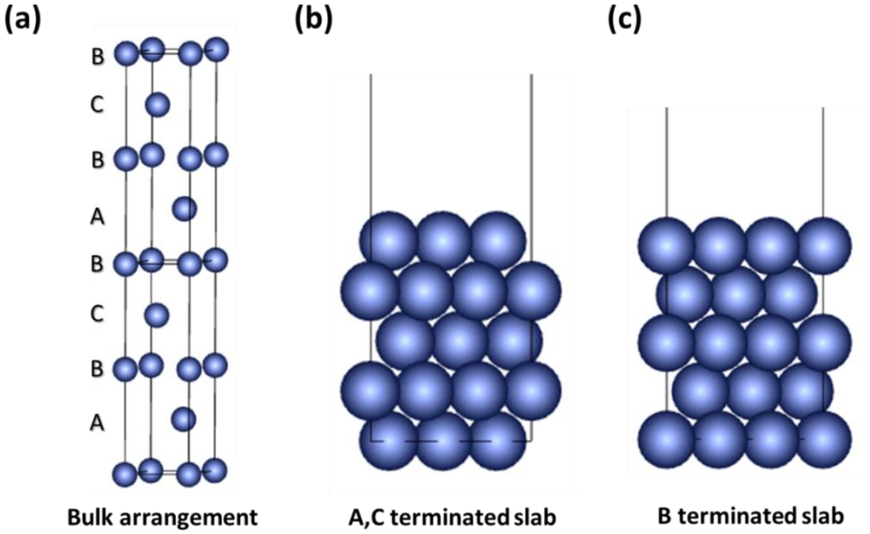

Figure 6.3 (a) Bulk arrangement of 4H phase. (b) A or C terminated slab (4H-A, C). (c) B terminated slab (4H-B).

6.2.2 Theoretical Methods

Material Models. According to Hori's work[17], four categories of metallic catalysts can be classified based on the reaction products generated in catalyzing CO_2 reduction. Specifically, Cu is the only candidate that can selectively reduce CO_2 into various hydrocarbons (CH_4, C_2H_4, CH_3OH). Metals of Au, Ag, and Zn can catalyze CO_2 into CO, with the CO efficiency of more than 79.4%. The third category of metals, including Pb, Hg, In, Sn, Cd, and Tl, can selectively reduce CO_2 into HCOOH. The last category contains Ni, Fe, Pt, and Ti, where H_2 is the main product (higher than 88.9%) under the CO_2 reduction environment. However, for the last category, since the generated H_2 gas is from solvation and no CO_2 is actually reduced during the electro-chemical process. Hence, we consider metals in this category are not active for CO_2ER and thus excluded in this study. In order to thoroughly investigate the effect of phase transformation on the catalytic activity of CO_2 reduction, we have selected three metals, Cu, Au, and Pb, representing the above mentioned three categories, to perform the theoretical calculations. Moreover, all three metals adopt a bulk fcc arrangement; since fcc is the most commonly encountered symmetry on transition and post-transition metals, we believe these fcc metals can be quite representative in providing a general trend for the phase transformation effect. Since various hydrocarbons can be generated when using Cu electrode to reduce CO_2, we choose the reduction of CO_2 to CH_4 to represent the catalytic ability of Cu. This is because CH_4 has the highest yield among all the hydrocarbon products.[17]

Computational Methods. For all the density functional theory (DFT) calculations, the projected augmented wave[18] (PAW) method was chosen to describe the ion-electron interactions under the Vienna Ab-initio Simulation Package[19] (VASP). The exchange and correlation effects were described by using the revised Perdew-Burke-Ernzerhof[20] (RPBE) functional within the generalized gradient approximation (GGA). A plane-wave cutoff energy of 500 eV was used for all the surface calculations. All the structures were fully optimized until the residual forces on each atom were less than 0.05 eV/ Å without any constraints. For all the catalyst models, a five-layer slab with 3 × 3 supercell was used.

The periodic boundary condition was employed to establish the long solid surface. To avoid the vertical interaction between the periodic images in z-direction, at least 15 Å vacuum was added in all cases. Reciprocally proportional to the surface parameters, a Monkhorst-Pack[21] grid of 3 × 3 × 1 was used to carry out the surface calculations. However, in order to achieve more detailed energy levels of d-orbitals, a 9 × 9 × 1 Monkhorst-Pack grid was adopted when computing the d-band energies. During the structure optimization, the top two layers of the slabs and the adsorbates were allowed to relax until the most stable configurations were reached, while the bottom layers were kept fixed in their bulk positions. The computational hydrogen electrode[22] (CHE) model was used to calculate the free energy of each intermediate. More detailed procedures of this model can refer to Chapter 3.

6.3 Results & Discussions

6.3.1 Phase Transformation on Cu for CO_2ER

Lattice Constant. We have first computed the lattice constants of Cu in various symmetries (Table 6.1). The calculated lattice parameter of Cu in fcc arrangement is 3.658 Å, consistent with the experimentally observed value of 3.603 Å. We note that the lattice constant of fcc Cu is reported to be 3.632 Å by Perdew-Burke-Ernzerhof (PBE) functional, which is under the same approximation type with the RPBE functional used in this work.[23] The difference between the two values is because the two functionals use different κ values in the exchange energy (0.804 for PBE while 1.245 for RPBE). Based on Nørskov’s work, the κ value in RPBE functional will result in more consistently computed interaction energy with the experimental data; but at the same time, larger values (0.5-0.75%) of lattice parameters will be achieved.[24] This explains the larger value of lattice constant for fcc Cu obtained in this work.

For bcc symmetry, the computed lattice constant is 2.928 Å, smaller than the value of fcc symmetry. This is because the number of atoms in one unit cell of bcc is smaller than that of fcc. For one fcc unit cell, there are four atoms inside, leading to a large volume of the cell. However, in bcc symmetry, only two atoms stay in one unit cell, making the cell less bulky than the fcc one. The situation is even extreme for sc symmetry, where only one atom is contained in one unit cell, leading to a lattice constant of 2.443 Å. The phase of both 2H and 4H belong to the symmetry of hexagonal close packed. Since 4H has a stacking sequence of "ABCB" in (001) direction, its c value is observed to be roughly twice higher than that on 2H phase, where the stacking sequence in (001) direction is "AB".

Table 6.1 Computed lattice constants of Cu in various crystal symmetries.

Bulk symmetry		fcc	bcc	sc	2H	4H
Lattice constant (Å)	a	3.658	2.928	2.443	2.593	2.578
	b	3.658	2.928	2.443	--	--
	c	3.658	2.928	2.443	4.254	8.476

***d*-band Structures.** In order to estimate the trend of adsorbates energetics on the surface of these symmetries, we computed the *d*-orbital structures of the surface atoms (Figure 6.4). According to the *d*-band center theory proposed by Nørskov and coworkers, a higher energy level of the *d*-band center results in a stronger adsorbate-surface interaction; while a smaller energy level will lead to a weaker one.[25] From the computed results, the surface atom of the original fcc phase displays the lowest *d* energy level value, suggesting the weakest binding activity to adsorbates. Based on Peterson's work, the catalytic activity of Cu towards CO_2ER is greatly hindered by its weak binding affinity to *CO and *CHO species.[26] Hence, to enhance the catalytic capability of Cu, strategies should be proposed to increase the interaction between the adsorbates and Cu surface (decrease the binding energy). Therefore, based on the results in Figure 6.4, all the other phases offer an estimated increase trend of the adsorbate-catalyst interaction and thus the possibility to lower the energetic gap of the rate-determining step.

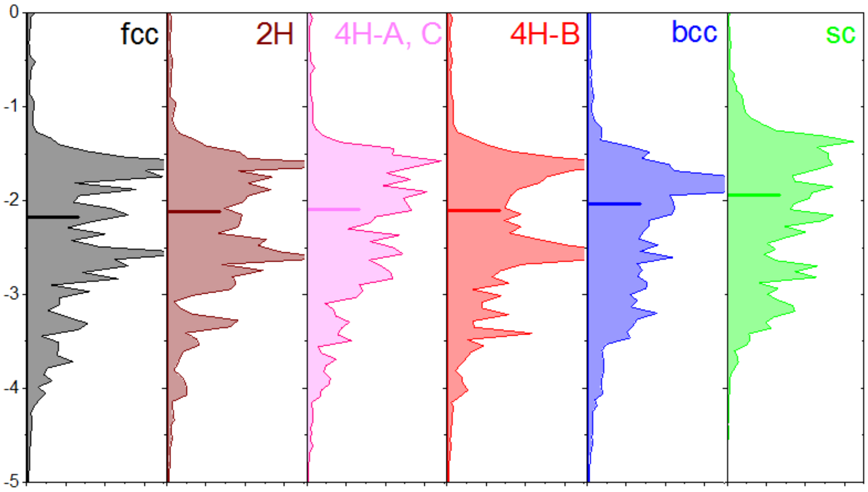

Figure 6.4 *d*-orbital density of states of Cu in various bulk symmetries.

Energetics of CO_2 Reduction to CH_4. Reduction of CO_2 on Cu electrode may lead to various hydrocarbons, among which CH_4 has the highest yield.[17] We firstly computed the reaction pathway on sc Cu, since the surface atom of sc(100) displays the highest energy level of *d*-band center (Figure 6.4). However, by computing the configuration of the first reaction intermediate on sc(100), great lattice distortion has been observed (Figure 6.5). The surface calculations have been performed by fixing the bottom three layers while relaxing the top two layers and the adsorbates. Interestingly, from the optimized geometry in Figure 6.5, we found that by adsorbing the *COOH intermediate, the arrangement of the top two Cu layers changes from simple cubic form to hexagonal close packed (hcp) form. Noting that the original stacking sequence of fcc Cu is in this hcp type, we believe this lattice change strongly suggests that sc Cu is not stable under the CO_2ER environment. Hence, sc Cu is excluded in further calculations.

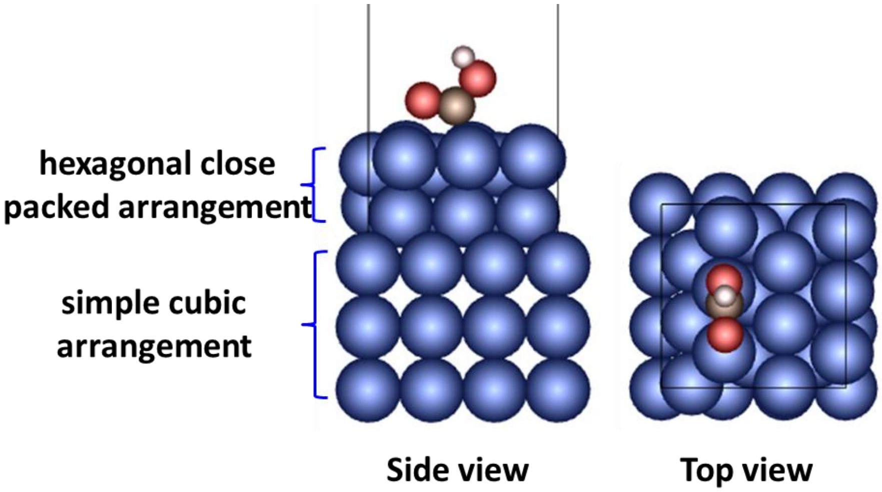

Figure 6.5 Side view and top view for the binding configuration of *COOH on sc Cu.

We then computed the reaction pathway on Cu in phases of 2H, 4H-A,C, and 4H-B, since these surfaces share the same atomic arrangement of hexagonal close packed (hcp). The binding energies of some key reaction intermediates on the three surfaces are summarized in Table 6.2. It can be seen that the energy levels are quite close (less than 0.03 eV). This is not surprising, since the *d*-band centers of the three surface atoms are quite close, ranging from -2.089 eV to -2.100 eV. Theoretically, free energy changes in this range will not result in significant difference in the prediction of reaction overpotentials. Hence, in the following comparisons of Cu phases, we take the three surfaces as one type (the hcp-type) by using the reaction energetics on 2H symmetry.

Table 6.2 Computed binding energies of the key reaction intermediates on Cu in crystal symmetries of 2H, 4H-A, C, and 4H-B. All values are given in the unit of eV.

Reaction intermediate	*COOH	*CO	*OH	*O
2H	1.51	0.91	0.17	0.83
4H-A, C	1.52	0.93	0.18	0.85
4H-B	1.51	0.91	0.16	0.82

Finally, the energetics on bcc phase and the original fcc phase were computed. The detailed comparison is illustrated in Figure 6.6. According to this reaction diagram, both the hcp type and bcc phase lower the energy levels of the reaction intermediates. Moreover, it can be seen that of these three types of crystal phases, bcc binds the reaction intermediates most strongly. This is because the surface atom of bcc(110) shows the highest *d*-band center relative to the Fermi level, and hence the strongest interaction with the adsorbates. However, the lowered energetics of reaction intermediate do not lower the gap of the rate-determining step (*CO → *CHO) on the phases of hcp type. Specifically, the free energy gap between *CO and *CHO on hcp phases (the yellow line in Figure 6.6) is 1.04 eV, slightly higher than that on fcc Cu, where a gap of 0.97 eV is observed. By contrast, a lowered gap is found on bcc Cu, where a 0.91 eV value (6.2% decrease from fcc) has been computed. This result predicts that bcc Cu can catalyze CO_2 into CH_4 with a lower overpotential than fcc Cu. However, although we find that transforming the phase of Cu into bcc type will create a more effective CO_2ER catalyst (with lowered reaction overpotential), we also notice that the scale of the enhancement is not that big (6.2% based on the free energy), implying that this strategy is not significant for Cu. This may attribute to the similar binding affinities of metal surface to the species of *CO and *CHO. Based on Nørskov's work, a linear scaling with a slope of 0.88 is found between the binding energies of *CO and *CHO on various metal surfaces.[27] This slope value indicates that a surface that stabilizes *CHO will stabilize *CO by a similar amount. Thus, the binding energies are coupled, and the relative free energy changes between these two states are only slightly different with catalyst materials.

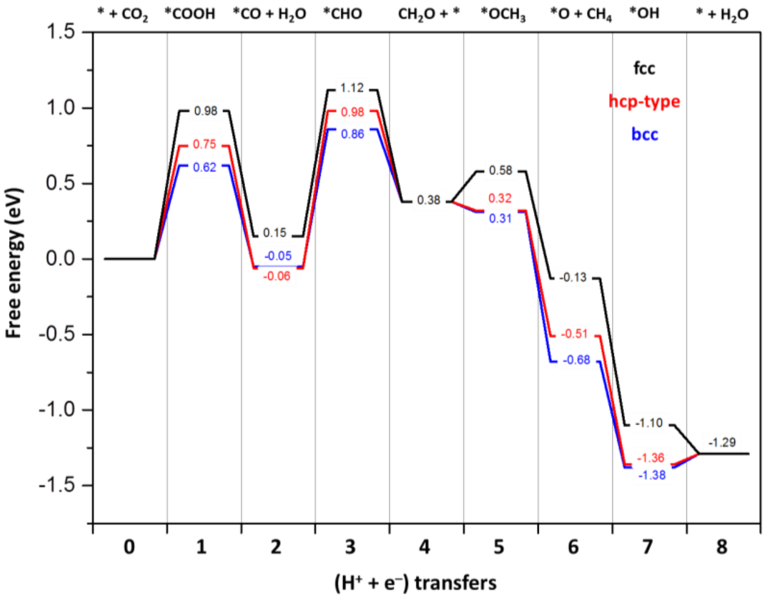

Figure 6.6 Free energy diagram of CO_2 reduction to CH_4 on Cu in crystal phases of fcc, hcp-type, and bcc.

6.3.2 Phase Transformation on Au for CO_2ER

Lattice Constant. The calculated lattice constants of Au in various crystal phases are summarized in Table 6.3. A value of 4.201 Å is obtained for the original fcc phase, consistent with the value of 4.17 Å reported by Mistry and coworkers using PBE functional.[28] The calculated lattice constants of the other two cubic symmetries, bcc and sc, are 3.340 Å and 2.771 Å, respectively. The lattice constants increases with increasing number of atoms in one unit cell, the same trend as has been observed for Cu. The lattice constants of 4H are calculated to be 2.933 Å and 9.597 Å for *a* and *c*, respectively. They are consistent with the simulated cell in other reported works, where *a* and *c* equal to 2.866 Å and 9.662 Å, respectively.[4] The slight difference may result from the different code and computational parameters set during the calculations.

Table 6.3 Computed lattice constants of Au in various crystal symmetries.

Bulk symmetry		fcc	bcc	sc	2H	4H
Lattice constant (Å)	a	4.201	3.340	2.771	2.950	2.933
	b	4.201	3.340	2.771	--	--
	c	4.201	3.340	2.771	5.072	9.597

***d*-band Structures.** Similar to the trend observed on Cu, the original Au (fcc) phase displays the lowest energy level of *d*-band center (Figure 6.7), with a value of -3.107 eV. The values on other phases are all closer to 0 than that on fcc Au, suggesting all the changed crystal phases can lower the energetics of adsorbates adsorption. Based on the mechanism of CO_2 reduction to CO on Au surfaces, the rate-limiting step is the hydrogenation of molecular CO_2 ($CO_2 \rightarrow$ *COOH). Since this step is the first elementary step of the reaction, it is believed that lowered energetics will be of great significance in decreasing the estimated theoretical overpotential.

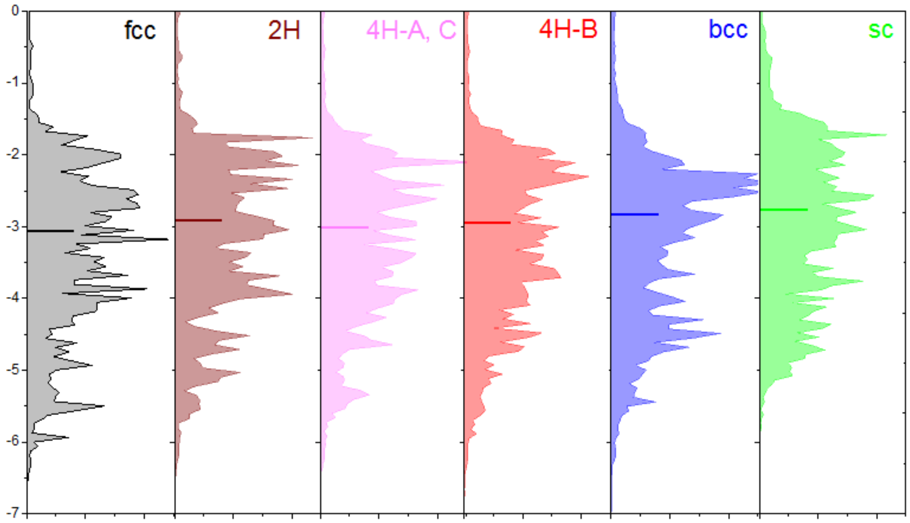

Figure 6.7 *d*-orbital density of states of Au in various bulk symmetries.

Energetics of CO_2 Reduction to CO. From the energetics results on Cu, crystal surfaces of 2H, 4H-A, C, and 4H-B show almost the same energy levels (less than 0.03 eV) for the key reaction intermediates. Hence, on Au phases, we firstly computed the energetics on these three surfaces (Table 6.4). According to the mechanism of CO_2 reduction to CO, only two types of intermediates are involved, *COOH and *CO. Based on the obtained results, 4H-A, C and 4H-B show almost the same energetics of the reaction states (the difference is less than 0.01 eV), while 2H shows slightly different ones from the two 4H surfaces (the difference is more than 0.08 eV). This is because the two 4H surfaces display quite comparable values of *d*-band center (-2.988 eV for 4H-B, -3.002 eV for 4H-A, C); while a smaller value of -2.967 eV is obtained for 2H. Therefore, considering the close energetics on the two 4H surfaces, on the following comparisons, we use the energetics on 4H-B to represent the 4H phase.

Table 6.4 Computed binding energies of the reaction intermediates on Au in crystal symmetries of 2H, 4H-A, C, and 4H-B. All values are given in the unit of eV.

Reaction intermediate	*COOH	*CO
2H	1.71	1.45
4H-A, C	1.64	1.36
4H-B	1.63	1.36

Reaction diagram of CO_2 reduction to CO on Au in different phases is shown in Figure 6.8. Consistent with the trend obtained in *d*-band center, it is obvious that all the changed phases lower the energetics of reaction intermediate. For the rate-determining step ($CO_2 \rightarrow$ *COOH), the energetic has been lowered from 1.11 eV on fcc(111) to 0.96 eV on sc(100), 0.95 eV on 2H(001), 0.87 eV on 4H(001), and 0.83 eV on bcc(110). Notably, there is a 25.2% decrease in free energy on the bcc surface. Based on the current status of CO_2 reduction to CO on Au electrode, this scale is quite considerable.

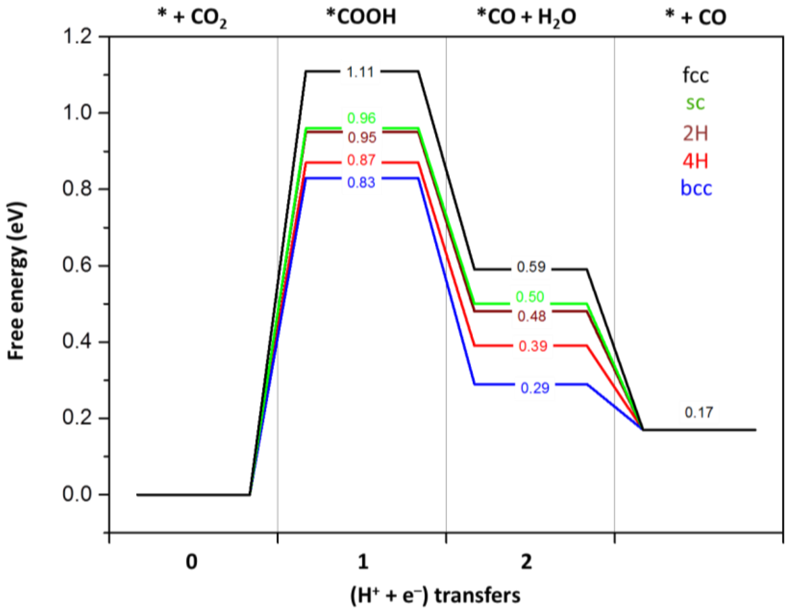

Figure 6.8 Free energy diagram of CO_2 reduction to CO on Au in crystal phases of fcc, sc, 2H, 4H and bcc.

Interestingly, one significant difference found between Au and Cu is that sc Au is quite stable under CO_2 reduction environment. From the final configurations of *COOH and *CO on sc Au (Figure 6.9), it is obvious that sc(100) of Au remains its bulk arrangement. This may attribute to the low d-band center of surface Au atom in sc phase. On sc Au, the *d*-band center of surface atom is -2.753 eV, indicating that the surface atoms are quite stable. However, on sc Cu, the *d*-band center for a surface atom is calculated to be -1.961 eV, suggesting a much stronger activity.

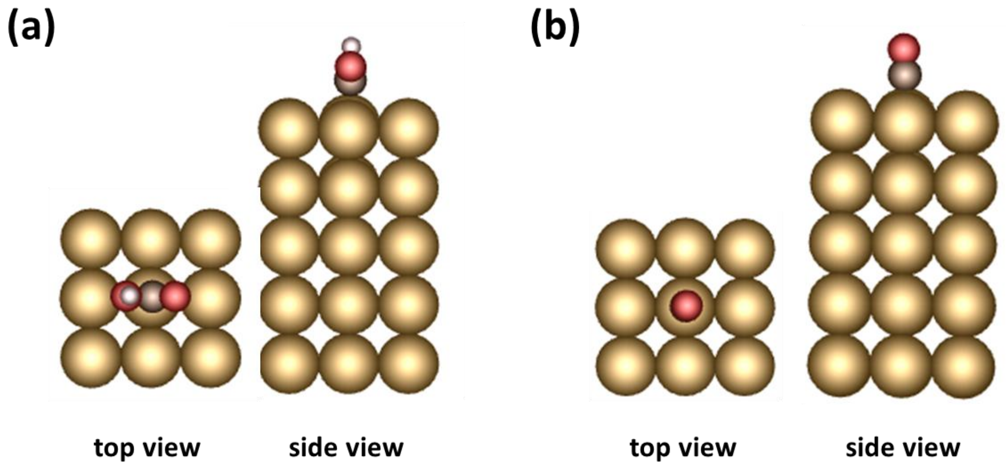

Figure 6.9 Most stable binding configurations of (a) *COOH and (b) *CO on sc(100) of Au.

6.3.3 Phase Transformation on Pb for CO_2ER

Lattice Constants. As a post-transition metal staying in the sixth period of the periodic table, Pb has a quite large lattice constant for its original fcc symmetry. The computed lattice constant of fcc Pb is 5.084 Å under RPBE functional, consistent with the reported value of 5.048 Å by PBE functional.[23] Similar to the trend generated in Cu and Au, lattice constants of the other two cubic phases of Pb are smaller than that of fcc, with 4.043 Å for bcc and 3.478 Å for sc. For the two hcp type phases, the values of *a* and *c* are calculated to be 3.522 Å and 6.059 Å for 2H and 3.544 Å and 12.091 Å for 4H.

Table 6.5 Computed lattice constants of Pb in various crystal symmetries.

Bulk symmetry		fcc	bcc	sc	2H	4H
Lattice constant (Å)	a	5.084	4.043	3.478	3.522	3.544
	b	5.084	4.043	3.478	--	--
	c	5.084	4.043	3.478	6.059	12.091

Energetics of CO_2 Reduction to HCOOH. Since the *d*-band center theory is designed to explain the binding trend on transition metals[25], we consider some assumptions may not be suitable for main group elements. Hence, the *d*-band theory is excluded here as it is believed that no useful predictions can be obtained for the energetics on Pb in different crystal phases. Reducing CO_2 into HCOOH is a two-electron reaction and involves one intermediate. Depending on which atom (C or O atom of the CO_2 molecule) the first transferred electron-proton pair will bind to, two possible types of intermediate, *COOH and *OCHO, can be generated.[29] If the first electron-proton pair interacts with the O atom, *COOH will be formed. Otherwise, *OCHO will be the intermediate (Figure 6.10).

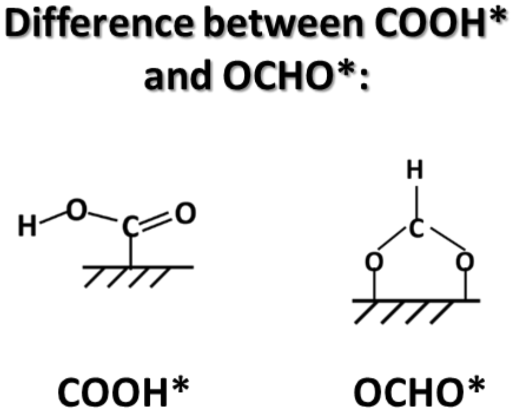

Figure 6.10 Configurational difference between the two possible intermediates: *COOH and *OCHO.

The calculated free energy states of CO_2 reduction to HCOOH on various Pb phases are summarized in Table 6.5. Similar to the phenomenon observed on Cu, sc Pb is found to be unstable under CO_2ER conditions, with large lattice distortion (from sc arrangement to hcp one) for the adsorption configurations. According to the results from Cu and Au, this is probably because the high reactivity of the electrons in surface Pb atoms. In order to verify this hypothesis, we have calculated the energy level of *d*-electrons from surface Pb atoms. The computed value is -0.450 eV, a quite high one to result in strong activities. Therefore, based on these findings, it is reasonable to conclude that active metals in sc phase are not stable under CO_2ER conditions; the necessarily occurred reaction intermediates (*COOH, *CO) will cause great distortion to the sc surfaces and thus destroy their bulk arrangements.

Energetically, the original fcc phase binds the two possible intermediates most weakly among the five studied phases, suggesting its poor catalytic activity. By contrast, the rest four surfaces all display lowered energetics of the reaction states, indicating stronger binding. Similar to the trend observed on Cu and Au, the three hcp-type surfaces (2H, 4H-A, C, and 4H-B) of Pb also show comparable energetics of the reaction states. The differences in free energy of both *COOH and *OCHO on these three surfaces are less than 0.09 eV, as can be seen from the results summarized in Table 6.6. Considering a barrier of 0.09 eV is quite surmountable at room temperature[26], we thus take the energetics on 2H(001) to represent the reaction pathway on all these three hcp-type surfaces. The bcc(110) surface shows the strongest binding affinity among the four stable surfaces, with the free energy of *COOH and *OCHO being 0.96 eV and -0.04 eV, respectively. The lowered *COOH state predicts a significant 21.3% decrease of the onset potential for the reaction going through the *COOH pathway (Figure 6.11). However, the tight binding on bcc phase may not always lead to smaller estimated potentials. From the reaction diagram in Figure 6.11, for the reaction via *OCHO intermediate, the lower free energy on bcc(110) results in a higher gap for the second elementary step, making the second elementary step the rate-determining one. These results confirm that the binding should be neither too strong nor too weak in order to have effective catalytic activity. This is consistent with the Sabatier Principle (see details in Chapter 3) in catalysis domain, which defines a good catalyst should have intermediate interactions with the key adsorbates.

Table 6.6 Computed binding energies of the reaction intermediates on Pb in crystal symmetries of fcc, bcc, 2H, 4H-A, C, and 4H-B. All values are given in the unit of eV.

Crystal phases	fcc	bcc	hcp-type		
			2H	4H-A, C	4H-B
*COOH	1.22	0.96	1.07	1.08	1.03
*OCHO	0.34	-0.04	0.11	0.17	0.08

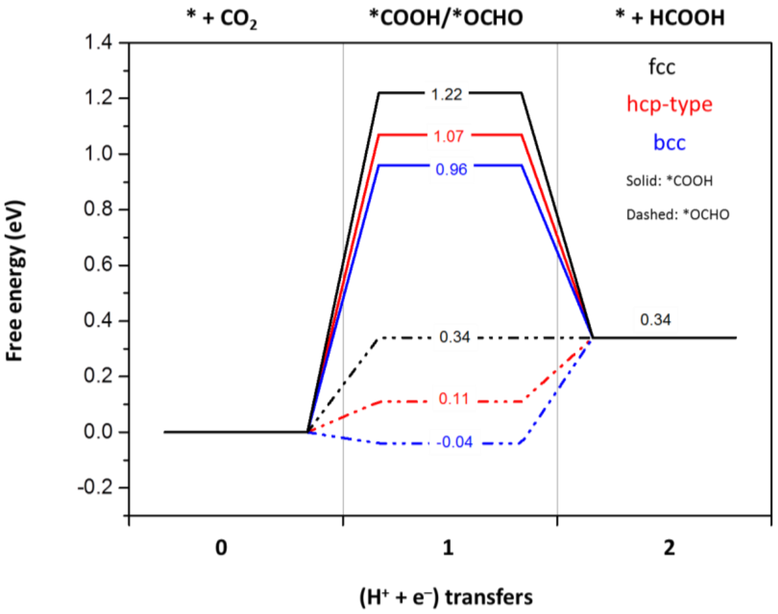

Figure 6.11 Free energy diagram of CO_2 reduction to HCOOH on Pb in crystal phases of fcc, hcp-type, and bcc.

On all these crystal orientations studied, the free energies of *OCHO species are always lower than those of *COOH. Since low free energy change correlates to low reaction potential, the reaction is likely to go through the *OCHO pathway at low driving potential. However, according to Hori's work, a 1.63 V (*vs.* NHE) potential is needed to produce a 5.0 mA/cm^2 current density on Pb electrode when catalyzing CO_2 into HCOOH.[17] The high experimental potential suggests the *COOH pathway may be dominant for the reaction. The infeasibility of the reaction going through *OCHO pathway at low potential may attribute to the competing HER, which takes place at the same cathode surface and can couple the transferred electrons at low potential range.

6.3.4 Applicability of Phase Transformation

On all these selected metals, transforming the original fcc surfaces into other symmetries (2H, 4H, and bcc) lowers the free energy states of the reaction intermediates in CO_2ER, with bcc symmetry providing the lowest theoretical reaction potential. The binding affinities of metals with different phases towards the reaction intermediates follow the trend of fcc < hcp-type < bcc. The symmetry of sc is found to be only stable on very passive metals (Au in this work) and thus considered to be less significant for designing effective electro-catalysts. The higher energy level of *d* electrons gives the electronic insight of the binding affinity of bcc surface. Apparently, transferring crystal phase of metals into bcc orientation can be an effective strategy in designing CO_2ER catalyst with lowered reaction overpotential. However, whether this strategy can be applied to all metal electrodes still needs more detailed study.

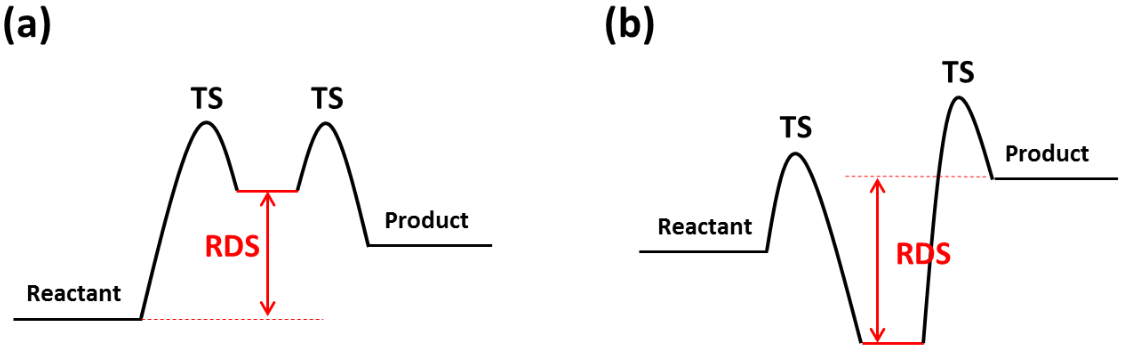

Figure 6.12 Two possible cases for the rate-determining step (RDS): (a) weak adsorption and (b) strong adsorption for the key intermediate.

Catalytically, the RDS can occur in two possible cases: the adsorption-determined process or the desorption-determined one (Figure 6.12). Based on the results achieved in this work, changing the fcc orientation into bcc type can create higher d-band level, and thus lower binding energies for adsorbates. This is of great significance to decrease the barrier for the adsorption-determined process (Figure 6.12 (a)), since, according to the BEP relation (see details in Chapter 3), a lowered state of the adsorbate-catalyst system will result in a lowered reaction barrier. In the domain of CO_2ER, as far as our concern, the catalytic performance of most metals are hindered by the high energy state of the key intermediate. Among all the typical metallic electrodes (those reported by Hori in Figure), only Pd is found to bind the reaction intermediates too strongly.[30] Moreover, so far, since most of the commonly used metals in CO_2ER are noble metals (Cu, Ag, Au) in fcc type, this strategy may open a new approach for designing very promising catalysts.

However, things will be quite different on desorption-determined RDS (Figure 6.12 (b)). Because the energy states of reactant and product cannot be changed, the only method to lower the activation barrier of RDS is to increase the state of the corresponding intermediate. Hence, changing the fcc symmetry into bcc can play a rather negative role in this case. Then, metals in bcc or hcp phases will be advantageous, since converting the phase into fcc may increase the energy level of the key reaction intermediates and thus display better catalytic activity. For metals in hcp phase, they may benefit greatly from the strategy of phase transformation, as they may either change to fcc to create higher energetics or transform to bcc to produce lower ones. In other words, the strategy of phase transformation can be applied to a wide range of metals in designing effective electro-catalysts towards CO_2ER. Moreover, this finding may also provide guidance for effective design of electro-catalysts in other surface reactions, where the energetics of key intermediates plays the dominant role in determining the catalytic activity.

6.4 Conclusions

To evaluate the strategy of phase transformation in designing good metallic catalyst for CO_2ER, we have systematically studied the catalytic performance of Cu (with selectivity of hydrocarbons), Au (with selectivity of CO), and Pb (with selectivity of HCOOH) in various crystal symmetries (fcc, 2H, 4H, bcc, and sc). By analyzing the obtained computational results, following conclusions are reached.

(1) Under CO_2ER conditions, the crystal phase of sc is found to be stable only on passive metals (Au in this study). Transformation of atomic arrangement from sc to hcp is observed by the adsorption of *COOH on less passive metals. Thus, it is concluded that metals in sc phase cannot work durably as electro-catalyst for CO_2ER.

(2) For metals in different crystal symmetries, their binding affinities for adsorbates follow the trend of fcc < hcp-type < bcc. Energetically, this trend provides useful guidance in manipulating the energy state for the key reaction intermediates and thus helps design new effective electro-catalyst.

(3) For metal of Cu, Au, and Pb, we found that converting its original fcc phase into bcc type can decrease the energy gap of the rate-determining step, which predicts lower

reaction potentials. On Au and Pb, the estimated onset potentials for CO_2ER are lowered by 25.2% and 21.3%, respectively, suggesting effective catalytic enhancement.

References

1 Liu, X., Luo, J. & Zhu, J. Size effect on the crystal structure of silver nanowires. *Nano Letters* **6**, 408-412 (2006).

2 Kondo, Y. & Takayanagi, K. Gold nanobridge stabilized by surface structure. *Physical Review Letters* **79**, 3455 (1997).

3 Huang, X. *et al.* Synthesis of hexagonal close-packed gold nanostructures. *Nature Communications* **2**, 292 (2011).

4 Fan, Z. *et al.* Stabilization of 4H hexagonal phase in gold nanoribbons. *Nature Communications* **6** 7684 (2015).

5 Chakraborty, I. *et al.* Novel hexagonal polytypes of silver: growth, characterization and first-principles calculations. *Journal of Physics: Condensed Matter* **23**, 325401 (2011).

6 Li, Q. *et al.* New approach to fully ordered fct-FePt nanoparticles for much enhanced electrocatalysis in acid. *Nano Letters* **15**, 2468-2473 (2015).

7 Zhang, S., Guo, S., Zhu, H., Su, D. & Sun, S. Structure-induced enhancement in electrooxidation of trimetallic FePtAu nanoparticles. *Journal of the American Chemical Society* **134**, 5060-5063 (2012).

8 Kim, J., Rong, C., Lee, Y., Liu, J. P. & Sun, S. From core/shell structured FePt/Fe3O4/MgO to ferromagnetic FePt nanoparticles. *Chemistry of Materials* **20**, 7242-7245 (2008).

9 Chen, H. M. *et al.* Ferromagnetic CoPt3 nanowires: structural evolution from fcc to ordered L12. *Journal of the American Chemical Society* **131**, 15794-15801 (2009).

10 Singh, A., Sai, T. P. & Ghosh, A. Electrochemical fabrication of ultralow noise metallic nanowires with hcp crystalline lattice. *Applied Physics Letters* **93**, 102107 (2008).

11 Liu, X. *et al.* In situ electrical measurements of polytypic silver nanowires. *Nanotechnology* **19**, 085711 (2008).

12 Chakraborty, I., Shirodkar, S. N., Gohil, S., Waghmare, U. V. & Ayyub, P. A stable, quasi-2D modification of silver: optical, electronic, vibrational and mechanical properties, and first principles calculations. *Journal of Physics: Condensed Matter* **26**, 025402 (2013).

13 Kusada, K. *et al.* Discovery of face-centered-cubic ruthenium nanoparticles: facile size-controlled synthesis using the chemical reduction method. *Journal of the American Chemical Society* **135**, 5493-5496 (2013).

14 Fan, Z. *et al.* Surface modification-induced phase transformation of hexagonal close-packed gold square sheets. *Nature Communications* **6**, 6571 (2015).

15 Wang, D. *et al.* Structurally ordered intermetallic platinum–cobalt core–shell nanoparticles with enhanced activity and stability as oxygen reduction electrocatalysts. *Nature Materials* **12**, 81-87 (2013).

16 Luo, J., Zhang, L., Zhang, Y. & Zhu, J. Controlled Growth of One Dimensional Metal–Semiconductor and Metal–Carbon Nanotube Heterojunctions. *Advanced Materials* **14**, 1413-1414 (2002).

17 Hori, Y., Wakebe, H., Tsukamoto, T. & Koga, O. Electrocatalytic process of CO selectivity in electrochemical reduction of CO2 at metal electrodes in aqueous media. *Electrochimica Acta* **39**, 1833-1839 (1994).

18 Kresse, G. & Joubert, D. From ultrasoft pseudopotentials to the projector augmented-wave method. *Physical Review B* **59**, 1758 (1999).

19 Kresse, G. & Furthmüller, J. Efficient iterative schemes for ab initio total-energy calculations using a plane-wave basis set. *Physical Review B* **54**, 11169 (1996).

20 Zhang, Y. & Yang, W. Comment on "Generalized gradient approximation made simple". *Physical Review Letters* **80**, 890 (1998).

21 Monkhorst, H. J. & Pack, J. D. Special points for Brillouin-zone integrations. *Physical Review B* **13**, 5188 (1976).

22 Nørskov, J. K. *et al.* Origin of the overpotential for oxygen reduction at a fuel-cell cathode. *The Journal of Physical Chemistry B* **108**, 17886-17892 (2004).

23 Haas, P., Tran, F. & Blaha, P. Calculation of the lattice constant of solids with semilocal functionals. *Physical Review B* **79**, 085104 (2009).

24 Hammer, B., Hansen, L. B. & Nørskov, J. K. Improved adsorption energetics within density-functional theory using revised Perdew-Burke-Ernzerhof functionals. *Physical Review B* **59**, 7413 (1999).

25 Hammer, B. & Nørskov, J. K. Theoretical surface science and catalysis—calculations and concepts. *Advances in Catalysis* **45**, 71-129 (2000).

26 Peterson, A. A., Abild-Pedersen, F., Studt, F., Rossmeisl, J. & Norskov, J. K. How copper catalyzes the electroreduction of carbon dioxide into hydrocarbon fuels. *Energy & Environmental Science* **3**, 1311-1315 (2010).

27 Peterson, A. A. & Nørskov, J. K. Activity Descriptors for CO_2 Electroreduction to Methane on Transition-Metal Catalysts. *The Journal of Physical Chemistry Letters* **3**, 251-258 (2012).

28 Mistry, H. *et al.* Exceptional size-dependent activity enhancement in the electroreduction of CO_2 over Au nanoparticles. *Journal of the American Chemical Society* **136**, 16473-16476 (2014).

29 Durand, W. J., Peterson, A. A., Studt, F., Abild-Pedersen, F. & Nørskov, J. K. Structure effects on the energetics of the electrochemical reduction of CO_2 by copper surfaces. *Surface Science* **605**, 1354-1359 (2011).

30 Gao, D. *et al.* Size-dependent electrocatalytic reduction of CO_2 over Pd nanoparticles. *Journal of the American Chemical Society* **137**, 4288-4291 (2015).

31 Rosen, J. *et al.* Mechanistic insights into the electrochemical reduction of CO_2 to CO on nanostructured Ag surfaces. *ACS Catalysis* **5**, 4293-4299 (2015).

32 Liu, M. *et al.* Enhanced electrocatalytic CO_2 reduction via field-induced reagent concentration. *Nature* **537**, 382-386 (2016).

33 Torelli, D. A. *et al.* Nickel–Gallium-Catalyzed Electrochemical Reduction of CO_2 to Highly Reduced Products at Low Overpotentials. *ACS Catalysis* **6**, 2100-2104 (2016).

Chapter 7

Summary and Future Work

This chapter summarizes the entire project as a whole. Based on the obtained computational results, the three hypotheses have been deeply addressed and demonstrated one by one. The generated data in this thesis also provide significant guidance in future designs of effective electro-catalysts for CO_2*ER. Combining the results obtained in this thesis and from reported works, strategies are proposed for future work, such as constructing surface alloy systems using Au and Ag substrates, designing core-shell models to take advantage of the strain effect, and doping various transition metals into the surface of inert 2D materials. These strategies should be able to help design effective* CO_2*ER catalysts and the computational predictions based on these models will provide useful guidance in directing experimental synthesis.*

7.1 Summary

This study aims to rationally design effective metallic electro-catalysts for advanced CO_2ER performance. By taking advantage of computational tools, energetic calculations have been performed to verify the three hypotheses (Figure 7.1) proposed in Chapter 1. Firstly, we have explored the catalytic behaviors of low-coordinated (defective) atomic sites on Cu NPs. Secondly, by employing the scaling relations and computational hydrogen electrode (CHE) model, we have screened the CO_2ER activity of Cu surface alloys (SAs) doped by transition metals. Finally, by computing the energetic pathway of CO_2ER on Cu, Au, and Pb in various crystal phases (fcc, bcc, sc, hcp, and 4H), we have demonstrated that phase transformation can be an effective strategy in designing metallic NPs with advanced catalytic performance for electrochemical reactions.

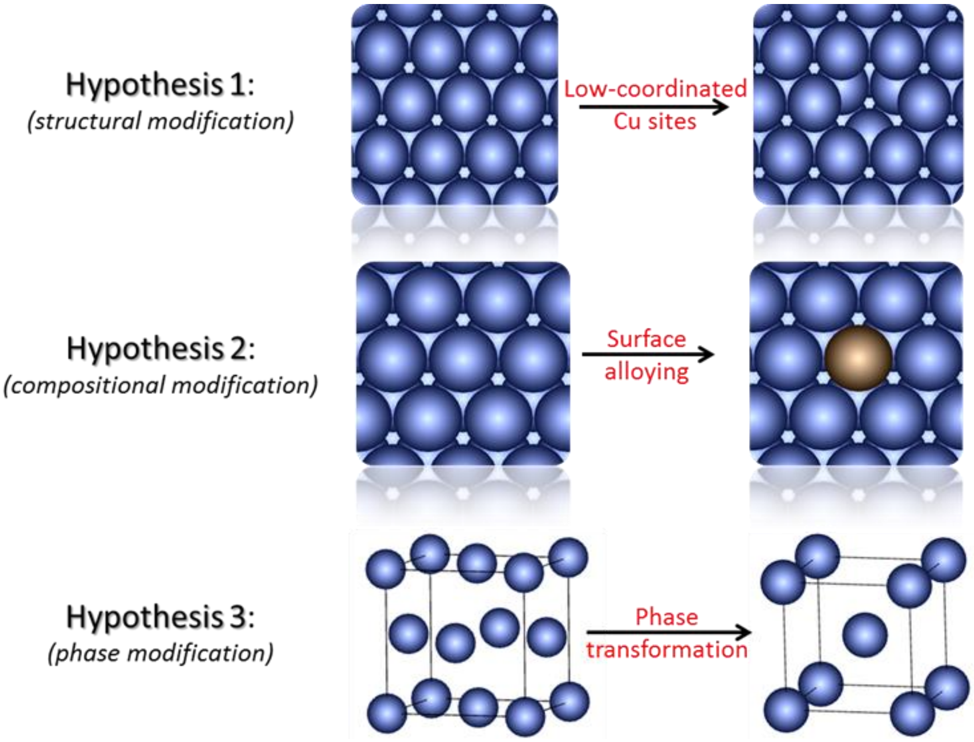

Figure 7.1 Three hypotheses proposed in this work for improving the catalytic activity of metal NPs.

The first hypothesis proposed in this study is that the various low-coordinated atomic sites on metal NPs can catalyze CO_2ER with lowered reaction overpotentials than the full-coordinated ones. To verify this hypothesis, four different low-coordinated Cu sites –

(100) for the plain atoms, (211) for the edge atoms, (532) for the corner atoms, and vac-(111) for the atoms around the surface vacancy – have been simulated (see Figure 4.2). Energetics of CO_2ER and the competing HER were calculated on the above mentioned low-coordinated sites and the full-coordinated (111) site. We found that for all the possible reactions of CO_2ER, lowered energetic gaps were observed on the low-coordinated sites, suggesting lower overpotential to initiate the reactions. Of the four low-coordinated sites, (211) site displays the highest catalytic performance, with the lowest energetic gaps for the rate-determining steps and the highest d-orbital energy relative to the Fermi level. Additionally, in the protonation step of $*OCH_3$ species, the formation of methane was found to be more thermally advantageous than the formation of methanol, implying the selectivity for methane in hydrocarbon generation. This finding suggests that the edge sites on metal NPs can effectively boost CO_2ER in aqueous solutions (Figure 7.2). However, despite the accelerated reaction rate of CO_2ER, the HER was also found to be energetically boosted on the low-coordinated Cu sites. Since HER competes the transferred electrons against CO_2ER, we conclude that a high operating potential should be applied in order to take advantage of the low-coordinated atomic sites, where both types of reactions are kinetically opened. This work gives a general explanation for the intrinsic reason of the catalytic enhancement observed among the currently employed approaches of structural modifications. We have proved that the created large numbers of low-coordinated sites are responsible for the catalytic behaviors.

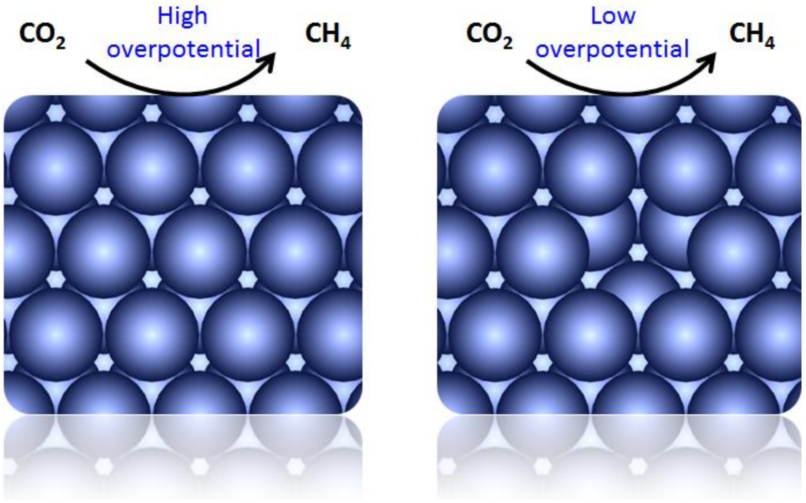

Figure 7.2 The role of low-coordinated sites: lowered overpotential for catalyzing CO_2ER.

The second hypothesis proposed is that surface alloying (SA) can be effective in designing CO_2ER catalyst with lowered reaction overpotential. By screening the catalytic ability of various transition-metal doped Cu SAs, candidates which are able to selectively catalyze CO_2 into CH_4 are expected to be found out. To perform this high-throughput screening work, we firstly evaluated the stability of Cu SAs. By computing the vertical segregation energy and the horizontal mixing energy, we found that only eight transition-metals (Au, Ag, Zn, Pt, Pd, Y, Sc, and Cd) can stably alloy Cu at the topmost surface layer. Catalytically, since the surface is where the reaction takes place, it's important that the bimetallic area forms at the topmost layer. This discovery provides a general thermodynamic trend, by a first-order estimate, of the possibility to form a surface alloy on Cu substrate. By computing the reaction energetics on these stably existed SAs, we find that dopants of Zn and small amount of Ag and Cd are found to remain the same onset potential as Cu for generating CH_4 and considerably enlarge the overpotential for the competing HER. SAs doped by Au and high percentage of Ag are observed to increase the overpotential for both the CO_2ER and HER. SAs with the dopant of Pt and Pd are not active for CO_2ER, but rather capable in catalyzing HER. Sc and Y are discovered to bind the reaction intermediates too strongly, leading to no catalytic activity for CO_2ER or HER. Finally, doping high concentration of Cd into Cu can effectively and selectively catalyze CO_2 into HCOOH, with the prevention of yielding hydrocarbons and significant suppress of the unwanted HER. Hence, the SA of CdCu is identified as a promising candidate for CO_2ER (Figure 7.3).

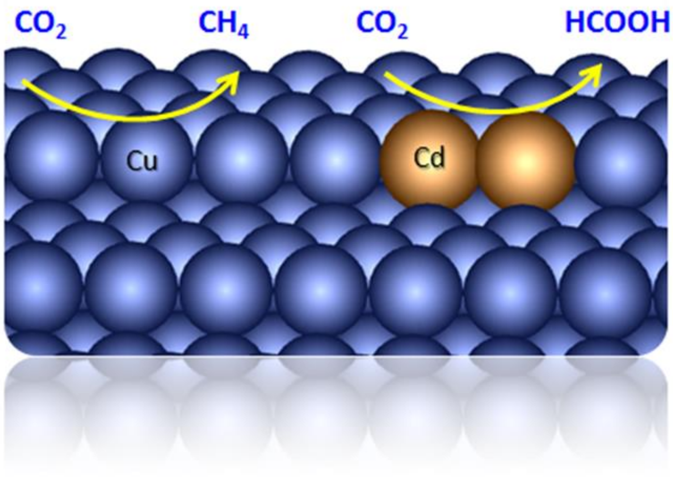

Figure 7.3 Adjacently located Cd in Cu surface can selectively catalyze CO_2 into HCOOH.

Finally, considering that the energy level of metal d-orbital electrons is sensitive to bulk arrangements and orientations[1], we hypothesized that phase transformation can alter the binding affinities of metals to the CO_2ER intermediate and thus give rise to more effective electro-catalysts. Since the metallic catalysts can be classified into three categories based on their product selectivity, we verified this hypothesis in chapter 6 on three different fcc metals – Cu (for hydrocarbon selectivity), Au (for CO selectivity), and Pb (for HCOOH selectivity). The catalytic behaviors of these metals in crystal phases of fcc, bcc, hcp (2H), 4H, and sc have been computed. We have found that Cu and Pb in sc orientation are not stable under CO_2ER conditions, since atomic transformations form sc to hcp are observed. On contrary, sc Au is rather stable in adsorbing the reaction intermediates. We attribute this phenomenon to the chemical activity of metals; that is, only passive metals in sc symmetry can work durably for catalyzing CO_2ER. For the other orientations, on all these three metals, the binding affinities for adsorbates follow the trend of fcc < hcp-type < bcc (Figure 7.4). Energetically, we believe this trend can provide useful guidance in manipulating the energy state for the key reaction intermediates and thus help design new effective electro-catalyst. Finally, we find that converting the original fcc phase of Cu, Au, and Pb into bcc type can decrease the energy gap of the rate-determining step and predicts lower reaction potentials for catalyzing CO_2ER. On Au and Pb, the estimated onset potentials for CO (product on Au) and HCOOH (product on Pb) are lowered by 25.2% and 21.3%, respectively, suggesting effective catalytic enhancement.

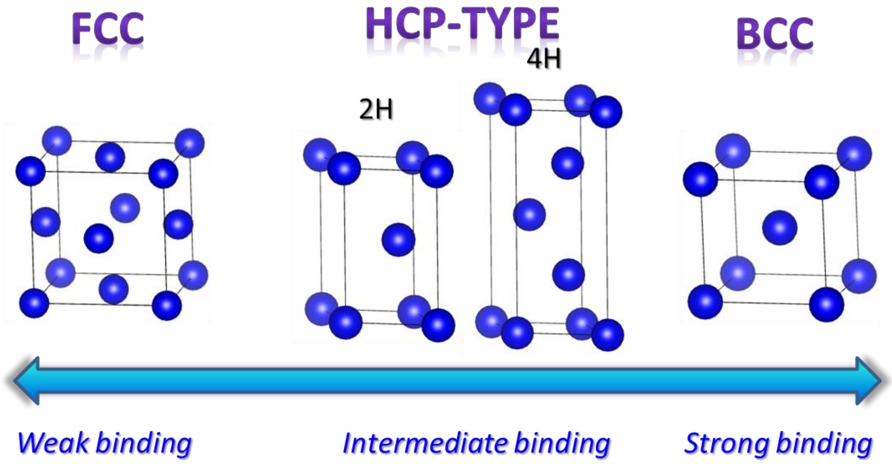

Figure 7.4 Trend of binding affinities of metals in various crystal phases: fcc < hcp-type < bcc.

To sum up, three different strategies are proposed on metal NPs in order to design advanced catalysts with low reaction overpotential for CO_2ER. The first one focuses on the structural modifications to the metal NPs. By calculating the reaction pathway on different low-coordinated Cu atoms, it has been discovered that the low-coordinated sites can boost CO_2ER with low energetic gap. This trend explains the reported catalytic improvements on structural modified (meta-stable surface, small size, ridged morphology, porous structures et al.) metal NPs. The second strategy is proposed based on the compositional modification of surface alloying. By screening the catalytic ability of transition-metal doped Cu SAs, we have found that Cd is an excellent dopant for Cu substrate in achieving efficient catalytic performance towards CO_2ER. The created Cd-Cd-Cu sites can selectively catalyze CO_2 into HCOOH with the prevention of generating hydrocarbons or hydrogen molecule. Finally, by employing the strategy of phase transformation, we have found that metals in different crystal phases would display different binding affinities to the adsorbates. The trend in binding abilities follows fcc < hcp-type < bcc. We believe this trend will provide useful guidance in tuning the binding capabilities of metal NPs.

7.2 Future Work

Inspired by the results obtained in this work and reported literature, some future work for the design of effective CO_2ER catalysts are recommended.

(1) As discussed in Chapter 5, for all the stable Cu SAs, although the reaction selectivity for CO_2ER is improved (HER is largely suppressed), the overpotentials of CO_2 reduction to CH_4 can hardly be decreased. This is because the *CO and *CHO binding energies scale with a slope of 0.89, meaning that a surface that stabilizes CO will, at the same time, stabilizes CHO by a similar amount. Therefore, the binding energies for the two intermediates involved in the rate-determining step are coupled, and the relative binding energies between them change only slightly with respect to different catalyst material.[2] However, the slope between E_B[COOH] and E_B[CO] is only 0.62, implying a wide potential for decreasing the energetics of the CO_2 protonation step. This may be quite

useful in achieving low reaction overpotentials on these metals with CO selectivity, where the elementary step of CO_2 protonation ($CO_2 \rightarrow$ *COOH) determines the overall reaction rate.[3-5] Inspired by this finding, we can extend the surface alloying strategy to metal Au, which can selectively reduce CO_2 into CO. So we hypothesize that Au SAs can be effective in catalyzing CO_2 into CO at lower operating potentials.

(2) When one or two monolayers of guest metals are deposited onto the surface of another metal, the formed core-shell structures show dramatically different electronic structures from the pure shell metals. The changed electronic energy level is largely due to the strain effect caused by the lattice mismatch between the core and the shell metal.[6,7] Since the electronic structures of surface metal play a crucial role in determining the catalytic activity, this strain effect can be of great help in designing effective CO_2ER catalyst. Specifically, according to Nørskov's work, the binding energies of O and CO on Ru(0001) surface decrease with the expansion of lattice constant.[8] Based on these, we expect that the same trend for the binding energies of CO_2ER intermediates can also be found on expanded Au surface. To verify this hypothesis, energetics of reaction pathway on Au(111) in different lattice constant has been computed (Figure 7.5).

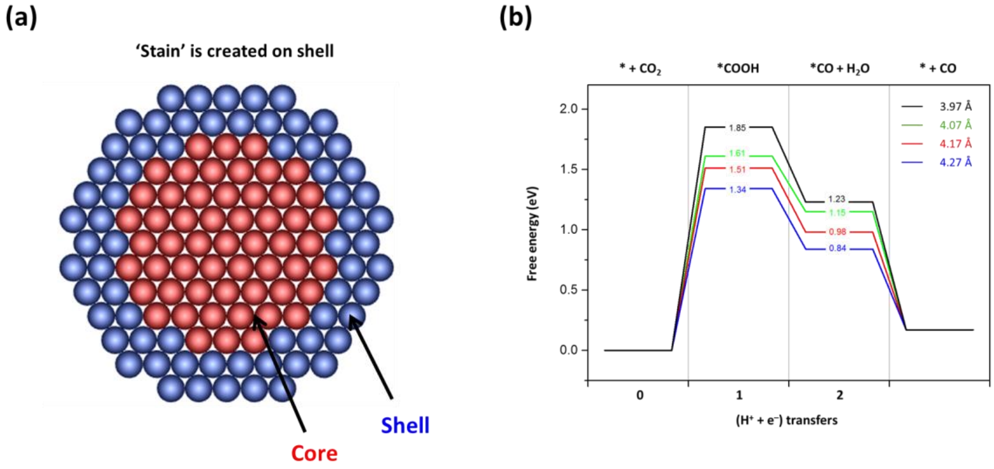

Figure 7.5 (a) Illustration of the strain effect created by core-shell structures. (b) Reaction diagram of CO_2 reduction to CO on Au in different lattice constants.

The results in Figure 7.5 suggest that the binding energies of both intermediates involved in CO_2 reduction to CO (*COOH and *CO) decrease as the lattice of Au expands. Supported by the preliminary results, it is rationale to conclude that an effective Au-based electro-catalyst can be made by matching a suitable substrate that can bring tensile strain to the Au shell. Therefore, we have supposed two catalyst models, Cd(0001)@Au and Pb(111)@Au, to be effective in catalyzing CO_2 into CO. The Cd(0001) and Pb(111) are chosen as the substrate metal because both surfaces display hcp atomic arrangement as the most close-packed surface on Au and have large enough atomic distance to bring tensile strain to the Au shell. Following calculations will be performed on these two models to test their stability and catalytic activity towards CO_2ER.

(3) Recently, 2D materials and their derivatives have been widely applied in many energy-related electro-catalysis reactions, such as HER[9,10], ORR[11,12], OER[13]. The unique electronic structures resulted from the 2D arrangement can be effective in optimizing the binding energies of key reaction intermediates. However, in the domain of CO_2ER, few works have been reported using 2D material as the catalyst. This is because most of the pure 2D materials (graphene, MoS_2, C_3N_4) have poor catalytic activity towards CO_2ER.[14,15] Moreover, the lack of theoretical predictions also hinders the experimental design of good CO_2ER catalyst in 2D style. Since graphene and MoS_2 are all consisted by earth-abundant elements, it is of great significance if they can be effective in catalyzing CO_2ER.

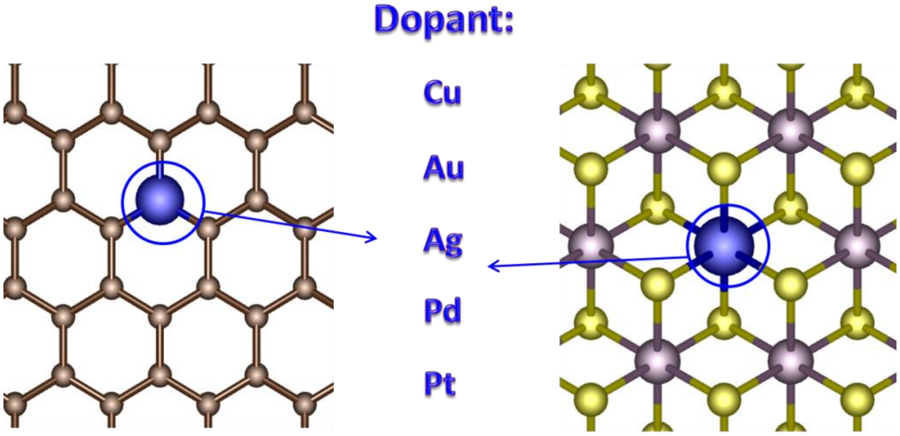

Figure 7.5 Illustration of the surface compositional modifications created by transition metal doping on graphene and 1T-MoS_2.

Recently, doping guest metals into the bulk lattice of has been found to be an effective method in altering the electronic property of 2D materials. Catalytically, all the possible binding sites (hollow, bridge, and top site) on single-layer graphene cannot actively capture CO_2. However, it has been reported that when doping metals (Li, Ca, or Fe) into the graphene lattice, the electronic structures can be tuned and lowered binding energies can be achieved.[16] For MoS_2, introducing W metal into the 1T phase can significantly alter its electronic structure and hence catalytic activity.[17] Therefore, in order to alter the electronic structures of graphene and 1T-MoS_2 and design effective CO_2ER catalyst, we aim to change their surface compositions by doping transition metals into their lattice. More specifically, we hypothesize that doping Cu, Pt, Pd, Au, and Ag into the surface of graphene and MoS_2 can provide ways for designing effective CO_2ER catalysts with low reaction overpotentials. These five kinds of metals are chosen because they can represent all the possible binding affinities towards CO_2ER intermediates. As the only metallic candidate that can selectively catalyze CO_2 into hydrocarbons, Cu has been found to display an intermediate binding affinity for the most important reaction intermediate – CO.[2] Meanwhile, the Pt and Pd group and the Au and Ag group are well-known for their strong and weak CO binding affinities, respectively.[2,18] Hence, it is believed that doping these five metals can effectively tune the catalytic activity of graphene and 1T-MoS_2 for CO_2ER. The following computational works will be performed on these systems.

References

1 Durand, W. J., Peterson, A. A., Studt, F., Abild-Pedersen, F. & Nørskov, J. K. Structure effects on the energetics of the electrochemical reduction of CO_2 by copper surfaces. *Surface Science* **605**, 1354-1359 (2011).

2 Peterson, A. A. & Nørskov, J. K. Activity Descriptors for CO2 Electroreduction to Methane on Transition-Metal Catalysts. *The Journal of Physical Chemistry Letters* **3**, 251-258 (2012).

3 Hansen, H. A., Varley, J. B., Peterson, A. A. & Nørskov, J. K. Understanding trends in the electrocatalytic activity of metals and enzymes for CO_2 reduction to CO. *The Journal of Physical Chemistry Letters* **4**, 388-392 (2013).

4 Rosen, J. *et al.* Mechanistic insights into the electrochemical reduction of CO_2 to CO on nanostructured Ag surfaces. *ACS Catalysis* **5**, 4293-4299 (2015).

5 Zhu, W. *et al.* Monodisperse Au nanoparticles for selective electrocatalytic reduction of CO_2 to CO. *Journal of the American Chemical Society* **135**, 16833-16836 (2013).

6 Strasser, P. *et al.* Lattice-strain control of the activity in dealloyed core–shell fuel cell catalysts. *Nature Chemistry* **2**, 454-460 (2010).

7 Bandarenka, A. S. *et al.* Design of an Active Site towards Optimal Electrocatalysis: Overlayers, Surface Alloys and Near Surface Alloys of Cu/Pt (111). *Angewandte Chemie International Edition* **51**, 11845-11848 (2012).

8 Mavrikakis, M., Hammer, B. & Nørskov, J. K. Effect of strain on the reactivity of metal surfaces. *Physical Review Letters* **81**, 2819 (1998).

9 Jaramillo, T. F. *et al.* Identification of active edge sites for electrochemical H_2 evolution from MoS_2 nanocatalysts. *Science* **317**, 100-102 (2007).

10 Voiry, D. *et al.* Conducting MoS_2 nanosheets as catalysts for hydrogen evolution reaction. *Nano Letters* **13**, 6222-6227 (2013).

11 Wang, T. *et al.* Size Dependent Enhancement of Electrocatalytic Oxygen Reduction and Hydrogen Evolution Performance of MoS_2 Particles. *Chemistry A European Journal* **19**, 11939-11948 (2013).

12 Sheng, Z.-H., Gao, H.-L., Bao, W.-J., Wang, F.-B. & Xia, X.-H. Synthesis of boron doped graphene for oxygen reduction reaction in fuel cells. *Journal of Materials Chemistry* **22**, 390-395 (2012).

13 Lin, Z., Waller, G. H., Liu, Y., Liu, M. & Wong, C.-p. 3D Nitrogen-doped graphene prepared by pyrolysis of graphene oxide with polypyrrole for electrocatalysis of oxygen reduction reaction. *Nano Energy* **2**, 241-248 (2013).

14 Kumar, B. *et al.* Renewable and metal-free carbon nanofibre catalysts for carbon dioxide reduction. *Nature Communications* **4** 2819 (2013).

15 Asadi, M. *et al.* Robust carbon dioxide reduction on molybdenum disulphide edges. *Nature Communications* **5** 4470 (2014).

16 Kang, H. S. Theoretical study of binding of metal-doped graphene sheet and carbon nanotubes with dioxin. *Journal of the American Chemical Society* **127**, 9839-9843 (2005).

17 Li, H., Yu, K., Tang, Z. & Zhu, Z. Experimental and First-Principles Investigation of MoWS2 with High Hydrogen Evolution Performance. *ACS Applied Materials & Interfaces* **8**, 29442-29451 (2016).

18 Back, S., Kim, H. & Jung, Y. Selective heterogeneous CO_2 electroreduction to methanol. *ACS Catalysis* **5**, 965-971 (2015).

.

Appendix

Free Energy Corrections for Adsorbates and Gaseous Molecules Involved in CO_2ER

Table S1 The zerio-point energy correction, enthalpy, and entropy correction for adsorbates. All values are given in the unit of eV.

Adsorbate	ZPE	$\int C_P dT$	-TS
*COOH	0.62	0.10	-0.18
*CO	0.19	0.08	-0.15
*CHO	0.44	0.09	-0.18
$*CH_2O$	0.76	0.09	-0.19
$*OCH_3$	1.11	0.09	-0.18
*O	0.07	0.03	-0.04
*OH	0.36	0.05	-0.08
*H	0.16	0.01	-0.01

Table S2 The zerio-point energy correction, enthalpy, and entropy correction for free gaseous molecules. All values are given in the unit of eV.

Gas Molecule	ZPE	$\int C_P dT$	-TS
CO_2	0.31	0.10	-0.65
CO	0.14	0.09	-0.67
H_2	0.27	0.09	-0.42
CH_3OH	1.35	0.11	-0.79
H_2O	0.58	0.10	-0.65
CH_4	1.20	0.10	-0.60
CH_2O	0.70	0.10	-0.66